Stripline-based microfluidic devices for high-resolution NMR spectroscopy

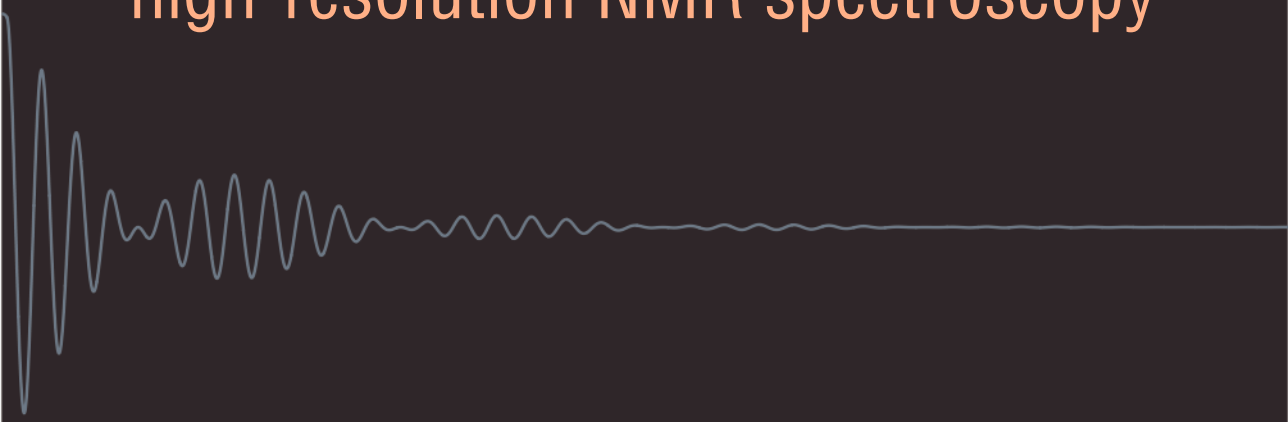

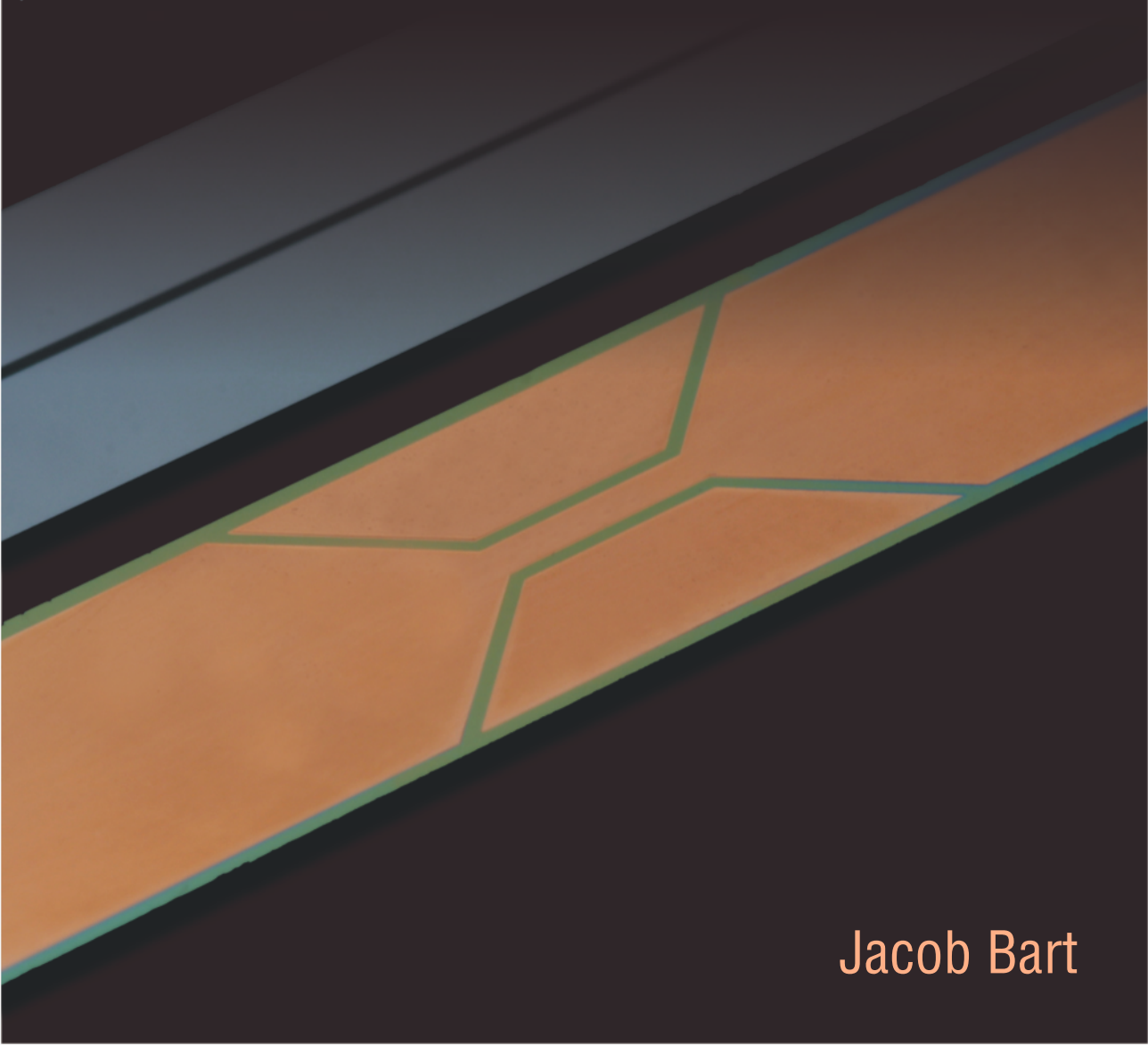

Jacob Bart

Stripline-based microfluidic devices for high-resolution NMR spectroscopy

The research described in this dissertation was carried out at the Mesoscale Chemical Systems group of the MESA+ Institute for Nanotechnology at the University of Twente (Enschede, The Netherlands) and the Solid State NMR group of the Institute for Molecules and Materials (IMM) at the Radboud University (Nijmegen, The Netherlands). The project was financially supported by The Netherlands Organisation for Scientific Research - NWO.

Graduation committee

Chairman and secretary

Prof. dr. G. van der Steenhoven	Universiteit Twente

Promotors

Prof. dr. J.G.E. Gardeniers	Universiteit Twente
Prof. dr. A.P.M. Kentgens	Radboud Universiteit Nijmegen

Co-promotor

Dr. P.J.M. van Bentum	Radboud Universiteit Nijmegen

Members

Dr. P.J.A. van Tilborg	Schering Plough Corporation
Dr. G. Boero	Ecole Polytechnique Fédérale de Lausanne
Prof. dr. G. Siegal	Universiteit Leiden
Prof. dr. ir. J. Huskens	Universiteit Twente
Prof. dr. ir. A. van den Berg	Universiteit Twente

Stripline-based microfluidic devices for high-resolution NMR spectroscopy
Bart, Jacob
ISBN: 978-90-365-2898-6
Publisher: Wöhrmann Print Service, Zutphen, The Netherlands

STRIPLINE-BASED MICROFLUIDIC DEVICES FOR HIGH-RESOLUTION NMR SPECTROSCOPY

PROEFSCHRIFT

ter verkrijging van
de graad van doctor aan de Universiteit Twente,
op gezag van de rector magnificus,
prof. dr. H. Brinksma,
volgens besluit van het College voor Promoties
in het openbaar te verdedigen
op donderdag 24 september om 16.45 uur

door

Jacob Bart
geboren op 21 juli 1980
te Kampen

This dissertation has been approved by:

Prof. dr. J.G.E. Gardeniers

Prof. dr. A.P.M. Kentgens

Dr. P.J.M. van Bentum

Table of Contents

Preface

NMR spectroscopy is one of the principal analysis techniques in chemistry, biology, medicine and material sciences. It is a powerful technique that can provide detailed information on the topology, dynamics and three-dimensional structure of molecules in solution and the solid state.

In **Chapter 1** the general concept of Nuclear Magnetic Resonance (NMR) is introduced. The basic equations describing the NMR phenomenon show the inherent low sensitivity of the technique. Therefore, different sensitivity enhancement methods are addressed, leading to the core of this thesis: micro-NMR. The two main approaches towards micro-NMR using helical microcoils are briefly discussed, namely solenoid coils and planar coils.

In **Chapter 2** a novel 'microcoil' design which departs from traditional helices is introduced: the stripline. The stripline geometry is compared with solenoids and planar coils in terms of sensitivity, resolution and implementation. Preliminary results obtained with a 'proof of principle' set-up are demonstrated.

An optimization study for stripline-based NMR detectors in terms of sensitivity, resolution and rf-homogeneity is presented in **Chapter 3**. Based on the determined optimal design, a first-generation microfluidic 'Lab on a chip' implementation is realized in silicon and the performance of this device is compared to modelling results.

Chapter 4 describes the monitoring of chemical reactions as an appealing application of the microfluidic NMR chip. Because the stripline can be operated in-flow it exhibits the possibility to follow reactions *in-situ*. The acetylation of benzyl alcohol in the presence of DIPEA is performed in an external microreactor and real-time measured on the NMR detector. The additional information that can be obtained because of *in-situ* measurement is presented. Furthermore, the effects of flow on the NMR performance are discussed.

In **Chapter 5** the feasibility of the microfluidic chip for the analysis of mass-limited samples is demonstrated by analyzing 600 nL human cerebrospinal fluid. These measurements are compared to spectra obtained with a standard NMR set-up.

Based on the optimization study and the results achieved in the silicon chip, it was aimed for a design which was fully optimized in all respects. In **Chapter 6** the fabrication and performance of a stripline chip based on a glass substrate is discussed.

Chapter 7 discusses a novel concept for fast concentration of low concentration biofluids, based on a porous hollow fiber evaporator. This concept is analytically modelled, such that concentration rates can be predicted. A 'proof of principle' set-up is constructed, with which a 22 μM phenolred solution in water is concentrated up to 16 times.

Chapter 8 discusses a novel wafer bond technique which was invented during the fabrication of the silicon based striplines, discussed in Chapter 3. This concept allows for bonding of glass or silicon wafers at room temperature and relies on the covalent amide-bond established between amine-terminated substrates and NHS-ester terminated fluorinated ethylene propylene foils.

– Chapter 1 –

General introduction

Parts of this chapter have been published as:

A.P.M. Kentgens, J. Bart, P.J.M. van Bentum, A. Brinkmann, E.R.H. van Eck, J.G.E. Gardeniers, J.W.G. Janssen, P. Knijn, S. Vasa, M.H.W. Verkuijlen, *J. Chem. Phys.* 128, 1 (2008).

J. Bart and J.G.E. Gardeniers, *Micro Process Engineering: A Comprehensive Handbook*, Volume 3, V. Hessel, J.C. Schouten (eds.), Wiley-VCH, 135 (2009).

Introduction

Nuclear Magnetic Resonance (NMR) was discovered in 1945 by Purcell and Bloch. Almost simultaneously, without knowledge about each others work, they discovered the response of atomic nuclei to radio frequency signals.[1] For this discovery they received the Nobel Prize in 1952. Since that time NMR has rapidly advanced as an interdisciplinary technique that covers the principles of chemistry, physics, engineering, medicine, and biology. NMR spectroscopy has become one of the major analytical techniques for elucidation of molecular structures in both liquid and solid phases.

In this chapter the fundamentals of NMR will be discussed.[2,3,4] Furthermore, different sensitivity enhancement methods will be addressed, leading to the core of this thesis: microcoils.

Fundamentals of NMR: a semi-classical description

Spin polarization

Matter is made of atoms. Atoms consist of electrons and nuclei. One of the fundamental properties of most nuclei is spin. Spin is a form of angular momentum, not produced by a rotation or movement, but an intrinsic property of the nucleus itself. The spin angular momentum $\hat{J}$ of atomic nuclei is quantized, and takes values of the form:

$$\hat{J} = \hbar\hat{I} = \hbar\sqrt{[I(I+1)]} \qquad 1.1$$

where $\hat{I}$ the spin momentum (vector) and I is the quantum number (scalar). The spin angular momentum $\hat{J}$ has a magnetic dipole moment $\hat{\mu}$:

$$\hat{\mu} = \gamma\hat{J} = \gamma\hbar\hat{I} \qquad 1.2$$

where γ is the gyromagnetic ratio which can be either negative or positive, depending on the nuclear isotope. In the absence of a magnetic field, the orientation of $\hat{\mu}$ is random and the orientation distribution of an ensemble of spins is isotropic.

When a static magnetic field B_0 (along the z-axis by convention) is applied to a spin ensemble, the energy of the spin system becomes quantized in *2I+1* levels (Zeeman effect) and the magnetic dipole moments start to precess around the field at the Larmor frequency ω_0:

$$\omega_0 = -\gamma B_0 \qquad 1.3$$

Considering nuclei with spin quantum number I = ½, two spin energy levels exist. These are referred to as spin-up and spin-down states or α and β, respectively. The energy difference is:

$$E = -\hat{\mu} \cdot B_0 = -\gamma \hbar \hat{I} \cdot B_0 = -\gamma \hbar I_z B_0 \qquad 1.4$$

where I_z is the projection of $\hat{I}$ on the z-axis. The negative sign indicates that the magnetic energy is lowest if the magnetic moment is parallel to the B_0-field.

Apart from the externally applied field, the spins experience the very small field fluctuations of the surrounding nuclear spins which influence the orientation of the spin. Since the environment has a finite temperature, it is slightly more probable that the nuclear spin is driven towards an orientation with low magnetic energy than towards an orientation with high magnetic energy. Note that a single nuclear spin is generally not exactly at one of the two energy levels α or β, but in an entangled state. As a consequence, the net distribution of magnetic moment is not longer isotropic (equal in all directions), but starts to become anisotropic (with a preferential orientation), see Figure 1.1. This results in a net magnetic moment which makes nuclear magnetism observable.

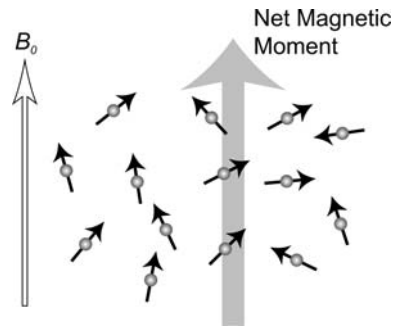

Figure 1.1. Anisotropic nuclear spin orientation distribution in the presence of a static magnetic field B_0 in thermal equilibrium. For the sake of clarity, the picture greatly exaggerates the anisotropy. Reproduced from Ref. 3.

This process is called dipolar relaxation and the rate of the magnetization build-up $M_z(t)$ is determined by the spin-lattice relaxation time constant T_1 as follows:

$$M_z(t) = M_0(1 - 2e^{-\frac{t}{T_1}}) \qquad 1.5$$

where M_0 is the equilibrium magnetization.

According to the fundamental Boltzmann law of statistical mechanics, the populations ρ_i of the quantized spin-states with different values for $I_z=m$ are proportional to:

$$\rho_i = \frac{e^{\frac{E_i}{k_B T}}}{\sum_{m=-I}^{I} e^{\frac{E_m}{k_B T}}} \qquad 1.6$$

Where k_B is the Boltzmann constant and T is the temperature. Given that:

$$\sum_{m=-I}^{I} {m_z}^2 = \frac{1}{3}\sum_{m=-I}^{I} m^2 = \frac{1}{3} I(I+1)(2I+1) \qquad 1.7$$

the net macroscopic nuclear magnetization M_0 along the direction of the B_0 field will be:

$$M_z = N\gamma\hbar \frac{\sum_{m=-I}^{I} m_z\, e^{\frac{E_m}{k_B T}}}{\sum_{m=-I}^{I} e^{\frac{E_m}{k_B T}}} \approx \frac{N\gamma^2\hbar^2 B_0}{k_B T} \frac{\sum_{m=-I}^{I} m_z^2}{2I+1} = \frac{N\hbar^2\gamma^2 B_0 I(I+1)}{3k_B T} \qquad 1.8$$

This equation is called the Curie Law, and the high-temperature approximation is used because in practice, E/k_BT is a very small number which makes a linear Taylor expansion of the Boltzmann exponential valid.

Exploring Eq. 1.6 for practical numbers indicates the minute difference in populations which makes NMR an intrinsically insensitive method. For instance, at regular fields of 11.7 T at room-temperature, there is only one excess 'spin up' out of 10^5 spins. The longitudinal nuclear spin magnetization can not be detected inductively. Therefore, Fourier-transform (FT) NMR takes a different approach by flipping the magnetization to the xy-plane (transverse magnetization) and measures the precession of the magnetic moment, which is called the Free Induction Decay (FID).

Transverse magnetization

An ensemble of nuclear spins in a static magnetic field can be seen as a tiny magnetic dipole $\vec{M}_z$ as described by Eq. 1.8. From classical physics it is known that a magnetic

dipole in an external field experiences a torque which tries to align the dipole parallel to the externally applied field:

$$\frac{d\vec{J}}{dt} = \vec{M} \times \vec{B} \tag{1.9}$$

Using Eq. 1.2, the motion of the magnetic moment in B_0 is described by the equation:

$$\frac{d\vec{M}}{dt} = \gamma \vec{M} \times B_0 \tag{1.10}$$

Flipping the net magnetization vector in the xy-plane is performed by an extra oscillating magnetic field B_1, *e.g.* applied along the x-axis:

$$B_x = 2B_1 \cos(\omega t) \tag{1.11}$$

B_x can be described as two field vectors B_R and B_L rotating in opposite directions with identical angular velocities:

$$\begin{aligned} \vec{B}_R &= B_1(\vec{x}\cos\omega t + \vec{y}\sin\omega t) \\ \vec{B}_L &= B_1(\vec{x}\cos\omega t - \vec{y}\sin\omega t) \end{aligned} \tag{1.12}$$

where $\vec{x}$ and $\vec{y}$ are unit vectors along the x- and y-axis. Since application of B_0 and B_1 results in a complicated movement of the magnetization vector, it is useful to transform to rotating coordinates. For this purpose, a frame rotating with angular velocity $\vec{\Omega}$ is introduced which expresses the variations in the magnetic dipole $\vec{M}$ in terms of the unit vectors $\vec{i}$, $\vec{j}$ and $\vec{k}$:

$$\begin{aligned} \frac{d\vec{M}}{dt} &= \frac{dM_x}{dt}\vec{i} + \frac{dM_y}{dt}\vec{j} + \frac{dM_z}{dt}\vec{k} + M_x\frac{d\vec{i}}{dt} + M_y\frac{d\vec{j}}{dt} + M_z\frac{d\vec{k}}{dt} \\ &= \frac{\partial\vec{M}}{\partial t} + \vec{M} \times \vec{\Omega} \end{aligned} \tag{1.13}$$

Equation 1.13 contains a time-dependent term of $\vec{M}$ in the rotating frame. Finally, using Eq. 1.10, it follows:

$$\frac{\partial\vec{M}}{\partial t} = \gamma\vec{M} \times (B_0 - \frac{\vec{\Omega}}{\gamma}) \tag{1.14}$$

When the rotating frame angular velocity $\vec{\Omega}$ is chosen to be equal to the Larmor frequency ω_0, the effective field experienced by $\vec{M}$ is zero. Introducing the

alternating field B_x, described by B_R and B_L in the rotating frame, and maintaining the convention to have all angular frequencies positive, it follows that there is one field which is time-independent and aligned along a certain axis, and one rotating with $2\omega_0$. Without loss of generality the contribution of the part rotating with $2\omega_0$ can be ignored. In the rotating frame, the magnetization vector only precesses around the time-independent part of the rf-field, as shown in Figure 1.2, with frequency:

$$\omega_1 = \gamma B_1 \tag{1.15}$$

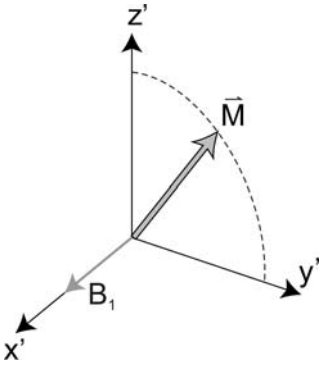

Figure 1.2. The movement of the magnetization vector $\vec{M}$ in the rotating frame during the appliance of an rf-field B_1.

To flip the orientation of the magnetization over an angle of 90° (to arrive parallel to the y'-axis), the length of the rf-pulse should be:

$$\tau_{90} = \frac{1}{4}\frac{2\pi}{\gamma B_1}\text{sec} \tag{1.16}$$

From Eq. 1.14, it can be concluded that after an rf-pulse, the transverse magnetization vector is time-independent in the rotating frame. However, in the laboratory frame, it precesses at frequency ω_0 around the main field. The current induced by this alternating field is the signal which is detected by NMR spectroscopy. Because of microscopic field fluctuations the coherence will not last forever, but decays in time with the transverse relaxation time constant T_2:

$$M_x = M_o \sin(\omega_0 t)\, e^{\frac{-t}{T_2}} \text{ and } M_y = M_o \cos(\omega_0 t)\, e^{\frac{-t}{T_2}} \tag{1.17}$$

This movement is depicted in Figure 1.3.

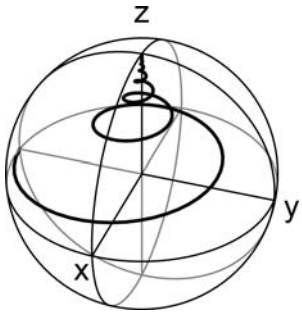

Figure 1.3. The trajectory taken by the tip of the magnetization vector $\vec{M}$ after a 90° pulse for T_1=T_2. Reproduced from Ref. 3.

Observation of the transverse magnetization

The oscillating transverse magnetization vector described in Eq. 1.17 can be detected by means of an rf-coil which is placed perpendicular to the B_0-field. Early NMR spectrometer designs used separate transmitter and receiver coils; however, modern designs use a single transceiver coil that is electronically connected to the transmitter during the pulse and then to the receiver after the pulse. The magnetization vector will induce a current in the coil from which amplitude and phase correspond to the precession of the magnetization vector. The resulting time-domain signal is the sum of sinusoids which have frequencies close to the Larmor frequency, corresponding to spins in different electronic environments. Fourier transformation is utilized to visualize the different frequencies in one spectrum.

The position of a specific resonance line in the spectrum provides information about the local environment of a certain nucleus, as will be described below in more detail. The peak intensity is proportional to the amount of spins with resonance at the specific position in the spectrum, and can therefore be used as a (relative) measure of the concentration of the species to which the nuclear spins belong.

Chemical shift

Chemical shift was discovered in 1951 by Arnold, Dharmatti, and Packard.[5] Before that time, NMR was mainly applied for the accurate determination of the nuclear magnetic moments of all elements in the periodic table. Arnold et al. found that the total magnetic field experienced by a nucleus in its equilibrium state includes local magnetic fields induced by currents of electrons in the molecular orbitals. The electron distribution usually varies according to the local geometry (binding partners, bond lengths, angles between bonds, etc.), and with it the local magnetic field at each nucleus. This is reflected in the spin energy levels (and resonance

frequencies). The local magnetic field B_{loc} experienced by the nucleus therefore differs from the applied field B_0:

$$B_{loc} = (1-\sigma)B_0 \qquad 1.18$$

where σ is the screening constant which strongly depends on the electronic environment.

The variation of nuclear magnetic resonance frequencies of the same kind of nucleus, due to variation in the electron screening, is called the chemical shielding, which results in a chemical shift δ in the spectrum. The size of δ is given with respect to a reference sample, *e.g.* tetramethylsilane (TMS) for protons. Figure 1.4 shows the first ^{1}H-spectrum of ethanol CH_3CH_2OH recorded by Arnold et al., which has three resonance peaks: one belonging to the CH_3 protons, one belonging to the CH_2 protons, and one resonance for the OH proton.

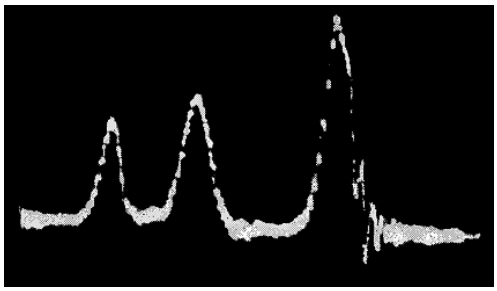

Figure 1.4. First wide-line ^{1}H-NMR spectrum recorded by Arnold, Dharmatti, and Packard. Three peaks are distinguishable corresponding to the OH, CH_2 and CH_3 groups (left to right). Reproduced from Ref. 5.

Chemical shifts are generally not reported in Hertz units, since the strength of every magnet is different. Therefore, the frequency difference δ is usually reported on a *ppm* scale which is defined as the frequency shift in Hertz divided by the Larmor frequency for that particular nucleus in the used magnet:

$$\delta_{ppm} = \frac{2\pi\Delta\nu}{\gamma B_0} \qquad 1.19$$

where $\Delta\nu$ is the frequency shift in Hertz.

Nuclei experiencing the same chemical environment or chemical shift are called equivalent. Considering equivalent nuclei (for example the three protons of the CH_3 group in an ethanol molecule) one expects a single resonance line belonging to these spins. However, high-resolution spectra show splitting as a result of couplings to neighbouring spins sharing electrons through chemical bonds, as shown in Figure

1.5. This is called spin-spin coupling or J-coupling. In the case of the ethanol molecule, the two spins belonging to the CH_2 group can be both up, both down or one up and one down. The latter configuration has twice the probability of the first two configurations. This leads to a splitting of the CH_3 peak in three peaks with intensities 1:2:1, in which the outer peaks result from the both up and both down configurations of the CH_2 spins, whereas the centre peak results from the two configurations in which one CH_2 spin is up and one is down. In contrast to chemical shifts, J-couplings are denoted in Hertz units, since they are independent of the applied static field.

Apart from J-coupling, other spin-interactions exist like direct dipolar coupling and quadrupolar coupling. However, these interactions are generally not directly manifested in 1D-NMR spectra of liquids, and therefore not discussed here.

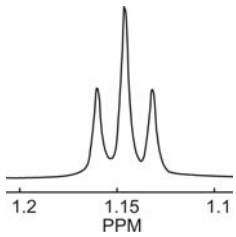

Figure 1.5. Detail of a ^{1}H-NMR spectrum of ethanol, showing the CH_3 triplet with intensities 1:2:1. Recorded on a regular NMR-spectrometer (5 mm tube, 500 µL of pure ethanol).

General experimental NMR set-up

Detection of the nuclear magnetism is a considerable instrumental challenge. First, the signal is very weak. Second, the Larmor frequencies must be measured with extremely high accuracy (<1 part of 10^8). In the following the components necessary for a reliable detection system are described.

Magnet and console

A static magnetic field B_0 is necessary to build up the net magnetization in the sample. Generally, superconducting magnets are used (see Figure 1.6), which produce strong fields up to 23.4 Tesla (Larmor frequency of 1 GHz for protons). In order to achieve narrow lines in the NMR spectrum, and allow visualisation of small differences in Larmor frequencies ω_0, the field should be homogeneous across the whole sample range. This sets high demands to the homogeneity of the magnet. For example, a linewidth of 1 Hz Full Width Half Maximum (FWHM) for a ^{1}H-spectrum in

a magnetic field of 14.1 Tesla (600 MHz proton resonance) requires a homogeneity better than 1.67 ppb over the sample volume.

The electronics generating the rf-wave to excite the spins, and the low-noise amplifiers for detection of the weak NMR signals are included in the console (Fig. 1.6). Finally, computer equipment is necessary for controlling the electronics, data acquisition and processing.

Figure 1.6. A 14.1 Tesla superconducting magnet (equivalent with 600 MHz for ^{1}H-NMR) placed in the Goudsmit Pavilion in Nijmegen (left), together with the console containing the necessary electronics for NMR spectroscopy (right).

Probe

The probe contains the rf-coil and the sample. Figure 1.7a shows a probe and Figure 1.7b a conventional 5 mm sample tube. Standard liquid probes are equipped with a so-called saddle-coil (Fig. 1.7c) which is the most-favourable coil configuration in combination with 5 mm tubes. Since the rf-coil is positioned closely to the sample, highest care has to be taken with respect to metal-induced distortion of the B_0-field. Especially in the case of small samples, the configuration of the rf-coil design plays a crucial role with respect to the finally achieved spectral resolution.

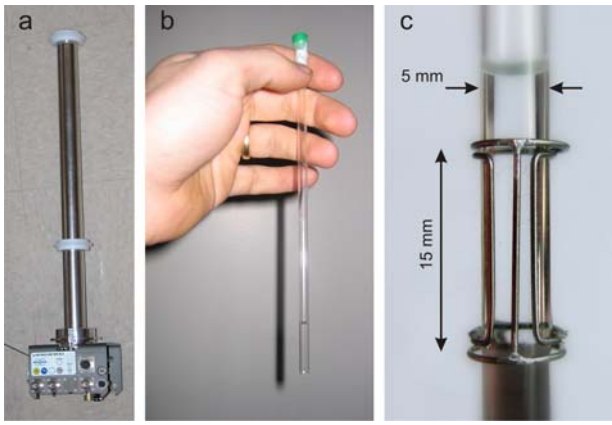

Figure 1.7. a) An NMR probe. The length is typically 0.5 meter, necessary to position the sample in the center of the magnet.
b) Standard NMR sample tube with 5 mm diameter. The sample volume is ~500 μL.
c) A saddle rf-coil as implemented in most liquid-state NMR probes.

NMR sensitivity enhancement methods based on establishing non-Boltzmann populations

As mentioned before, sensitivity is the Achilles heel of NMR. This is due to the almost equal Boltzmann population of the different energy levels at room temperature. For liquid-state NMR, various approaches can be utilized to alter the population difference in order to obtain higher net-magnetizations.

DNP

A promising approach is to pre-polarize the spin system by polarization transfer. The majority of experiments on low γ nuclei involve transfer of polarization from abundantly present proton spins which have a much larger Zeeman splitting, allowing an enhancement proportional to the ratio of the gyromagnetic constants. Since the electron magnetic moment is much larger than any nuclear moment, exploiting the coupling of the nuclear spins to unpaired electron spins can be very advantageous. This Dynamic Nuclear Polarization (DNP) phenomenon is being investigated with varying intensity. Shortly after discovery of NMR the transfer mechanisms such as the nuclear Overhauser effect[6] or the solid-effect, underlying various forms of polarization transfer were described.[2]

With the advent of high-resolution solid-state NMR, DNP research re-emerged and focused on the investigation of materials where unpaired electrons are inherently present such as diamonds, coal, chars, doped organic polymers etcetera.[7] With the drive to higher external NMR fields the interest for DNP declined, however,

since the efficiency of the main polarization transfer effects become less efficient at higher magnetic fields. Moreover there was no clear strategy to make DNP more generally applicable to materials without unpaired electrons. It was the pioneering work of Griffin and co-workers that changed this situation by introducing suitable microwave sources[8,9] for high-field DNP-NMR, optimizing sample preparation techniques using frozen solutions containing radicals[10] and studying the transfer mechanisms that can be exploited at high fields.[11] This knowledge is now exploited in the development of new radicals and radical mixtures that optimize the transfer efficiency using three-spin processes.[12,13] Ardenkjaer-Larsen et al.[14] developed a protocol to quickly dilute frozen solutions after DNP enhancement to produce highly polarized molecules to be used in liquid-state NMR and specifically in-vitro and in-vivo applications. This approach has been commercialized which will lead to many practical applications and trigger further methodological investigations.

CIDNP

In liquids nuclear hyper polarization by chemically induced radical pairs has proven to be much more accessible.[15,16,17] This chemically induced dynamic nuclear polarization (CIDNP) has been used extensively to study chemical reactions forming radical intermediates.[18] By probing (changes in) the solvent-accessibility of tryptophan, tyrosine, and histidine residues in proteins by means of laser-induced photochemical reactions information about the folding of proteins can be obtained.[19,20] More recently photo-induced polarization has also been explored in photosynthetic reaction centers in solid-state NMR.[21,22] Ongoing research by Matysik and coworkers gives insight in the mechanisms involved.[23] This holds some promise as an alternative polarization source if synthetic photoreaction centers can be made.

Para-Hydrogen

Another promising chemical approach to produce highly spin-polarized molecules is the use of para-hydrogen (p-H_2) in hydrogenation reactions performed either in high-field[24] or zero-field with subsequent cycling to high-field.[25] Para-hydrogen (hydrogen with the coupled proton spins in the singlet state) is stable in liquid solutions and can be used as a fully spin-polarized reactant. In most hydrogenation reactions the symmetry of the proton pair will be broken leading to highly spin-polarized reaction products giving strongly enhanced spectral NMR resonances. This can be used to identify reaction intermediates and study the reaction kinetics but also to produce polarized molecules which can subsequently be used in *in-vitro* or *in-vivo* magnetic resonance spectroscopy and imaging experiments.[26,27,28]

NMR sensitivity enhancement based on microcoils

As has been summarized above great progress has been made in the various approaches to enhance the NMR spin transitions by establishing non-Boltzmann populations in the spin system. So far however there is no generic protocol that can be used to spin polarize any substance. In fact most solutions described above only work for certain classes of material and need substantial investment in additional hardware. Therefore it is of interest to explore alternatives such as optimizing the currently used detector coils. Even if the potential gains are much smaller it should be realized that a signal gain of a factor of 10 will decrease the experiment time by a factor of 100 which can easily bring the measurement times for various experiments so far considered impossible down to a feasible level.

In 1976 Richard and Hoult have described the sensitivity of an NMR experiment via inductive detection.[29] Based on this work Webb and co-workers have shown that the sensitivity of an NMR coil is inversely proportional to the coil diameter given a constant length-to-diameter ratio. This was experimentally verified in 1994 when they showed that by miniaturizing the detection coil, the NMR sample volume could be brought down to the nanoliter regime.[30,31] This has triggered substantial research into the use of microcoils (loosely defined here as coils with less than 1 mm diameter) mainly in liquid-state high-resolution NMR. For routine NMR analysis one typically requires at least 10^{16} nuclear spins. Even then, several scans have to be averaged to obtain a sufficient SNR in the frequency domain, which can be very time consuming. Microcoils offer the possibility to decrease the necessary measurement time, if that same amount of spins can be measured in a more sensitive coil. Most appealing is the role microcoils can play in the field of analyzing mass-limited samples. The applicability of conventional NMR is limited in that case, because of the low number of spins involved. Performing reliable NMR on mass-limited samples in a conventional NMR system means that the sample has to be dissolved in a (deuterated) solvent in order to fill the standard sample chamber. This decrease in concentration means a decrease in SNR. However, this dissolution is not longer necessary when microcoils with optimized sizes are utilized. Nowadays, Bruker Biospin offers the so-called 1 mm probe, which is based on the regular saddle coil geometry in combination with a sample tube, however downscaled such that the observed volume is 5 µL.[32]

Apart from the sensitivity enhancement obtainable with microcoils, the small sample scales which can be handled make microcoils of considerable interest for hyphenation with other analysis and micro separation techniques such as liquid

chromatography, electrophoresis and even gas chromatography.[33,34,35,36] Furthermore, within the microreactor chemistry, there is a growing interest in onboard placed chemical sensors because this opens the way to in-flow monitored production processes of high-grade compounds executed on one chip. The research and development of NMR micro-probes, and the sensitivity advances of micro-probes has had a tremendous impact on the capabilities of NMR as a detection mechanism for chemical techniques using mass limited samples.

Although making smaller coils seems a trivial step, the challenges in the design of microcoil probeheads are to get the highest possible sensitivity while maintaining high-resolution and keeping the versatility to apply all known NMR experiments. This means that the coils have to be optimized for a given sample geometry, circuit losses should be avoided, susceptibility broadening due to probe materials has to be minimized and finally the B_1 fields generated by the rf-coils should be homogeneous over the sample volume. Moreover, the rf-circuit should be simultaneously tunable for multiple frequencies to allow multinuclear experiments.

Until now, two different approaches towards miniaturization are pursued in liquid-state NMR, one focuses on capillary NMR[30,31,37,38,39,40,41,42,43,44] where tightly wound solenoids are the predominant coil design. The second approach is to work in microfluidic devices which use planar helical structures for the detection of the NMR signal.[45,46,47,48,49,50]

Solenoids

The first attempt to perform high-resolution NMR on sample volumes down to 5 nL was published by Wu et al.[51] A solenoidal microcoil wrapped directly around a fused silica capillary containing 5 nL of sample was placed in a conventional superconducting magnet. The coil was used as a detection system for liquid chromatography. With a thin-walled capillary (75 μm ID, 145 μm OD) they obtained linewidths over 200 Hz (0.73 ppm) for a 0.8 M sample of arginine, while for a thick-walled capillary (75 μm ID, 350 μm OD) the linewidths were narrowed to 11 Hz (0.037 ppm). Although the minimally detectable numbers of spins from these microcoils were considerably better than achieved with standard probes, the linewidths of the order of 10-20 Hz were unacceptable for high resolution NMR spectroscopy.

The first high resolution NMR spectra were presented by Olson et al.[31] who employed the same design (Fig. 1.8) but obtained linewidths of 0.6 Hz (0.002 ppm) FWHM, on a sample of pure ethylbenzene.

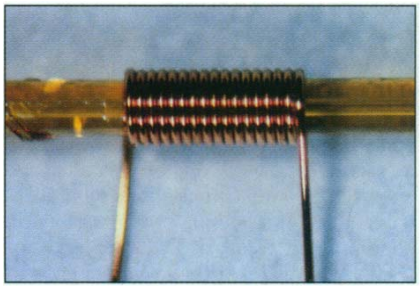

Figure 1.8. Microcoil wrapped around fused silica capillary. The coil is composed of 50 µm-diameter copper wire, has a length of 1 mm, and an outer diameter of 470 µm. From Ref. 31.

They showed that the resolution can be improved significantly by immersing the used copper detection coil in perfluorocarbon FC-43 (fluorinert), having nearly the same susceptibility as copper. In that case the sample is surrounded by a homogenous susceptibility cylinder; according to electromagnetic field theory, a sample enclosed by a perfectly uniform and infinitely long hollow cylinder experiences a uniform static magnetic field.[52]

This concept has been optimized and implemented in probes which are now commercially available under the name CapNMR.[37,53,54] The probes are currently used for in-flow NMR,[55] in-flow LC-NMR,[56] and as high-throughput NMR spectroscopic instruments, by means of coupling it to an HPLC pump and an autosampler.[57]

The basic considerations for solenoid microcoils have been reviewed by Webb.[58] Optimization of rf-homogeneity and SNR was treated by Minard and Wind;[59,60] they give clear guidelines for the design of solenoid microcoils with respect to the number of windings and wire diameters depending on the conductivity of the samples. Engelke has described the specific problems that are encountered in the high-frequency operation of solenoid coils where the wavelength of the rf-irradiation is no longer large with respect to the coil dimensions.[61]

Planar coils

Not surprisingly, the fabrication of solenoidal rf-microcoils is a manufacturing challenge, especially at smaller wire dimensions. An alternative to manually wrapping the wires around capillary tubes is to take advantage of lithographic fabrication techniques. Several groups investigated planar microcoils as the modern way to perform NMR on nanoliter samples.

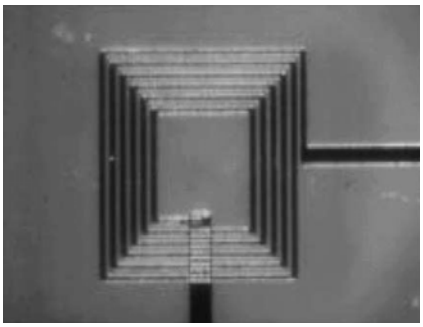

Figure 1.9. Electron micrograph of the first planar microcoil. The outer diameter is 200 µm. From Ref. 45.

The first planar microcoil for NMR detection was demonstrated by Peck et al.,[45] who patterned a GaAs substrate with gold inductors, using photolithographical and lift-off methods. An electron micrograph of the coil is shown in Figure 1.9. A silicone rubber sample was placed directly over the coils. With this configuration a FWHM of 60 Hz (0.2 ppm) was obtained.

A thorough study of the electrical and spectroscopic characteristics of planar microcoils was done by Massin et al.,[48,62] who characterized and optimized a microfluidic probe with a planar microcoil on a glass substrate. A channel was etched in a Pyrex glass substrate and the NMR detection coil was electroplated on the top surface of the microfluidic wafer stack. With this chip (depicted in Figure 1.10), containing a sample of 160 µg sucrose in 470 nL D_2O, they obtained a spectral SNR of 38 (16 times averaged) and a FWHM of 9 Hz (0.03 ppm).

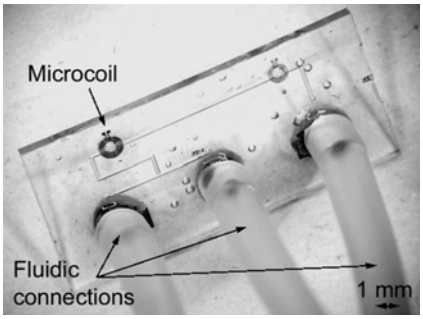

Figure 1.10. Picture of a micromachined planar NMR probe. The glass chip has a size of 16×8 mm^2. The visible microfluidic channels have a width of approximately 170 µm. The pointed microcoil has an inner diameter of 500 µm, and an observe volume of 30 nL. The sample is injected via flexible plastic tubes connected to inlet and outlet holes on the backside of the chip. From Ref. 48.

Conclusions

NMR has become the analytical method of choice in many areas of research. However, the main bottleneck that impedes certain advancements in the field of NMR spectroscopy is the relatively low sensitivity of the NMR detection method. Although great progress has been made in various approaches to enhance the NMR signals by establishing non-Boltzmann populations in the spin system, there is no generic protocol that can be used to spin polarize any substance. An alternative for sensitivity enhancement for mass-limited samples is the utilization of microcoils. Conventional microcoils can be divided in 3D coils (mostly solenoids) and 2D planar coils. An exciting advantage of microcoils compared to conventional NMR is the compatibility with other micro analysis and separation techniques, and microreactors.

References

[1] F. Bloch, *Nobel lecture*, 1952.
[2] A. Abragam, *The Principles of Nuclear Magnetism*, Clarendon Press, Oxford (1961).
[3] M.H. Levitt, *Spin dynamics. Basics of Nuclear Magnetic Resonance*, John Wiley & Sons, Ltd, Chichester (2001).
[4] R. Verhagen, *Novel radio-frequency and force-detected approaches in nuclear magnetic resonance*, PhD-thesis, Katholieke Universiteit Nijmegen, The Netherlands (2002).
[5] J.T. Arnold, S.S. Dharmatti, M.E. Packard, *J. Chem. Phys.* 19, 507 (1951).
[6] A.W. Overhauser, *Phys. Rev.* 92 (2), 411 (1953).
[7] R.A. Wind, R. Lewis, H. Lock, G.E. Maciel, *Adv. Chem. Ser.* 229, 45 (1993).
[8] L.R. Becerra, G.J. Gerfen, R.J. Temkin, D.J. Singel, R.G. Griffin, *Phys. Rev. Lett.* 71 (21), 3561 (1993).
[9] V.S. Bajaj, C.T. Farrar, I. Mastovsky, J. Vieregg, J. Bryant, B. Elena, K.E. Kreischer, R.J. Temkin, R.G. Griffin, *J. Magn. Res.* 160 (2), 85 (2003).
[10] G.J. Gerfen, L.R. Becerra, D.A. Hall, R.G. Griffin, R.J. Temkin, D.J. Singel, *J. Chem. Phys.* 102 (24), 9494 (1995).
[11] C.T. Farrar, D.A. Hall, G.J. Gerfen, S.J. Inati, R.G. Griffin, *J. Chem. Phys.* 114 (11), 4922 (2001).
[12] C.S. Song, K.N. Hu, C.G. Joo, T.M. Swager, R.G. Griffin, J. Am. Chem. Soc. 128 (35), 11385 (2006).
[13] K.N. Hu, V.S. Bajaj, M. Rosay, R.G. Griffin, *J. Chem. Phys.* 126 (4), 044512 (2007).
[14] J.H. Ardenkjaer-Larsen, B. Fridlund, A. Gram, G. Hansson, L. Hansson, M.H. Lerche, R. Servin, M. Thaning, K. Golman, *Proc. Nat. Ac. Sci. USA* 100 (18), 10158 (2003).
[15] J. Bargon, *Helv. Chim. Acta* 89 (10), 2082 (2006).

[16] R. Kaptein, *Chem. Phys. Lett.* 2 (4), 261 (1968); R. Kaptein, J.L. Oosterhoff, *Chem. Phys. Lett.* 4 (4), 195 (1969); R. Kaptein, L.J. Oosterhoff, *Chem. Phys. Lett.* 4 (4), 214 (1969).
[17] G.L. Closs, *J. Am. Chem. Soc.* 91 (16), 4552 (1969); G.L. Closs, A.D. Trifunac, *J. Am. Chem. Soc.* 91 (16), 4554 (1969).
[18] J. Bargon, *Photochem. Photobiol. Sci.* 5 (10), 970 (2006).
[19] K.H. Mok, P.J. Hore, *Methods* 34 (1), 75 (2004).
[20] L.T. Kuhn, J. Bargon, *In Situ Nmr Methods in Catalysis*, Vol. 276, pp. 125, Springer (2007).
[21] M.G. Zysmilich, A. McDermott, *J. Am. Chem. Soc.* 116 (18), 8362 (1994); M.G. Zysmilich, A. McDermott, *Proc. Nat. Ac. Sci. USA* 93 (14), 6857 (1996); M.G. Zysmilich, A. McDermott, *J. Am. Chem. Soc.* 118 (25), 5867 (1996); A. McDermott, M.G. Zysmilich, T. Polenova, *Solid State Nucl. Magn. Reson.* 11 (1-2), 21 (1998).
[22] J. Matysik, A. Alia, P. Gast, H.J. van Gorkom, A.J. Hoff, H.J.M. de Groot, *Proc. Nat. Ac. Sci. USA* 97 (18), 9865 (2000).
[23] A. Diller, S. Prakash, A. Alia, P. Gast, J. Matysik, G. Jeschke, *J. Phys. Chem. B* 111 (35), 10606 (2007).
[24] C.R. Bowers, D.P. Weitekamp, *Phys. Rev. Lett.* 57 (21), 2645 (1986); C.R. Bowers, D.P. Weitekamp, *J. Am. Chem. Soc.* 109 (18), 5541 (1987).
[25] M.G. Pravica, D.P. Weitekamp, *Chem. Phys. Lett.* 145 (4), 255 (1988).
[26] D. Canet, C. Aroulanda, P. Mutzenhardt, S. Aime, R. Gobetto, F. Reineri, *Concepts Magn. Reson. Part A* 28A (5), 321 (2006).
[27] L.T. Kuhn, J. Bargon, *In Situ Nmr Methods in Catalysis*, Vol. 276, pp. 25, Springer (2007).
[28] P. Bhattacharya, K. Harris, A.P. Lin, M. Mansson, V.A. Norton, W.H. Perman, D.P. Weitekamp, B.D. Ross, *Magn. Reson. Mater. Phys., Biol. Med.* 18 (5), 245 (2005).
[29] D.I. Hoult, R.E. Richards, *J. Magn. Reson.* 24, 71 (1976).
[30] N.A. Wu, T.L. Peck, A.G. Webb, R.L. Magin, J.V. Sweedler, *Anal. Chem.* 66 (22), 3849 (1994).
[31] D.L. Olson, T.L. Peck, A.G. Webb, R.L. Magin, J.V. Sweedler, *Science* 270 (5244), 1967 (1995).
[32] Bruker BioSpin GmbH, Rheinstetten. www.bruker-biospin.com
[33] A.M. Wolters, D.A. Jayawickrama, J.V. Sweedler, *Curr. Opin. Chem. Biol.* 6 (5), 711 (2002).
[34] D.A. Jayawickrama, J.V. Sweedler, *J. Chromatogr A* 1000 (1-2), 819 (2003).
[35] K. Albert, *Nachr. Chem.* 54 (4), 428 (2006).
[36] M.D. Grynbaum, D. Kreidler, J. Rehbein, A. Purea, P. Schuler, W. Schaal, H. Czesla, A. Webb, V. Schurig, K. Albert, *Anal. Chem.* 79 (7), 2708 (2007).
[37] D.L. Olson, J.A. Norcross, M. O'Neil-Johnson, P.F. Molitor, D.J. Detlefsen, A.G. Wilson, T.L. Peck, *Anal. Chem.* 76, 2966 (2004).
[38] F.C. Schroeder, M. Gronquist, *Angew. Chem. Int. Ed.* 45 (43), 7122 (2006).
[39] D.L. Olson, M.E. Lacey, J.V. Sweedler, *Anal. Chem.* 70 (3), 645 (1998).
[40] D.A. Seeber, L. Ciobanu, C.H. Pennington, *Appl. Magn. Reson.* 22 (2), 139 (2002)
[41] D.A. Seeber, R.L. Cooper, L. Ciobanu, C.H. Pennington, *Rev. Sci. Instr.* 72 (4), 2171 (2001).
[42] M. Kakuta, D.A. Jayawickrama, A.M. Wolters, A. Manz, J.V. Sweedler, *Anal. Chem.* 75 (4), 956 (2003).
[43] D. Sakellariou, G. Le Goff, J.F. Jacquinot, *Nature* 447 (7145)
[44] A.F. McDowell, N.L. Adolphi, *J. Magn. Reson.* 188 (1), 74 (2007).

[45] T.L. Peck, R.L. Magin, J. Kruse and M. Feng, *IEEE Trans. Biomed. Eng.* 41, 706 (1994).
[46] J.E. Stocker, T.L. Peck, A.G. Webb, M. Feng, R.L. Magin, *IEEE Trans. Biomed. Eng.* 44 (11), 1122 (1997).
[47] J.D. Trumbull, I.K. Glasgow, D.J. Beebe, R.L. Magin, *IEEE Trans. Biomed. Eng.* 47 (1), 3 (2000).
[48] C. Massin, F. Vincent, A. Homsy, K. Ehrmann, G. Boero, P.A. Besse, A. Daridon, E. Verpoorte, N.F. de Rooij, R.S. Popovic, *J. Magn. Reson.* 164 (2), 242 (2003).
[49] H. Wensink, F. Benito-Lopez, D.C. Hermes, W. Verboom, J.G.E. Gardeniers, D.N. Reinhoudt, A. van den Berg, *Lab Chip* 5 (3), 280 (2005).
[50] J. Dechow, A. Forchel, T. Lanz, A. Haase, *Microelectron. Eng.* 53, 517 (2000).
[51] . N. Wu, T.L. Peck, A.G. Webb, R.L. Magin, J.V. Sweedler, *J. Am. Chem. Soc.* 16, 7929 (1994).
[52] N.N. Rao, *Electromagnetics*, Prentice Hall, New York (1992).
[53] Protasis/MRM Corporation, Illinois, USA.
[54] W. Peti, J. Norcross, G. Eldridge, M. O'Neil-Johnson, *J. Am. Chem. Soc.* 126, 5873 (2004).
[55] A. Jansma, T. Chuan, R.W. Albrecht, D.L. Olson, T.L. Peck, B.H. Geierstanger, *Anal. Chem.* 77, 6509 (2005).
[56] R.J. Lewis, M.A. Bernstein, S.J. Duncan, C.J. Sleigh, *Magn. Reson. Chem.* 43, 783 (2005).
[57] N.J.C. Bailey, I.R. Marshall, *Anal. Chem.* 77, 3947 (2005).
[58] A.G. Webb, *Prog. Nucl. Magn. Reson. Spectrosc.* 31, 1 (1997).
[59] K.R. Minard, R.A. Wind, Concepts in Magnetic Resonance 13 (2), 128 (2001).
[60] K. R. Minard and R. A. Wind, Concepts in Magnetic Resonance 13 (3), 190 (2001).
[61] F. Engelke, *Concepts Magn. Reson.* 15 (2), 129 (2002).
[62] C. Massin, G. Boero, F. Vincent, J. Abenhaim, P.A. Besse, R.S. Popovic, *Sens. Actuators A* 97-98, 280 (2002).

– Chapter 2 –

Stripline probes for NMR

Parts of this chapter have been published as:

P.J.M. van Bentum, J.W.G. Janssen, A.P.M. Kentgens, J. Bart, J.G.E. Gardeniers, *J. Magn. Reson.* 189, 104 (2007).

Introduction

In the previous chapter microcoils are introduced as a way to enhance the NMR sensitivity. Although several groups have studied microcoils for NMR, nearly all have used the helix shape so far. In this chapter, a novel NMR detector will be introduced, the stripline, which departs from the idea of a helical structure.

First, the stripline will be introduced as a new approach for NMR detection. After that, some general sensitivity calculations will be discussed, in which different coil geometries are evaluated, starting with conventional designs (solenoids and planar coils). These three geometries will be compared with respect to sensitivity, resolution and some implementation issues. Furthermore the thermal characteristics of the stripline which determine the limits in excitation bandwidth will be discussed. Finally, a preliminary implementation including experimental results based on this implementation will be presented.

The stripline configuration

Generally, when a radio frequency (rf) current is fed through a straight wire, an electromagnetic rf-field will be generated which encircles this wire. When such a wire is positioned parallel to a static B_0-field, the generated magnetic component of the rf-field is perpendicular to this static field, and can be used for the excitation of NMR transitions. By reciprocity (see below) the same wire can be used to detect the NMR signal. This simple 'coil' geometry is very interesting because it hardly disturbs the static field homogeneity, holding great promise for high resolution NMR spectroscopy. From Maxwell's equations, it can be deduced that an infinitely long metal wire placed parallel to a static magnetic field does not affect the homogeneity of this field. This approximately holds also for finite length wires, as long as the length of the wire is much larger than the distance of the sample from this wire.

Clearly, a simple wire is not an efficient NMR detector, because the rf-field strength decreases inversely proportional with the distance to the wire. This can be remedied to some extent by putting a cylindrical conductor around the wire as in a coaxial arrangement. This geometry indeed results in a sensitive NMR detector as used in toroid cavities.[1] For regular NMR its drawback is the remaining strong rf-inhomogeneity, although this can be exploited favourably in imaging and diffusion experiments.[2,3]

A stripline is a two-dimensional analogue of such a wire. The term 'stripline' originates from the high frequency electronics field, where they are commonly used as transmission lines that route high frequent signals with low losses. The geometry

was invented by Robert M. Barrett of the Air Force Cambridge Research Centre in the 1950's. In a stripline the current is fed through a thin metal strip. A non-radiative closed configuration is realized by placing ground planes both above and below the strip which help to homogenize the rf-field. Figure 2.1 shows a schematic representation of the geometry, indicating the dimensional parameters, *l* (length of the strip), *w* (width of the strip) and *d* (distance between the ground planes).

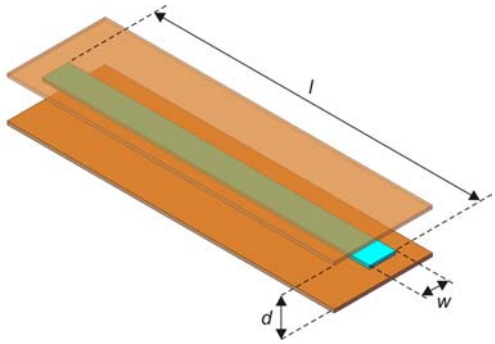

Figure 2.1. 3D representation of a stripline configuration. Color differences are only for clarity: the central strip which feeds the rf-current and the ground planes are made from the same material.

A cross-sectional view of the stripline configuration is shown in Figure 2.2. The rf-current is fed through the central strip and the rf-field generated by this current encircles the strip.[4] The B_1-field points in opposite directions above and below the stripline, but sample positioned at both sides of the strip will contribute in phase to the signal.

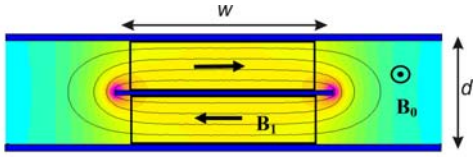

Figure 2.2. Schematic cross-section of the stripline design. The rf-field B_1 circulates around the strip as indicated by the field lines. The local rf-field strength is indicated by the color map (blue corresponds to a low B_1-field and red to high B_1-field). Because of the boundary conditions imposed by the metallic planes above and beneath the strip, the magnetic field lines are forced parallel to the surface. The result is a large volume with a homogeneous B_1-field. Suitable sample chambers are indicated by the two black rectangles where the B_1-field is homogeneous within about 10%. Also, the current distribution in the strip is homogeneous thereby minimizing electrical losses. For NMR applications one can use the stripline geometry both for excitation and detection by insertion of this structure inside an external field. The static field B_0 can be oriented perpendicular to the cross section shown in the Figure (along the stripline axis). The rf-current that runs through the central copper strip flows parallel to the static field.

The boundary conditions at the metal surface dictate that the field lines run parallel to this surface: as a result a very good B_1-field homogeneity is realized. The current distribution over the strip is fairly homogeneous (except at the very edges), and Eddy currents are avoided. Because of the applied ground planes, a large volume exists with a homogeneous B_1-field resulting in a high filling factor. Sample chambers can be positioned above and below the central strip as indicated by the black rectangles in Figure 2.2. The resulting structure is optimal for high-resolution and high-sensitivity NMR, because of the minimal susceptibility distortion combined with the high filling factor.

In traditional helices and saddle coils, the B_1-field is naturally concentrated in the interior of the coil. For a stripline configuration, the B_1-field strength is a function of the diameter of the central line. Therefore, the central line has to be constricted, resulting in a region where the current density is high and the corresponding B_1-field is concentrated in a small volume. In the areas where the central line is not constricted, the rf-field will be low, because the rf-energy is distributed over a larger volume. In this way, a well-defined sample selection is guaranteed. Figure 2.3 shows a simulated rf-distribution along the central line, assuming a constant current along the line.

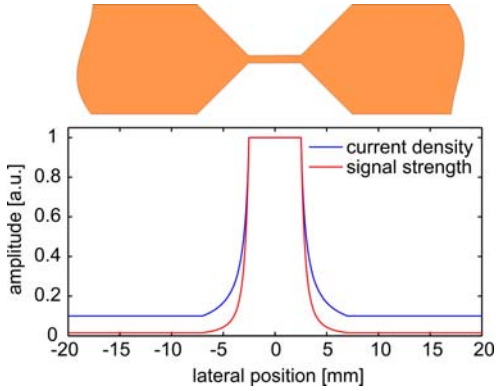

Figure 2.3 By defining a constriction in the central line, the current density (blue line) will be locally enhanced, and the corresponding B_1-field is concentrated. Since the stripline is used for excitation and detection, the signal response along the line after a 90° pulse will show an even stronger sample selection.

In comparison with the planar helix, the stripline has the advantage that all connections can be made in the same plane, removing the problems associated with the connection to another plane. A very interesting feature of the stripline design is that the surface can be scaled in a simple and trivial way, such that optimal matching for specific sample sizes is feasible.

Recently, Gershenfeld and co-workers introduced the microslot design for NMR spectroscopy that bears common ideas with the stripline design.[5,6] In both cases the sample is located close to a small metal strip carrying the rf-current. In the microslot design no attempt is made to homogenize the B_1-field as ground planes are absent.

Sensitivity

General considerations

The motivation to miniaturize the NMR receiver coil is based on the principle of reciprocity as discussed by Hoult and Richards.[7] Reciprocity means that the sensitivity of an NMR coil used as a receiver to a magnetic dipole present at position *P*, is proportional to that coil's efficiency, when used as a transmitter to generate an rf-field B_1 at *P*. In other words, a coil that generates a high B_1-field per unit current is also a sensitive detection coil. This also implies that one needs to put the sample at the position where the coil concentrates most of its magnetic energy. Based on these considerations the SNR of the receiver coil can be deduced, starting from the magnitude of the magnetization M_0 of a sample recently subjected to a 90° pulse, as calculated in chapter 1, reproduced here for convenience:

$$M_z = \frac{N\hbar^2\gamma^2 B_0 I(I+1)}{3k_B T} \qquad 2.1$$

The electromotive force ξ induced in the coil due to the precessing magnetization *m* in an infinitesimal volume at position *r* in the coil is:

$$\xi \sim -\frac{d}{dt}\left(\frac{B_1(r)}{i}\cdot m(r,t)\right) \qquad 2.2$$

where $B_1(r)/i$ is the magnetic field induced in the rf-coil per unit current. Assuming a reasonable homogeneity of B_1 over the sample volume V_s, the integration of Eq. 2.2 becomes trivial, giving the signal *S* induced by the whole sample magnetization:

$$S = k_0\omega_0\left(\frac{B_1}{i}\right)M_0 V_S \cos\omega_0 t \qquad 2.3$$

where k_0 is a scaling factor accounting for the rf-inhomogeneity of the coil and ω_0 is the rf-angular frequency. The rms-value of thermal noise signal *N* in an electrical conductor is expressed by:

$$N = \sqrt{4k_B TR\Delta f} \qquad 2.4$$

with Δf being the spectral bandwidth and R the resistance of the coil. Dividing the averaged signal S by the noise N, and using Eq. 1.3 finally gives:

$$SNR = \frac{k_0\left(\frac{B_1}{i}\right)V_S N\gamma\hbar^2 I(I+1)\frac{\omega_0^2}{k_B T 3\sqrt{2}}}{F\sqrt{4k_B TR\Delta f}} \qquad 2.5$$

where F is the noise factor of the spectrometer.

From Eq. 2.5 the possibilities to optimize sensitivity are easily identified. The obvious choice is to go to the highest possible external field to maximize ω_0. Furthermore, it is advantageous to cool the detector circuitry as is done in so-called cryoprobes to reduce the noise and, if possible, cool the sample leading to a reciprocal increase in the magnetization. Limited to optimization of the detector coil, Eq. 2.5 can be simplified. The effective sample volume $V_s'=k_0V_s$ is defined as the volume in which the homogeneity of B_1 is within a defined range. With these parameters the SNR is given by:

$$SNR = C\frac{\left(\frac{B_1}{i}\right)N_s}{\sqrt{R\Delta f}} \qquad 2.6$$

where N_s is the number of spins located within the effective volume V_s'. For protons at 600 MHz the constant C equals $1.4\cdot10^{-11}$ in SI units (B_0=14.09 T, T=300 K, $\gamma=0.2675\cdot10^9$ rad/T·s, I=1/2 and F=1, assuming negligible noise contribution from the spectrometer). From this expression it is clear that for a good SNR one should optimize the filling factor and, as stated by the reciprocity theorem, design the coil such that the highest possible rf-field is generated per unit current, *i.e.* maximize B_1/i. It goes without saying that one should minimize all possible losses in the rf-circuit as the actual SNR is proportional to $1/\sqrt{R}$. The coil geometry is an important design parameter to achieve high sensitivity: to get the optimal SNR the coil design has to be adapted to the specific size and shape of the sample, generating a high (and for most experiments uniform) B_1-field over the whole sample volume. For a high effective filling factor the integrated magnetic energy outside the sample should be as low as possible.

Limit of Detection (LOD)

In order to compare the sensitivity of different probes, it is inconvenient to express the sensitivity by means of the experimentally obtained SNR in the frequency domain for one peak. This is because the final SNR depends on the experimental set-up as well as the data treatment. Therefore, the limit of detection (LOD) is defined here, as the number of spins that have to resonate in a 1 Hz bandwidth to give a signal as strong as the rms-noise in a single acquisition:

$$LOD = \frac{N_s}{SNR_{t,SS}\sqrt{\Delta f}} \tag{2.7}$$

where N_s is the number of spins, Δf is the bandwidth in which the spins resonate (*e.g.* the linewidth of one line) and $SNR_{t,SS}$ is the single scan SNR in the time domain. This definition makes comparison of different probes straightforward, and is independent of the data treatment and sample. Determination of the LOD must be performed with a sample having a well-known proton concentration (without unknown proton residues from *e.g.* D_2O). In that case, the first point in the FID corresponds to the integral of all the protons in the sample, and gives therefore a valuable $SNR_{t,SS}$.

Solenoid

From textbook physics it is well-known that winding a wire in the form of a helix is an efficient way to produce a strong field in the coils interior. An idealized helical coil is a cylindrical shell with a uniform current density. The center field of such a cylindrical shell can be deduced using Biot-Savart's law:

$$\frac{B_1}{i} = \frac{\mu_0 n}{\sqrt{D^2 + l^2}} \tag{2.8}$$

where μ_0 is the permeability of free space, n the number of turns in the coil, and D and l the diameter and length of the coil, respectively. The rf-current will penetrate to a frequency dependent penetration depth δ. For copper at room temperature and at 600 MHz δ equals 2.7 μm. The resistance is described by:

$$R = \rho \frac{\pi D}{l\delta} \tag{2.9}$$

where ρ is the resistivity of copper. Note that for a fixed coil size, the number of windings n in a helix does not influence the sensitivity. Although the field factor increases linearly in n, the resistance scales with n^2 (doubling the number of turns

implies a halving of the wire diameter for a fixed coil size), so both signal and noise are amplified by the same transformation factor. By substituting Eq. 2.8 and 2.9 in Eq. 2.6, the optimal sensitivity can be calculated by taking the derivative and maximizing B_1/i for a D/l ratio, which gives:

$$\frac{D}{l}=1 \qquad 2.10$$

The resulting SNR is given by:

$$SNR = K\frac{N_s}{D\sqrt{\Delta f}} \qquad 2.11$$

where K accounts for all the constants including C. Thus, for a fixed number of spins the signal to noise ratio indeed scales with $1/D$ as predicted by Hoult and Richards.[7]

Even for an ideal solenoid the B_1-field falls off to half the center field at the ends of the helix. This inherent inhomogeneity is amplified by the fact that parallel currents repel each other, leading to a redistribution of the current away from the axis for the outermost windings. The decrease in rf-field strength at the edge of the coil can be somewhat counteracted by reducing the winding pitch at the end of the coil (so-called end-compensated coils[8]). In Figure 2.4, a field map of a 4-turn helix with an inner diameter of 280 µm and a height of 300 µm is displayed.

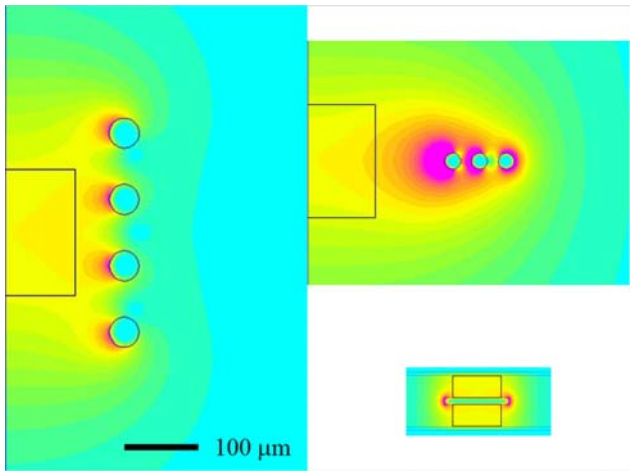

Figure 2.4. Comparison of the sizes of a solenoid (left), a flat helical (right top) and a stripline (right bottom) design needed for NMR experiments on 5 nL of sample. Note that the drawing is on scale. The sample is confined to a volume where the B_1-field varies by less than 10%. For the helical probes this sample volume is cylindrical. The scalability of the stripline allows for a compact design with the sample in rectangular bars of 1 mm long.

The effective sample volume with a B_1-homogeneity within 10% of the central field, indicated by the thin solid line, represents a volume of 5 nL. Numerical analysis shows that in this volume only 15% of the total magnetic energy is stored. The main parameters that specify the coil sensitivity, B_1/i and $\sqrt{R}$, can be calculated directly from the numerical results. Using Eq. 2.7 and 2.11, for this microhelix a LOD of $4{\cdot}10^{12}$ proton spins in a 1 Hz bandwidth is calculated.

Flat Helical

A well studied alternative for the helix is the surface microcoil that can be produced with micromachining techniques. Especially for the use in combination with microfluidic devices, integrated in silicon or glass chips, this design has been put forward. The calculation of the B_1/i and the coil resistance of this design, together with an analysis of the sensitivity as function of the number of windings has been given by Eroglu et al.[9] and Wensink et al.[10] A detailed analysis of such a surface spiral, again based on Bio-Savart's law, is shown in Figure 2.5, indicating that this design has some serious drawbacks compared to a solenoid. First, every winding that is added is less efficient than the previous one as it contributes less to the center axial field, but it increasingly adds to the resistive losses in the coil. Second, the fields produced by the outer windings cause considerable eddy currents in the center windings (the so-called proximity effect), adding additional losses and lowering the field homogeneity in the center region. Therefore the optimum for a flat helix is found for a single turn, which has the same theoretical sensitivity as a 3D single-turn helix. However, because the condition stated in Eq. 2.10 is completely impractical for a flat helix and therefore can never be fulfilled, the sensitivity will in general be lower than the sensitivity of a solenoid.

Another disadvantageous aspect of surface coils is that the innermost winding has to be connected to the contact pads via a bridge. This not only further disrupts the rf-homogeneity, but also complicates production with the need of extra layers and thus introducing additional losses. To make the comparison more quantitatively, the sensitivity of a flat helix is again examined for a 5 nL sample, see Figure 2.4. The cylindrical sample volume in which the field is homogeneous within 10% from the center field is indicated by the thin solid line. For this configuration only 4% of the total magnetic energy is concentrated in the sample volume. The LOD is found to be $7{\cdot}10^{12}$ proton spins per $\sqrt{\text{Hz}}$, which is nearly a factor of 2 less than the helix discussed above. In practical designs it is not straightforward to obtain a low loss connection to the inner winding, but this is not included in the numerical calculation.

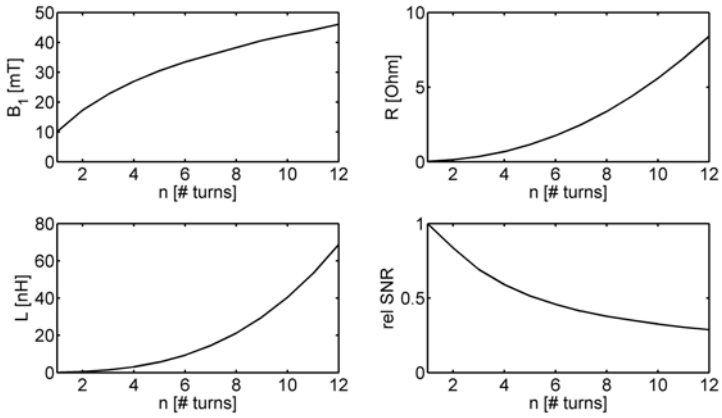

Figure 2.5. Analysis of an idealized planar microcoil with an inner diameter of 100 µm and a spacing of 13.2 µm between the windings. The effect of adding concentric windings is analyzed analytically based on Biot-Savart's law. The width and height of the copper deposits are taken to be 40 µm x 20 µm. Adding more windings increases B_1/i in the center of the field, but the SNR for a given number of spins goes down as each new winding introduces more resistive losses and has a relatively low filling factor (see text).

Stripline

To evaluate the sensitivity of the stripline, the expressions for B_1/i and the resistance R are explored in a similar way as is done for a solenoid. For these calculations the resistance of the constriction is assumed to be by far dominant and therefore the other resistive losses can be neglected. The width of the strip is denoted by w, the length of the stripline by l and the distance between the metallic ground planes by d. For simplicity an aspect ratio w/d=1 is chosen, and l/w=2π. For this situation, the sample volume is approximately $2\pi w^3$, which is the same volume as in the case of a helix for d=2w. The strip resistance is identical to that of the single turn solenoid (cylindrical current shell) as described above:

$$R = \frac{\rho l}{2\delta w} = \frac{\pi\rho}{\delta} \qquad 2.12$$

The B_1 field follows directly from Ampere's law:

$$\oint \vec{B}\cdot d\vec{s} = \mu_0 i \quad \text{yielding:} \quad B_1 / i = \frac{\mu_0}{2w} \qquad 2.13$$

Substituting B_1/i and R in Eq. 2.6 gives:

$$SNR = K\frac{\sqrt{2}\cdot N_s}{d\sqrt{\Delta f}} \qquad 2.14$$

where K accounts for the same constants as in Eq. 2.11, showing that the SNR is a factor $\sqrt{2}$ larger than that of the equivalent helix. Thus, in contrast to common sense estimates, the optimum rf detection geometry is not the helix. The main physical reason is the fact that for the micro-stripline the current distribution is homogeneous and runs on both sides of the strip. In a cylindrical shell, the current flows almost exclusively at the inside, so the effective dissipation is doubled and the sensitivity is reduced by $\sqrt{2}$.

To complete the quantitative comparison between solenoids, flat helicals and striplines, the magnetic field distribution for a planar stripline configuration containing 5 nL of sample is depicted in Figure 2.4. As can be seen the stripline provides the most compact design because it has the highest effective homogeneous B_1 volume. This volume, represented by the two boxes above and below the strip, contains more than 50% of the total magnetic energy and the LOD is found to be $3\cdot10^{12}$ proton spins per $\sqrt{\text{Hz}}$ for a strip length of 1 mm. This is consistent with the estimates based on the idealized model and confirms that the stripline configuration can indeed be more sensitive than the helix.

Resolution

Although microcoils have great advantages in terms of sensitivity and excitation bandwidths, they have not yet been embraced as a general tool in mainstream NMR research. This is mostly due to the compromises that must be made in spectral resolution. High sensitivity demands a high filling factor, so the sample will be in close contact with the rf-coil. In general the magnetic susceptibility of the metal wire differs from that of the coil former (or air in a free standing coil) and the sample holder, as a result of which local variations of the static magnetic field occur in the sample which reduce the spectral resolution. The small dimensions of the microcoil lead to field gradients over very short distances and the resulting field profile cannot be shimmed easily by macroscopic shim coils far away from the sample.

As has been shortly discussed in chapter 1, susceptibility broadening caused by a helix coil geometry close to the sample and perpendicular to the main field can be effectively remedied by immersing that coil in a medium that has the same susceptibility as copper.[11] This is because a uniform, infinitely long cylinder oriented perpendicular to the magnetic field has a uniform field in its interior.[12] Some

perfluorocarbons are available that have volume susceptibilities close to the copper susceptibility. These perfluorocarbons introduce a minimal proton background signal.[13] In fact this solution has found its way into commercial microcoil probes for capillary NMR. The successful susceptibility matching of these solenoid coils has led to extensive applications in for example the field of high-throughput screening.[14]

An alternative is to use zero susceptibility wire to avoid deterioration of the spectral resolution due to the close proximity of the coil to the sample. Zero susceptibility wire is produced by stacking of metals which have opposite signs in susceptibility such as copper and aluminum. The thickness of the layers has to be accurately controlled so that the metal volumes are consistent with the ratios of the volume susceptibilities.[12,15,16] Again, susceptibility matched coils have found their way into a number of home-built and commercial probes, showing that high resolution close to that in regular liquid probes is possible using solenoid microcoils provided that adequate measures are taken.[17] However, for planar helical coils the ultimate resolution has not yet been achieved.

In contrast to helical coils, the stripline has some properties that make the susceptibility problem much easier to handle. The first aspect is that the axis of the stripline is oriented parallel to the static field B_0. The magnetization of the copper strip is homogeneous and oriented parallel to the external field. From Maxwell's equations it can be derived that for an infinitely long strip there is no field inhomogeneity at the position of the sample, and therefore the ultimate resolution provided by the magnet should be attainable. Because of the constriction shape, the infinite long strip shape is slightly disrupted.

For a stripline, the static field distortion and susceptibility effects for the full structures were calculated using a C-programmed numerical solver. The 3D geometry of the stripline, consisting of the central line and a fluidic channel above it was defined in a static absolute homogeneous field. The 3D-space was divided in finite element sections which each were defined as dipoles having their particular material properties. The field strength at each position in the channel was computed by integrating the contribution of each dipole element.

The graph in Figure 2.6 shows the static field for a trace along the z-axis at a small distance above a micro stripline. The inset of Figure 2.6 shows the local field variations for a plane just above a stripline, including the contact pads that are tapered at an angle of 45 degrees. In the center part, the susceptibility broadening is less than 0.1 ppm.

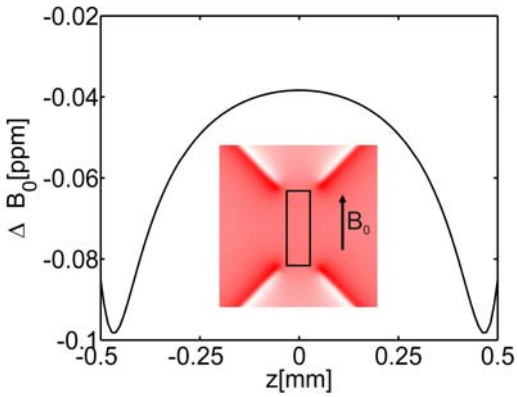

Figure 2.6. B_0-field distribution along the z-axis at a distance of 50 µm above the axis of a micro stripline with a width of 100 µm, length 1 mm and a metal thickness of 10 µm. The field inhomogeneity is below 0.05 ppm for the central part of the strip. Inset: B_0-field profile at a plane just above a micro stripline. At the edges of the contact pads a considerable field gradient was found with a maximum deviation from the center field of approximately 2 ppm. At the sample position, indicated by the solid rectangle, the field deviations are well below 0.1 ppm.

RF Power handling and excitation bandwidth

Helical microcoils offer high sensitivity because of their field factor (*i.e.* high B_1-field per unit current amplitude). This implies that the excitation bandwidth is also large, making it possible to use short π/2 pulses for wide-line solid-state NMR applications.[18] On the other hand, for narrowband applications one can work with extremely low rf-powers, typically in the 0.01-10 Watt range, thereby opening the way for low-cost integrated spectrometers. The stripline configuration as described above acts basically as a one turn coil, so the B_1-field is generally lower compared to solenoids. Nevertheless, the improved heat transfer for this configuration allows a very high excitation bandwidth. A thermal analysis was performed using both analytical calculations in Maple (Maplesoft) and 2D numerical modeling in Matlab (Mathworks). Some estimates toward the limits in rf-power handling can be made. As a first approximation it is assumed that losses are dominated by the electrical resistance of the constriction. For a freestanding wire the heat that is generated will be transported by thermal conduction through the wire towards the bulky contact pads. For simplicity it is assumed that these heat-sinks remain at ambient temperature. For a properly matched circuit all the external rf-power will be dissipated in the constriction.

The Fourier heat equation for a strip with constant cross section leads to a quadratic solution of the temperature as a function of the distance from the center of

the strip. For the 100 µm x 1 mm (5 nL) stripline described above, this translates to a 200 kHz proton excitation bandwidth at a dissipated power of only 20 mW and a CW heating profile with a maximum temperature raise of 9 K above ambient at the center of the strip. A graphical representation of the temperature profile is plotted in Figure 2.7.

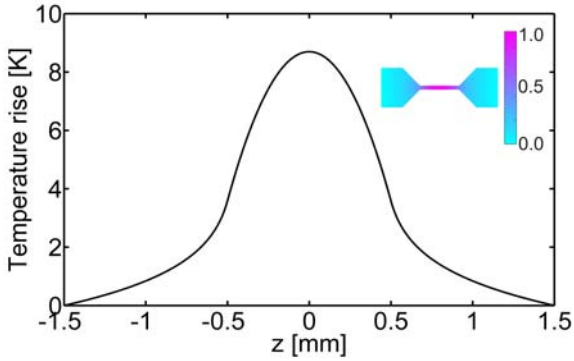

Figure 2.7. Temperature distribution in a freestanding 100 µm wide stripline subjected to an rf-power resulting in 200 kHz proton B_1-field strength. The maximum temperature rise at the center of the strip under CW conditions is 9 K. A freestanding helix that produces the same B_1-field would heat up to about twice this temperature. Inset: Temperature distribution of the strip in good thermal contact to a pure silicon substrate. The maximum temperature rise at the center is less than 1 K in this case.

This heating can be further reduced by shortening the strip, increasing the thickness (more efficient heat transport to the contacts) or by using a substrate material with a good thermal conductivity. For a strip in good thermal contact to a pure silicon substrate, the three-dimensional heat diffusion into the substrate leads to a strong reduction of the maximum temperature, and a 200 kHz CW excitation can be realized with less than 1 K temperature increase at the center of the strip (see inset Fig. 2.7). This opens the possibility for very high rf-field experiments; on pure Si substrates the strip safely allows sustained 1 MHz or higher B_1-fields in cross-polarization or decoupling sequences. Temperature heating effects under short pulsed conditions are not critical and pulsed excitation bandwidths above 10 MHz should be feasible. Note that these stripline probes, when implemented on a proper substrate, have a low loss and thus a rather high Q-factor. The effective excitation bandwidth is therefore limited by the overall probe Q-factor.

For comparison, the 5 nL helical coil described previously would produce a higher B_1-field per unit current, but as in the case of the sensitivity, the B_1-field per unit power is in fact lower than in the case of the 5 nL stripline. In this example for the same B_1-field and comparable metal cross sections, the temperature rise in a

helix is a factor 20 higher than that of the equivalent stripline. A critical point here is also that the thin wire has to be soldered onto the massive contact pads. This inevitably gives rise to additional contact resistances and less ideal cooling conditions. The stripline can be produced with micromachining techniques and does not require soldering of these small components and thermal breakdown of the rf-structure is much less of a problem.

Finally, a point of concern in NMR of biological samples with high salt concentrations is the dielectric sample heating due to rf-currents induced in the sample. In the case of the stripline structure as depicted above, the dominant electrical field component is perpendicular to the strip surface. By designing the stripline structure as a λ/2 mode structure (see below), this electrical field is zero at the center of the strip due to the symmetry of the design. Preliminary numerical simulations have shown that for liquid aqueous samples the maximum electrical fields near the ends of the constriction are about a factor 10 lower than in a comparable helix that generates the same B_1-field.

rf implementation

A typical property of microcoils in general and striplines in particular is that both the inductance and the resistance are very low. Therefore special attention to minimize losses at the contacts and to obtain good matching to the external 50 Ω circuit is required. Three convenient implementations are depicted in Figure 2.8. The first implementation shows a circuit where the stripline is built in as an inductive element in an LC-resonator circuit. Figure 2.8b shows an external λ/4 structure with the stripline inserted as a short at one side of the resonator and a capacitive coupling near the open side of the resonator. In this implementation, a standing wave is excited on the external coax. At the node of the voltage curve (top), the line is connected to ground using the stripline. The current maximum is at the node position of the voltage, warranting the highest current through the stripline. Tuning can be realized by the insertion of variable length dielectric stubs inside the coaxial resonator structure. Both implementations set high demands for the metallic connection to the central line because of the high local currents.

Alternatively, striplines can be designed as either λ/4 or λ/2 self-resonant structures (Figure 2.8c, only λ/2 is shown). In this case, the physical length of the central line should fit with either a half or a quarter of the wavelength of the excited frequency. The wavelength is a function of the dielectric constant ε, as can be

deduced from Eq. 2.15, describing the wavelength λ of an electromagnetic wave with frequency *f* propagating through an ideal transmission line:[19]

$$\lambda = \frac{v}{f} = \frac{c}{f\sqrt{\mu\varepsilon}} \qquad 2.15$$

where *v* is the propagation velocity, *c* is the speed of light in vacuum, μ the magnetic susceptibility of vacuum μ_0 multiplied by the susceptibility of the substrate μ_r, and ε the dielectric constant of vacuum ε_0 multiplied by the dielectric constant of the substrate ε_r. Figure 2.8c shows a self-resonant stripline implementation together with the current and voltage distributions.

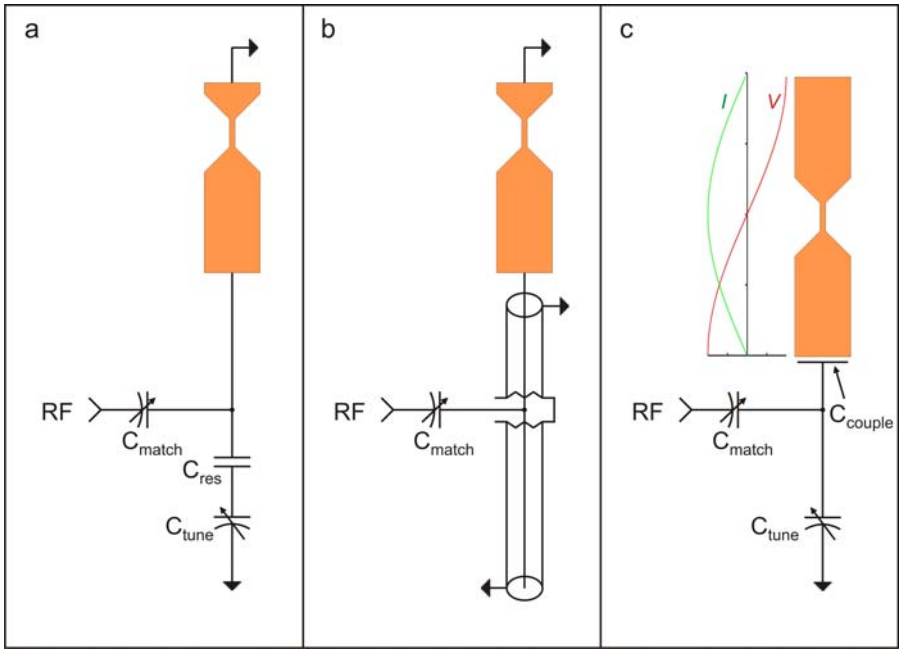

Figure 2.8. Possible stripline implementations. In all cases, only the central line is drawn.
a) Lumped element circuit. The stripline (an inductive element) in combination with C_{res} forms an LC-resonator.
b) A coaxial λ/4 resonator with a stripline as a short. The capacitive coupling to the λ/4 coax has to be chosen at a convenient point to achieve the best matching conditions.
c) A λ/2 self-resonant stripline implementation. The standing wave pattern of the current and voltage is schematically displayed. The rf-wave is coupled via C_{couple} which is large compared to C_{match} such that C_{match} is dominating the matching. Although the structure in principle should resonate at the aimed frequency, a small C_{tune} is included in the circuit, to compensate for minimal changes induced by *e.g.* sample differences which have effect on ε.

The main advantage of self-resonant structures compared to implementations based on external components is that the requirements for the rf-connections are low because they are not in the resonating line, but only weakly coupled to it. Especially, a $\lambda/2$ structure is attractive because in contrast to all other implementations the central line can be completely free-standing, which circumvents problems associated with metallic contacts. On the other hand, the integration of extra channels is difficult for self-resonant structures, whereas this is rather straightforward in the first two implementations. Furthermore, self-resonant structures require extremely careful design with respect to Eq. 2.15 to ensure resonance at the proper frequency and they are relatively long at lower frequencies.

'Proof of principle' results

Probe design

In order to establish the feasibility of striplines for NMR applications, a prototype probe was built, based on the configuration depicted in Figure 2.8b. For this prototype, a 1 mm stripline with a width of 500 µm was produced photolithographically using low-loss Teflon-based printed circuit board (PCB) material (Rogers RT/duroid 5870). Contact masks were used with high resolution structure definition. The wet etching allowed structures down to about 20 µm in size. The PCB thickness was 0.254 mm, with a copper cladding of 17 µm. The sample chamber was machined in a second layer of PCB, where the top copper layer was removed. The bottom copper layer of the sample holder acts as the second ground plane and closes the symmetric stripline configuration. Figure 2.9 shows the probe with the stripline located at the top.

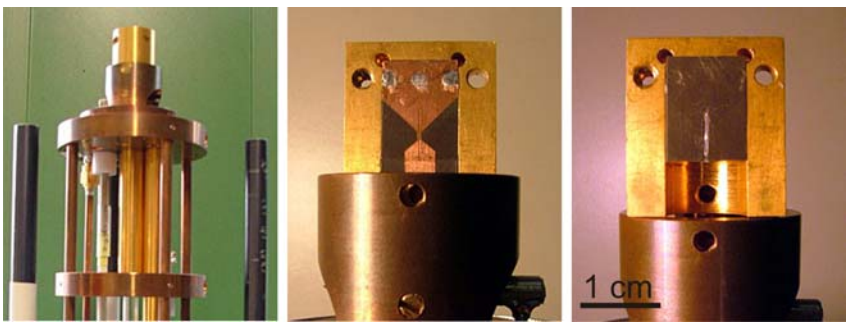

Figure 2.9. Actual photograph of the prototype stripline probe (left), showing the stripline structure (center) and the sample holder with capillary (right) and ground planes on both sides (not shown).

Methods and materials

Silicone rubber and polyethylene were both of a generic household type and used without further treatment. Ethanol (pro analysis 96%) was obtained from Merck.

All NMR experiments were carried out on a Chemagnetics CMX-Infinity 600 solid-state NMR spectrometer, operating at a magnetic field strength of 14.1 T. All data processing and spectral deconvolution was done using the matNMR processing package.[20]

rf-strength and homogeneity

Solid and liquid-state samples were used to determine the performance of this prototype probe. The first sample was a small 1 mm diameter disk of silicone rubber placed on top of the stripline. The total sample volume was 200 nL in this case. To determine the field strength and rf-homogeneity, proton nutation spectra were obtained for the narrow methyl-proton signal of the silicone rubber. The nutation curve for the silicone sample gave an rf-field strength of 90 kHz at an rf-power of 5 Watts. The $A_{810°}/A_{90°}$ pulse ratio was 62% (Figure 2.10), which is acceptable considering the fact that the sample diameter is slightly larger than the width of the strip.

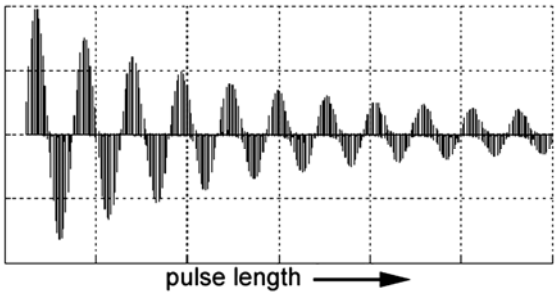

Figure 2.10. Proton nutation signal at 600 MHz for a 200 nL silicone rubber sample in an approximately cylindrical geometry of 500 µm diameter and 250 µm thickness on a 500 µm wide stripline.

Thin-film polyethylene

A very interesting application area for solid-state NMR is the study of thin-film material. To explore this capability, a film of commercial polyethylene based packaging material was placed over the stripline. This 10 µm thick foil corresponded to an effective sample volume of approximately 10 nL. A proton single-pulse excitation experiment gave an SNR of 165 in as little as 4 scans. Figure 2.11 shows a deconvolution of the spectrum which has a typical three component proton wide-line spectrum. In accordance with proton wideline studies of LDPE[21] the spectrum

can be deconvoluted into a broad Gaussian peak, a Lorentzian with intermediate line width and a narrow Lorentzian. These are attributed respectively to the rigid, semi-rigid and soft amorphous phases of the polymer. These results demonstrate the sensitivity of the stripline for thin-film wide-line NMR spectroscopy. This configuration might also be exploited for highly resolved materials imaging.

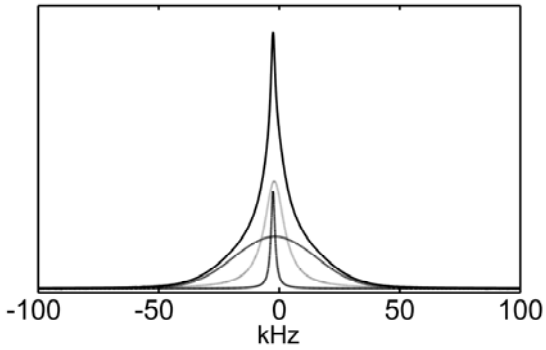

Figure 2.11. Proton wide-line spectrum of a PE foil (thickness 10 µm, volume 10 nL) measured at 14.1 T (600 MHz; 128 scans). The experimental spectrum overlaps perfectly with a deconvolution of the spectrum in a linear combination of a broad Gaussian and intermediate and narrow Lorentzian lines. The separate components are assigned to fractions with distinct differences in molecular mobility.

Liquid NMR on ethanol

To demonstrate the capabilities for liquids, a 110 µm inner diameter capillary filled with pure ethanol was placed on the stripline, with the capillary extending over the wide contact areas. The nutation spectrum in this case showed that the rf-field was considerably reduced above these contact pads, moreover the sample above the pads seriously affected the resolution. The sample volume located above the central part of the stripline was about 12 nL. The proton rf-field strength was 140 kHz at a source power of 5 W. With the experimentally determined Q-factor of the probe and the simple model based on Ampere's law, an rf-field strength of 150 kHz was expected, in good agreement with the experimental observations.

A spectrum obtained for the 12 nL ethanol sample is shown in Figure 2.12. To eliminate the broadened and shifted signal from ethanol above the contact pads, the spectrum was obtained by subtracting half of a 180° spectrum from a single scan spectrum excited under normal 90° pulse conditions. In this way signals that experience rather low rf-field strength are eliminated from the overall signal. Clearly, this can be done more efficient by implementing composite pulse methods that select for homogeneous B_1-field.[22] The single scan SNR equals 440 as

determined in the time domain. This translates to an experimental LOD of $1.5 \cdot 10^{13}$ spins per √Hz. The theoretical prediction for this geometry (including the spreading resistance of the contact areas) amounts to $1.2 \cdot 10^{13}$ spins per √Hz, which is in reasonable agreement with experiment. Note that the present capillary covers only 20 % of the stripline width, and therefore an improvement by a factor two in sensitivity is rather straightforward. The final and possibly most important parameter was the spectral resolution that could be obtained. For the proton difference spectrum of ethanol shown in Figure 2.12 a linewidth of 50 Hz, corresponding to a resolution of 0.08 ppm, was obtained. Although this is not truly a high resolution, this is sufficient to already study *e.g.* reaction kinetics for many reactions that are performed in microfluidic devices. It should furthermore be noted that this prototype probe was not designed for very high resolution work, but mainly to demonstrate the superior sensitivity.

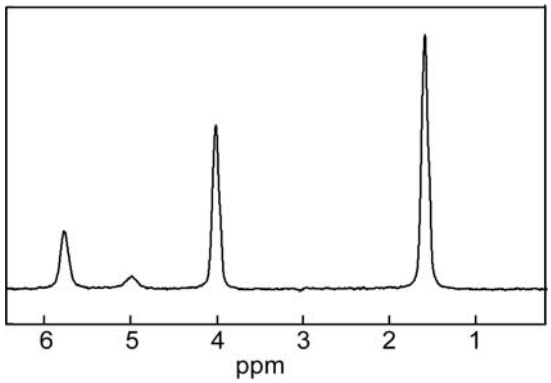

Figure 2.12. Single scan proton spectrum of a 12 nL ethanol sample obtained at 600 MHz (14.1 T) in the prototype stripline probe. The spectrum was obtained by subtracting a 180° spectrum divided by two from a single scan spectrum excited under normal 90° pulse conditions. In this way signals from sample above the contact pads that experiences a rather low rf-field strength are eliminated from the overall signal.

Discussion and conclusions

With this prototype the main conclusion from the design calculations were confirmed: very high sensitivity, high rf-field strength with good thermal characteristics and good B_1-homogeneity characteristics over a large volume of the available sample space around the structure. The ultimate spectral resolution was not reached in this implementation, which was addressed to the massive copper parts in between which the stripline was clamped.

One can easily optimize the stripline configuration for various sample sizes and concentrations. For example, in the case of microfluidic on-chip analysis the aim is to optimize the SNR for low concentration solutions. The main guideline is to have a sufficient number of nuclear spins in the detection volume. This number is limited by the acceptable sample volume and concentration. Assuming that 5 μL is an acceptable sample volume, the discussed 5 nL design can be scaled up by a factor 10 in size (1 mm strip width, 10 mm length). Although the absolute sensitivity decreases linearly with this scale factor, the concentration sensitivity increases quadratically with the scale factor and one may expect that a 10^{-1} M solution can be detected with an SNR of about 25 in a single scan (assuming again a spectral linewidth of 0.01 ppm). This would *e.g.* allow relatively fast 'realtime' screening of HPLC output flows or the study of reaction kinetics on-chip.

Many interesting samples are two-dimensional in nature, such as coatings, epitaxial layers, molecular beam epitaxy (MBE) grown films etcetera. With helical NMR detection coils these samples are difficult to handle. Removing the surface layer and transfer of the resulting powder to a cylindrical sample holder could result in structural changes and information about preferential orientation and ordering may be lost. Sometimes it is possible to cut the substrate in bars and stack these in the cylindrical NMR probes. Apart from the low filling factor, this will lead to destruction of the sample. Moreover, lossy and/or metallic substrates are difficult to handle with this procedure. Striplines give additional options: it is imaginable to replace one of the metal ground planes with such a coated metallic substrate and detect the nuclear spins in the surface layer non-destructively, thereby maintaining the full information content. In fact, one can even think of a *xy*-scanning stage where the local information is measured as a function of the position.

A third sample geometry is encountered for single crystals or biological fibers that are inherently small in size, difficult or expensive to synthesize because of isotopic labelling etcetera. For a needle shaped crystal, the width and length of the stripline can easily be adjusted to match the sample dimensions. Looking at quasi-cubic crystals of approximately $(10\ \mu m)^3$, both width and length of the strip can be reduced to obtain a theoretical LOD of $3 \cdot 10^{11}$ spins per $\sqrt{Hz}$.

In summary, the proposed stripline configuration represents a simple and effective design for mass-limited NMR samples that is easy to produce with micromachining methods. Attractive points are the fact that the sensitivity can be competitive with optimized helical coils and many of the problems encountered in planar helices are absent. In essence, the high sensitivity and high B_1-field of the helical microcoils is conserved. The simple planar design allows a quantitative

modelling of both static and high frequency components using analytical or 2D and 3D finite element analysis. A strong advantage of the present design is its scalability. The same approach can be used both for large surface layers, small diameter cylindrical samples or tiny crystals.

References

[1] K. Woelk, *J. Magn. Reson.* 146 (1), 157 (2000).
[2] D. Canet, *Prog. Nucl. Magn. Reson. Spectrosc.* 30, 101 (1997).
[3] I. Ardelean, R. Kimmich, *Isr. J. Chem.* 43 (1-2), 9 (2003).
[4] The high frequency finite element analyses shown in Fig. 2.1 and 2.3 were carried out using FEMM, http://femm.foster-miller.net/wiki/HomePage, David Meeker, dmeeker@ieee.org.
[5] Y. Maguire, I.L. Chuang, S.G. Zhang, N. Gershenfeld, *Proc. Nat. Ac. Sci. USA* 104 (22), 9198 (2007).
[6] H.G. Krojanski, J. Lambert, Y. Gerikalan, D. Suter and R. Hergenroder, *Anal. Chem.* 80, 8668 (2008).
[7] D.I. Hoult, R.E. Richards, *J. Magn. Reson.* 24, 71 (1976).
[8] D. Horne, R.D. Kendrick, C.S. Yannoni, *J. Magn. Reson.* 52 (2), 299 (1983).
[9] S. Eroglu, B. Gimi, B. Roman, G. Friedman, R.L. Magin, *Concepts Magn. Reson. Part B Magn. Reson. Eng.* 17B (1), 1 (2003).
[10] H. Wensink, F. Benito-Lopez, D.C. Hermes, W. Verboom, J.G.E. Gardeniers, D.N. Reinhoudt, A. van den Berg, *Lab Chip* 5 (3), 280 (2005).
[11] D.L. Olson, T.L. Peck, A.G. Webb, R.L. Magin, J.V. Sweedler, *Science* 270 (5244), 1967 (1995).
[12] A.G. Webb, *Prog. Nucl. Magn. Reson. Spectrosc.* 31, 1 (1997).
[13] D.L. Olson, M.E. Lacey, J.V. Sweedler, *Anal. Chem.* 70, 645 (1998).
[14] Y. Lin, S. Schiavo, J. Orjala, P. Vouros, R. Kautz, *Anal. Chem.* 80, 8045 (2008).
[15] F.D. Doty, G. Entzminger, Y.A. Yang, *Concepts Magn. Reson.* 10 (5), 327 (1998)
[16] F.D. Doty, G. Entzminger, Y. A. Yang, *Concepts Magn. Reson.* 10 (5), 329 (1998).
[17] A.G. Webb, *J. Pharm. Biomed. Anal.* 38 (5), 892 (2005).
[18] K. Yamauchi, J.W.G. Janssen, A.P.M. Kentgens, *J. Magn. Reson.* 167, 87 (2004).
[19] L.V. Blake, *Transmission Lines and Waveguides*, John Wiley & Sons, Inc., New York (1969).
[20] J.D. van Beek, *J. Magn. Reson.* 187, 19 (2007).
[21] C. Hedesiu, D.E. Demco, R. Kleppinger, A.A. Buda, B. Blumich, K. Remerie, V.M. Litvinov, *Polymer* 48 763 (2007).
[22] A. Bax, *J. Magn. Reson.* 65, 142 (1985).

– Chapter 3 –

Optimization of stripline-based microfluidic chips for high-resolution NMR

Parts of this chapter will be published as:

J. Bart, J.W.G. Janssen, P.J.M. van Bentum, A.P.M. Kentgens, J.G.E. Gardeniers, *J. Magn. Reson.* accepted, (2009).

Introduction

In the previous chapter, solenoids, planar coils and striplines were compared with respect to resolution and sensitivity. In this chapter, an optimization study in terms of rf-homogeneity, resolution and sensitivity will be presented. Based on these optimizations, a Lab-on-a-Chip implementation was realized. The performance of this device is compared to modelling results.

Lab-on-a-chip implementation

The 3D structure of a stripline, shown in Figure 2.1 was aimed to be implemented as a fluidic Lab-on-a-Chip device utilizing common microfabrication technology. In view of fabrication simplicity, a construction based on two substrates was chosen, one carrying the central strip and one containing a single fluidic channel. Ground planes were applied on the backsides of both substrates resulting in the configuration shown in Figure 3.1.

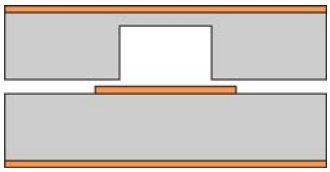

Figure 3.1. Lab-on-a-chip implementation based on two substrates. The central strip is defined on the bottom substrate and the sample chamber in the top substrate. Ground planes are defined at the backsides of both substrates. Clearly, for a working device these two substrates have to be merged to achieve a leak-free structure.

In regular NMR probes the rf-coil is implemented as an inductive element (L) in an LC resonator. This means, that discrete elements have to be soldered to the rf-coil. Striplines offer the possibility to be designed as self-resonant structures, which makes the need for soldering external electronics unnecessary. When the central strip is designed as a $\lambda/2$ length of the Larmor frequency of the nuclei to be observed, a standing wave can be excited on it, as shown in Figure 3.2a. The current is maximal in the middle of the strip and at this position the strip has a constriction, which increases the local current density resulting in a strong rf-field at the position of the sample (fig. 3.2b). The transition from the constriction to the so-called wide zone is tapered, for reasons discussed below.

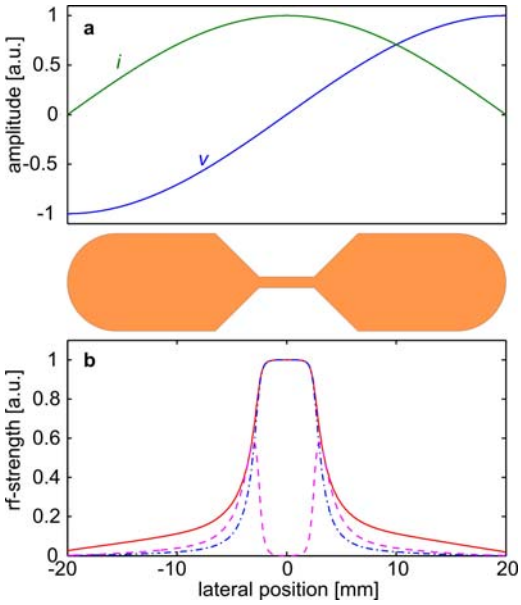

Figure 3.2. a) The standing wave pattern excited on a λ/2 stripline resonator, schematically displaying the lateral current (i) and voltage (v) distribution. b) The lateral rf-field (solid red line, numerically determined) and the lateral signal intensity after a 90° pulse (blue dash-dot line). The constriction clearly enhances the local current density. Because of the finite diameter of the wide zone and more importantly the tapering, a residual signal after a 180° pulse is visible (purple dashed line).

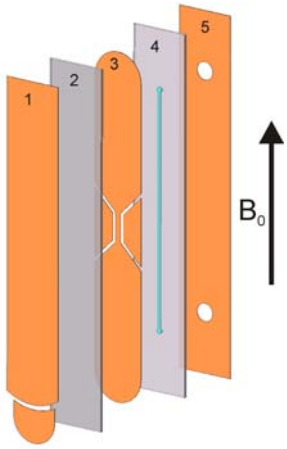

Figure 3.3. Exploded view of a λ /2 stripline-based NMR chip. Layer 1: grounded copper plane. The small separate plane represents the capacitive coupling to the external electronics. Layer 2: substrate. Layer 3: central line feeding the rf-current. A constriction is defined by removal of narrow copper lines. The remaining trapezoid shaped copper planes are electrically isolated. Layer 4: substrate containing a microfluidic channel. Access-holes are in the backside. Layer 5: grounded copper plane with microfluidic access-holes.

Since the coil is used both for excitation and detection, the effective signal contribution as a function of the position along the channel shows that the sample at the position of the constriction dominates the detected signal. Figure 3.3 shows an exploded view of a self-resonant stripline according to the description above.

Substrate choice and modification

We aimed for an NMR chip which could be fabricated by means of common microfabrication technology. For the NMR detector described here, silicon was used as a substrate. Silicon is an absolute proton-free substrate, which assures flat baseline spectra without any background resonances. Furthermore, a very wide manufacturing infrastructure for silicon fabrication exists which makes fabrication of this chip, as well as future integration with electronic or microfluidic functionality straightforward. Finally, the high dielectric permittivity ε_r of silicon limits the total length of the chip when it is designed as a $\lambda/2$ resonator. Eq. 3.1 gives the wavelength λ of an electromagnetic wave with frequency f propagating through an ideal transmission line:[1]

$$\lambda = \frac{v}{f} = \frac{c}{f\sqrt{\mu\varepsilon}} \qquad 3.1$$

where v is the propagation velocity, c is the speed of light in vacuum, μ the magnetic susceptibility of vacuum μ_0 multiplied by the susceptibility of the substrate μ_r, and ε the dielectric permittivity of vacuum ε_0 multiplied by the dielectric permittivity of the substrate ε_r.

Using a semi-conducting material as a substrate is not trivial considering the high frequencies at which ^{1}H-NMR usually operates (300~1000 MHz). This is due to the free charge carriers present in the standard bulk silicon which contribute significantly to the total losses of the detector. This is especially the case for a stripline configuration where the electrical field component of the rf-wave is perpendicular to the substrate. Substrate induced losses are usually denoted by the loss factor tan δ, which is inversely proportional to the quality factor Q (tan $\delta = 1/Q$). The loss factor of bulk silicon can be split in tan δ_C which is the contribution of the conductive losses caused by the finite resistivity of the substrate, and tan δ_P which is defined as the polarization loss caused by ionic and electronic polarization:[2,3,4]

$$\tan\delta = \frac{\sigma}{\omega\varepsilon_0\varepsilon_r^{'}} + \frac{\varepsilon_r^{''}}{\varepsilon_r^{'}} = \tan\delta_C + \tan\delta_P \qquad 3.2$$

where σ is the substrate conductivity, ω is the angular frequency and ε'_r and ε''_r are the real and imaginary part of the dielectric permittivity respectively. For ideal dielectrics having a very low σ, the first term is negligible and the losses are determined by the complex permittivity only. However, the abundant free charge carriers in silicon make tan δ_C dominant up to high frequencies, and tan δ_P begins to dominate in the high GHz range. To keep tan δ_C minimal, high-purity silicon with a minimal amount of free charges was used.

Apart from the bulk-conductivity induced losses, surface losses have to be considered. At the interface between the silicon and an insulating layer (*e.g.* oxide), a charge accumulation layer (also called a surface channel) is formed due to dangling silicon bonds and fixed charges in the SiO_2.[5,6,7,8,9] The amount of accumulated charge is about an order of magnitude larger than the total amount of mobile charge present in the bulk,[7] which makes this layer very conductive and thus lossy. The surface conductivity can be decreased by making the substrate surface amorphous, thereby decreasing the carrier mobility. Amorphous silicon (α-Si) can be deposited by means of Plasma Enhanced Chemical Vapour Deposition (PECVD)[8] or Low Pressure Chemical Vapour Deposition (LPCVD).[9] Another approach to achieve a damaged crystal structure is the implantation of high energetic argon ions in the substrate.[5,6,7] All these methods proved to be effective surface loss suppression techniques, making the bulk induced loss mechanism dominant. By using a high resistivity silicon substrate (to minimize bulk silicon induced losses) and surface amorphisation (to minimize the surface channel losses), silicon can be made suitable for rf-applications.

Computational modelling and optimization

The performance of an NMR detector is commonly expressed in three entities: the rf-homogeneity, the resolution and the sensitivity. The dimensional ratios (*w/d* and *l/w*) of the detector influence these entities and can be optimized. For the stripline, our strategy was to aim for a maximal sensitivity for a specified rf-homogeneity maintaining the optimal resolution. Of course, the design should be feasible for practical implementation, that is, fabrication limitations were taken into account.

rf-homogeneity

A high rf-homogeneity is of importance for complex spin manipulations based on successive pulses along different axes. When the rf-field is inhomogeneous, not every spin gets the same tip angle, which means that after a few pulses the

magnetization is scrampled which affects the final SNR. Usually, the rf-homogeneity is determined by means of a so-called nutation experiment, in which the signal amplitude is recorded for increasing pulse lengths. The ratio of the signal amplitudes after an 810° and a 90° pulse ($A_{810°}/A_{90°}$ ratio) is a common measure for the rf-homogeneity. Commercial saddle-coil based liquid-state probes show $A_{810°}/A_{90°}$ ratios in the order of 80%. This value is adopted as a starting point in the present optimization.

Nutation can be very well predicted using finite element methods for the representation of the generated rf-field. For the stripline, the cross-sectional rf-field distribution at the centre of the constriction was computed using Finite Element Methods for Magnetics (FEMM).[10] Typical pictures are shown in the insets of Figure 3.4a. Simulations were performed for varying stripline width with respect to the distance of the ground planes, expressed as *w/d*.

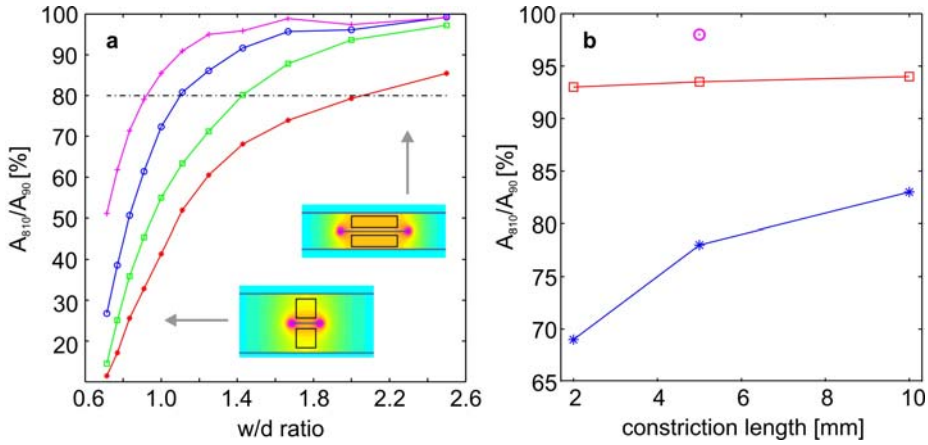

Figure 3.4. a) *w/d* ratio dependence of the rf-homogeneity for 4 different filling factors. For these simulations a filling factor of 100% corresponds to a sample size of *w*×*d*. Samples were scaled equally in both dimensions. Purple line (+): sample size = 0.55*w*×0.55*d*, filling factor = 30%. Blue line (o): sample size = 0.67*w*×0.67*d*, filling factor = 45%. Green line (□): sample size = 0.77w×0.77*d*, filling factor = 60%. Red line (*): sample size = 0.87*w*×0.87*d*, filling factor = 75%. The insets give an indication of the geometry for the limits of the the *w/d* ratios in the graph. For clarity reasons, only the 0.67*w*×0.67*d* sample area is shown, which has an $A_{810°}/A_{90°}$ ratio of 80% for *w/d*=1.
b) Effective rf-homogeneity for a finite length sample plug centered on the stripline as indicated by Figure 3.2, (*w/d*=1, channel depth = 300 µm, channel width = 400 µm, constriction length = 5 mm). The red line (□) shows the data for a plug of 0.75× the length of the constriction, the blue line (*) represents the data for a sample as long as the whole stripline and the purple dot (o) is the rf-homogeneity for a circular sample plug with a length of 3.75mm (0.75× the length of the constriction) and a diameter of 100 µm (see text).

Small *w/d* ratios are expected to yield a low homogeneity (and with that a low filling factor) because they approach a circular wire which intrinsically has a low homogeneity. This is in agreement with the simulations shown in Figure 3.4a, which predict a decrease in effective filling factor (which we here define as the area within *w*×*d* where the rf-homogeneity is >80%) for low *w/d* ratios. In the insets, the sample chambers are indicated with black lines. Compared to solenoids and planar coils the stripline shows a largely improved filling factor for a given rf-homogeneity.[11] It has to be noted that these simulations are valid for every size of the detector, as long as the aspect ratio *w/d* is kept constant. From this graph it is concluded that the *w/d* ratio should be maximized to obtain the best rf-homogeneity. However, for small sample volumes (below 1 µL) the *w/d* ratio is limited by what is possible to be fabricated; too low *w/d* ratios lead to impractical designs because extremely thin substrates have to be used. Practical numbers for *w/d* are found to be between 1 and 1.5.

The rf-homogeneity was also modelled for the specific construction based on two substrates (Fig. 3.1). In this design the sample is positioned directly on top of the central line. Substrates of 525 µm thickness were used in which a channel was etched with a width of 400 µm and a depth of 300 µm. The stripline width was 1 mm, resulting in a *w/d* ratio of 1. For fabrication reasons, this channel was kept rather narrow compared to *w*, resulting in a moderate filling factor, however, with a simulated $A_{810°}/A_{90°}$ ratio of 90%.

Apart from cross-sectional rf-inhomogeneities, lateral inhomogeneities were studied based on 3D rf-data sets, obtained by simulations in CST Studio Suite.[12] First, a sample plug with 0.75× the length of the constriction and a diameter as indicated in Figure 3.1 (channel width of 400 µm and depth of 300 µm) was examined for different constriction lengths. Since the rf-field is fairly homogeneous across this region (as indicated by Fig. 3.2b) the simulated $A_{810°}/A_{90°}$ ratio was maintained well above 90% for all studied lengths, see Figure 3.4b. This means that for plug-flow applications, a simple rf-homogeneity prediction based only on the cross-section of the channel is sufficient. For completely filled channels, the simulated $A_{810°}/A_{90°}$ ratio decreased, because of the sample regions under the tapering which experience a weaker rf-excitation. For a sample with the same length as the whole central line, the $A_{810°}/A_{90°}$ ratio decreases more rapidly for shorter constrictions. This is logical since the relative impact of the tapering is more dominant. For a constriction length of 5×*w*, an rf-homogeneity of 78% was calculated for the design of Figure 3.1.

Sensitivity

As has been stated by Hoult and Richards, the Signal to Noise ratio (SNR) of an NMR experiment scales according to:[13]

$$SNR \approx \frac{\left(\frac{B_1}{i}\right)}{\sqrt{R}} \qquad 3.3$$

where B_1/i is the rf-field generated per unit current and R is the total resistance of the detector. Assuming a proper rf-homogeneity (in our case >80%) B_1/i and R are determined by the ratio of the length and width of the constriction, l/w. Therefore, for a given sample volume and a fixed w/d ratio (being 1 in our case) the optimal sensitivity can be found by varying the l/w ratio. An optimum (taking the tapering resistance into account) was found for an l/w ratio between 5 and 10, as shown in Figure 3.5. For a steeper tapering (towards 90°) the maximum is higher and shifts to the left. Therefore, a steeper tapering gives a better sensitivity, but is disadvantageous in terms of susceptibility broadening (see for motivation the resolution section below). In our implementation a tapering angle of 45° was chosen and the total length was set by the resonance condition (48 mm for 600 MHz, see below). With these settings an optimal l/w of 5 was found.

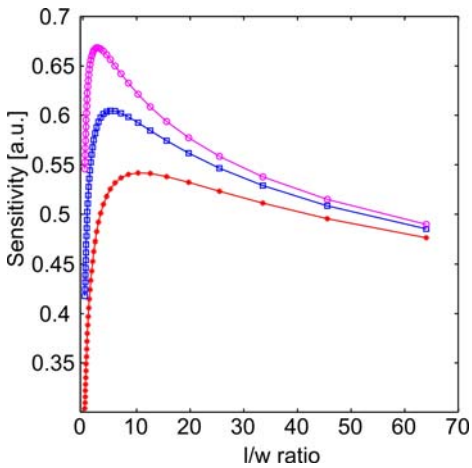

Figure 3.5. Sensitivity as function of the l/w ratio. Tapering and wide zone are taken into account. Red line (*): tapering 25°. Blue line (□): tapering 45°. Purple line (o): tapering 65°.

Resonance condition

As mentioned earlier, the length of the stripline determines the standing wave length which can be excited in the stripline. The length must be adjusted very carefully in order to make the chip compatible with a chosen Larmor frequency. Although calculations and simulations with lumped elements in an electrical circuit were performed in which the bulk induced losses were implemented, it turned out to be extremely difficult to predict the resonator length with a sufficient precision. Accurate size parameters had to come from 3D numerical simulations, which were performed based on the optimized parameters described before. For a stripline operating at 600 MHz with a constriction of 1×5mm ($w \times l$), a tapering of 45° and a wide zone width of 9 mm, the self-resonance length was calculated to be 48 mm for a stripline on a silicon substrate.

Resolution

Since the stripline is positioned parallel to the static field (z-axis), minimal susceptibility broadening is expected. Nevertheless, magnetic susceptibility transitions along the z-axis such as the ends of the fluidic channel and the edges of the tapering will limit the final resolution. In order to study these effects, calculations were performed using a C-programmed numerical solver. The 3D geometry of the chip, consisting of the stripline and the fluidic channel, was defined in a static homogeneous field. The non-patterned substrate and ground planes were left out of consideration since they are very large compared to the sample and therefore have negligible influence on the susceptibility broadening. The whole 3D-space was divided in finite element sections which each were defined as dipoles having their particular material properties. The lineshape was predicted by summing the effects of all the dipoles in the 3D-space for every position in the channel. With these simulations, the crucial design parameters influencing the susceptibility broadening were studied. Figure 3.6 shows which parameters are varied.

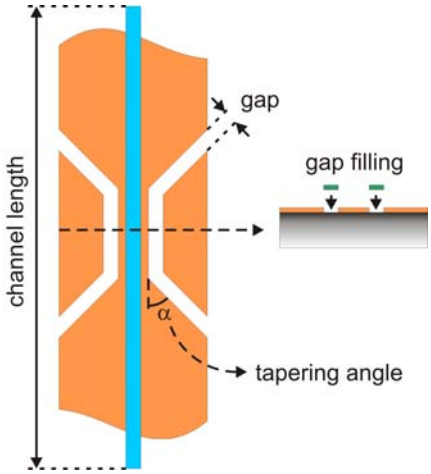

Figure 3.6. Parameters which are varied for optimization of the resolution. In the text, these parameters are described in detail.

Figure 3.7a shows the predicted NMR lineshapes for different channel lengths. Apparently, shortening the channel has a negative effect on the linewidth. This is because the ends of the channel where the magnetic permeability switches from sample (*e.g.* water) to silicon. Therefore, the channel should be long compared to the constriction to keep these distortions far away from the detection area. When there is no practical limitation, the best is to design the fluidic in- and outlets close to the edge of the chip, as we have done in the current implementation.

In terms of sensitivity it was shown that a tapering angle α of 90° exhibits maximal sensitivity. However, such an angle means a sudden 'discontinuity', resulting in a B_0-gradient in the channel above the constriction. Low values for α are therefore advantageous in terms of resolution, but will lead to a decrease in sensitivity and a poor sample selection. Therefore, we compromised choosing an angle of 45°.

Earlier simulations have shown that for a simple copper structure without any susceptibility matching the distortion of the B_0-field could be limited to below 0.1 ppm.[11] The main cause for the B_0-field distortion was found to be the tapering, being designed by removal of all the copper around the constriction (as schematically shown in Fig. 3.2). To limit this susceptibility broadening, one has to realize that it is not necessary to remove all copper to construct the narrow strip section. Starting from a uniform strip without a constriction, one can make a constriction by defining a gap as is shown in Figure 3.6. Such a design effectively routes the rf-current in the narrow constriction, but leaves nearly all the copper which means a minimal disruption of a long uniform strip. Figure 3.7d compares the local B_0-field variations

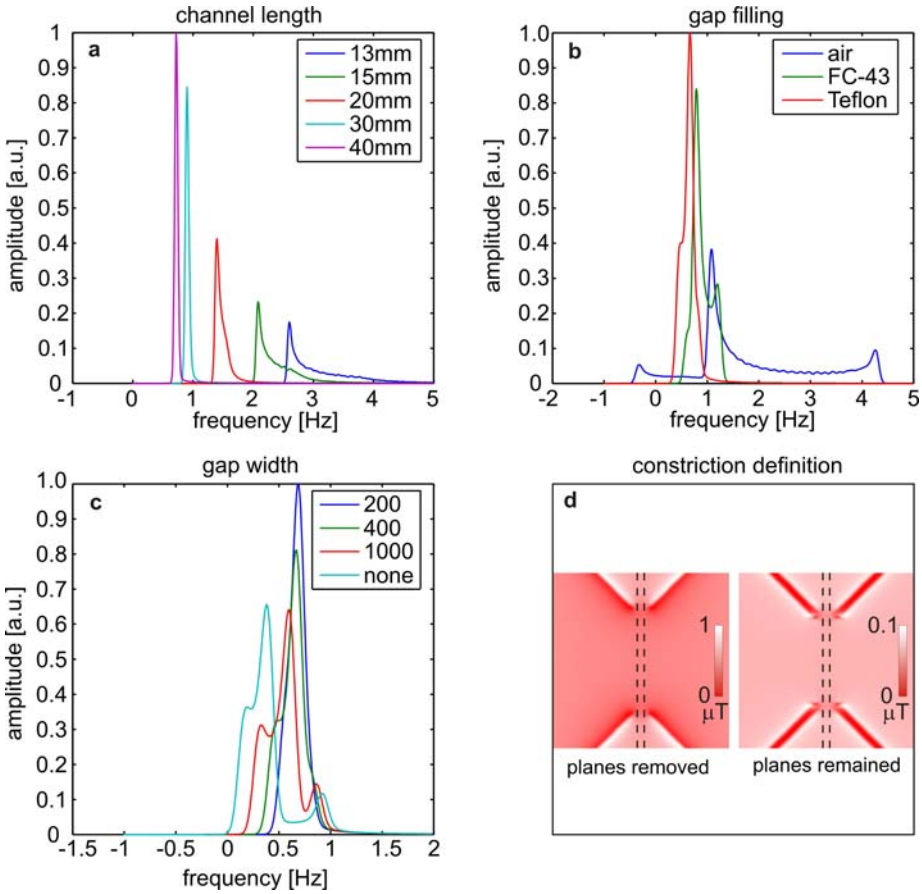

Figure 3.7. a) Predicted line shapes for channel length variations. Distortions caused by the copper structure are cancelled, to visualize only channel length effects.
b) Predicted line shapes for variations of the gap filling. The channel length is set to 40 mm and the gap width to 400 µm.
c) Predicted line shapes for gap width variations. The channel length is set to 40 mm and the gap is filled with FEP (see text).
d) 2D simulation of the local field variations in a plane 150 µm above the central strip for a constriction defined by removal of all the copper around it (left), and defined by a gap (right). The channel is indicated with dashed lines. The B_0-field distortion along the channel defined by a gap is lower than the one defined by removal of all the copper. Note the scale difference in both pictures.

of a stripline which is defined by removal of all the copper around the constriction, and one which is defined by a gap. Clearly the local field variations can be diminished by means of this approach.

The B_0-field distortion can be minimized further by filling the gap with a material having a susceptibility closely matching that of copper (χ_{Cu}=-9.60E-6), as shown in Figure 3.7b. Of course, for the choice of this filling one is limited to proton-free

materials like fluorocarbons. Furthermore, since a fluidic susceptibility matching material is not easily implemented in the current design, a solid film is preferable. Fortunately, the susceptibility of Polytetrafluoroethylene (PTFE) closely matches that of copper (χ_{PTFE}=-10.5E-6 is 9.4% within χ_{Cu}).[14] Fluorinated Ethylene Propylene (FEP) is expected to have almost the same χ and is available as a thin film. For comparison, the effect of the well-known FC-43 susceptibility matching fluid (χ_{FC-43}=-8.23E-6 is 14.3% within χ_{Cu})[15] is also shown, which exhibits similar results.

Fig 3.7c shows that a decrease in gap width results in a higher resolution. This is in agreement with expectations since the discontinuities decrease in size. However, the sensitivity is negatively affected by a decrease in gap width, because of enhanced eddy-currents induced by the central line in the isolated copper planes. The optimal gap width, for which the SNR in the frequency domain is maintained and the resolution is maximized, is found between 200 and 400 μm. This result is based on a gap filled with FEP. With these settings, the susceptibility broadening is calculated to be below 0.5 Hz at 14.1 Tesla.

Fabrication and methods

A microfluidic chip as schematically displayed in Figure 3.3 was fabricated on two silicon substrates which were treated in order to minimize losses. The optimal dimensional ratios described above (w/d=1 and l/w=5) were adopted in this implementation, as well as the optimal results obtained from the susceptibility broadening simulations (gap width of 400 μm and a gap filling with FEP). A detailed process flow of the chip can be found in Appendix A.

Chip fabrication

The 300 μm deep channel and the in- and outlets were fabricated by means of Deep Reactive Ion Etching (DRIE) using a standard Bosch process with SF_6 as etch-gas and C_4F_8 for passivation.[16] After etching the channel, the surface was protected with a foil, and patterned from the backside with holes for the in- and outlet. These were etched completely through, making the channel accessible from the outside.

The α-Si was deposited by means of a modified LPCVD process on all the wafers.[17] Before deposition the wafers were successively cleaned in freshly prepared 100% HNO_3 (Selectipur: Merck) and 69% boiling HNO_3 (VLSI: Merck). Deposition was performed for 217 minutes at 550°C with a SiH_4 flow of 25 sccm. The pressure was regulated to 1.0 mbar by N_2. After unloading, the wafers were immediately covered at both sides with SiO_2 by means of a PECVD process (300°C, SiH_4 flow: 425

sccm, N_2O flow: 710 sccm, pressure: 1.3 mbar). Both layers had a thickness of 500 nm as measured with a height profile measurement.

To define the copper structures, a 16 nm titanium adhesion layer and 200 nm copper seed layer were sputtered over the unpatterned wafer. Thick AZ9260 (Clariant, Wiesbaden, Germany) resist was lithographically patterned on the wafer with a thickness of 25 μm to define the copper structure. A dedicated electroplating set-up, based on Slotocoup HL10 bath chemistry (Schlötter GmbH, Geislingen, Germany) and a DμP(R)10-1-3 powersupply (Dynatronix Inc., Wisconsin, USA) operating in DC-mode, was utilized. 30 minutes plating at 1 A/dm^2 yielded a copper layer with a thickness of 10 μm (>3 times the skin depth of copper at 600 MHz). After the resist was removed, the remaining seed layer was removed by ion beam etching (IBE) to isolate the separate structures electrically. The ground planes were fabricated with the same process after bonding.

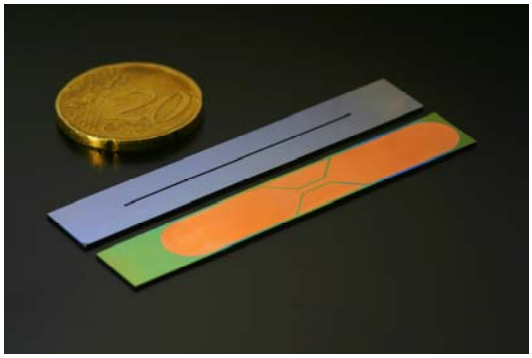

Figure 3.8. The two halves of the microfluidic chip fabricated on silicon substrates before bonding.

Bonding is the process in which the two wafers are merged together, such that they are leakage free and mechanically stable. Because of the α-Si layer and the copper stripline, bonding methods based on high temperatures like fusion bonding[18] and anodic bonding[19] were inapplicable. At the first glance, intermediate layer bonding[19] is the most obvious wafer bonding technique for the stack described here. However, since most intermediates are hydrogen-rich polymers, the choice is severely limited by the chemical composition. A completely fluorinated polymer would be the optimal intermediate, but these molecules can not establish a covalent bond with the SiO_2 surface. For these reasons we have developed a new bonding method based on an intermediate layer as is described in Chapter 8.[20] As an intermediate, we used Fluorinated Ethylene Propylene (FEP 100A), a copolymer of hexafluoropropylene and tetrafluoroethylene, (DuPont, Sabic Innovative Plastics Snij-Unie, Enkhuizen,

The Netherlands). FEP 100A film is a transparent thermoplastic with a thickness of 25 µm. Aligned bonding was performed on an EVG-620 mask-aligner in combination with an EV-501 anodic bonder. Both wafers were aligned with a FEP foil in between. During bonding, a force of 100 N/cm^2 was applied for 14 hours. It was observed that the applied force was enough to squeeze the FEP (which is deformable) in the gap around the constriction. This was necessary to obtain a proper susceptibility matching. The established bonds were strong enough to withstand the applied pressures (< 2 bar). Figure 3.8 shows a photograph of the two halves of the chip before bonding.

Probe fabrication

Special attention was given to the symmetry and simplicity of the probehead positioned in the top of a custom-designed probe (Fig. 3.9a). The top part of a long aluminum cylinder (9 mm ID, 11 mm OD, length 60 cm) was divided in two halves. Small trenches of 0.5 mm deep were milled in both halves in which the 1 mm thick chip could be placed, resulting in a non-radiative cylindrical structure (Fig. 3.9b). The return line connection was established by the direct contact between the copper shielding planes and the aluminum. This geometry keeps the holder metal far away from the sensitive area of the chip, warranting low influence on the B_0-homogeneity.

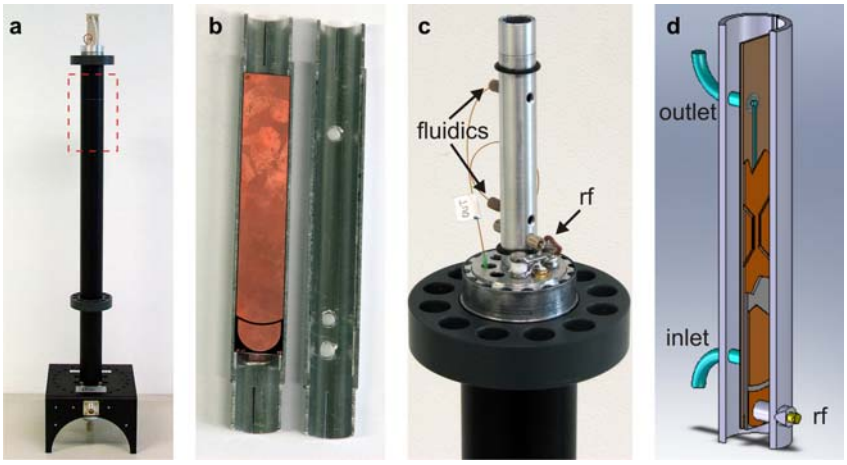

Figure 3.9. a) The complete probe. The dashed line indicates the position of the NMR chip.
b) The two halves of the aluminum cylinder showing how the chip is mounted.
b) The probehead. The chip is positioned in an aluminum cylinder in which fluidic access-holes are drilled from one side and an rf access-hole is drilled from the other side. The matching and tuning circuit is placed on the horizontal platform close to the rf-connector.
c) Schematic representation of the mechanical arrangement of the microfluidic chip in the holder.

Holes were drilled in the sidewalls of the cylinder to connect the microfluidic capillaries and the rf-contact (Fig. 3.9c). Figure 3.9d gives a schematic representation of the mechanical arrangement of the microfluidic chip in the holder.

Although the resonance frequency of the chip is intrinsically determined by the length of the stripline, small changes will be induced by sample parameters like the dielectric permittivity and losses (Eq. 3.1). Therefore, external fine-matching and fine-tuning capacitors were connected according to Figure 2.8c (see Fig. 3.9c).

Materials

Float zone High Resitivity Silicon (HRS) wafers with a resistivity of 10.000 Ω·cm, a thickness of 525 μm and a diameter of 100mm were purchased from Topsil, Denmark. 99.99% D_2O, ethanol (96% pro analysi) and isopropanol (pro analysi) were purchased from Aldrich Chemical. 99.5% Sucrose was purchased from J.T. Baker (Deventer, The Netherlands). D-glucose-1-^{13}C was purchased from CAMPRO Scientific (Veenendaal, The Netherlands). All chemicals were used as received.

NMR experiments

The NMR experiments were carried out on a Chemagnetics CMX-Infinity 600 solid-state NMR spectrometer (600 MHz) operated by Spinsight software. All spectra were recorded at 300K and processed by using the MatNMR processing package.[21]

The capillary which was used for nutation of a sample plug was sealed with Delo photobond 4436 (Delo industrial adhesives, Germany).

Experimental results

Electrical performance

The substrates were investigated with respect to dielectric losses in a home-built low-loss LC resonator, in which the substrate was introduced as a dielectric. Since the losses of the inductor (L) in this device were minimized, the measured losses could be contributed to the substrate only.

Before α-Si deposition the substrates were tested, but no resonance could be established, indicating high losses at the surface. After passivation (by means of an LPCVD process), resonance could be obtained with a Q-factor of 37, which is equivalent to a tan δ of 0.027. This is in very good agreement with the value calculated for the previously described silicon as a substrate for a stripline operating at 600 MHz. Using Eq. 3.2, a value for tan δ_C of 0.025 ($\varepsilon'_{r\,Si}$ is 11.9) was calculated. The α-Si passivation layer was also examined by X-ray Diffraction (XRD). These

measurements showed no preferential crystal orientation in the deposited layer, indicating an amorphous morphology.

rf-homogeneity

The results of the nutation simulations were experimentally verified. First, the whole chip was filled with a 100% ethanol sample. Figure 3.10a shows a sequence of spectra, recorded with different pulse widths. From this, an $A_{810°}/A_{90°}$ ratio of 76% was measured, which is in excellent agreement with simulations that predicted 78%. To get rid of the signal contributions from the sample under the tapered section of the stripline, a 40 mm fused silica capillary (100 µm ID, 200 µm OD) was filled with a 3.75 mm plug of 100% ethanol and restricted between two Fluorinert (FC-40) plugs of 15 mm length. For such a small sample volume, an $A_{810°}/A_{90°}$ ratio of 98% was predicted (purple dot in Fig. 3.4b). The capillary was positioned in the chip, such that the ethanol plug was symmetrically positioned under the 5 mm long constriction, where after the same nutation was run again. Figure 3.10b shows the nutation plot of this experiment, from which an $A_{810°}/A_{90°}$ ratio of 99% was obtained, again completely according to the simulations.

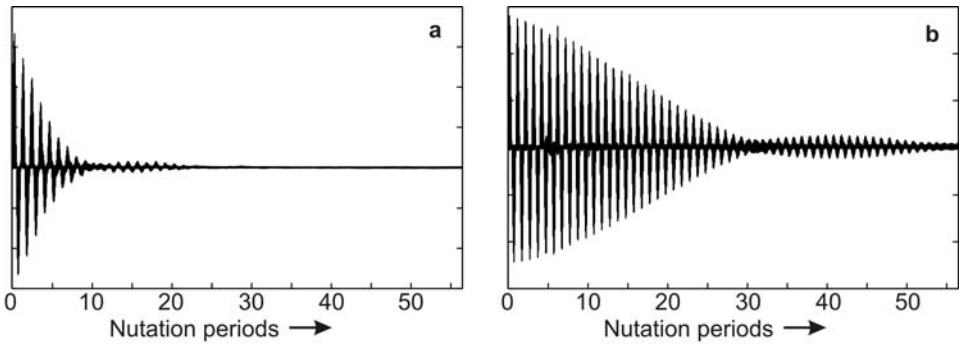

Figure 3.10. Proton nutation signal at 600 MHz for different sample geometries.
a) Complete channel (300×400×5000 µm) filled with pure ethanol. $A_{810°}/A_{90°}$ ratio is 76%. An $A_{810°}/A_{90°}$ ratio of 78% was simulated, see fig. 3.4.
b) A 3.75 mm plug of pure ethanol encapsulated in between two 15 mm long fluorinert plugs in a 4 cm long fused silica capillary (ID 100 µm, OD 200 µm) positioned in the same channel (Fig. 10a) such that the plug was centred on the 5 mm long constriction. The $A_{810°}/A_{90°}$ ratio is 99%. An $A_{810°}/A_{90°}$ ratio of 98% was simulated, see Fig. 3.4b.

Limit of Detection

The Limit of Detection (LOD) and normalized Limit of Detection ($nLOD_m$) of this probe for 1D ^{1}H-NMR were examined by the measurement of pure isopropanol and 600 nMol Sucrose respectively.

A four times averaged pure isopropanol ($3.8 \cdot 10^{19}$ spins in 600 nL) spectrum, shown in Figure 3.11, yielded an LOD of $2.8 \cdot 10^{14}$ spins/√Hz (0.47 nMol/√Hz). The LOD of this chip could be predicted using the numerically determined B_1/i and a calculated R (including tapering and wide zone) as described before.[11] Assuming only copper losses and neglecting the substrate losses an LOD of $3.1 \cdot 10^{13}$ spins/√Hz was predicted for this structure. As no other sources for signal loss are obvious, it must be concluded that the substrate-induced losses decrease the LOD with a factor of 9.

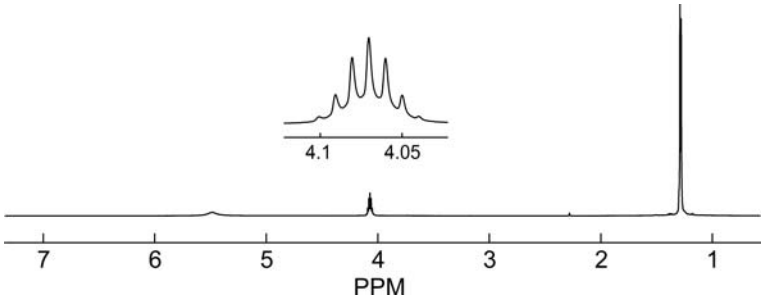

Figure 3.11. 4 times averaged unapodized ^{1}H spectrum of pure isopropanol. The SNR_t was 3839 from which an LOD of $2.8 \cdot 10^{14}$ spins/√Hz (0.47 nMol/√Hz) was calculated. The linewidth (after coarse shimming) is 1.9 Hz, as determined with a Lorentzian fit on the multiplet.

For convenient comparison with other micro-NMR systems, we also measured 600 nMol Sucrose and determined the $nLOD_m$.[22,23] The $nLOD_m$ is defined as the mole quantity necessary to obtain an SNR of 3 for a specified resonance peak in one second. We prefer the LOD of Eq. 2.7 over the $nLOD_m$ because this definition makes comparison of different probes straightforward, since it is independent of the data treatment and sample in contrast to the $nLOD_m$.

Figure 3.12 shows the single scan spectrum of Sucrose obtained after 1.5 seconds water-suppression. The SNR (defined as the height of the peak of interest divided by two times the root-mean-square of the noise) for the anomeric proton was 189. The $nLOD_m$ was calculated to be 22.3 nMol·√s. Since the measurements were performed on a 600 MHz system, scaling was not necessary. To compare this number with the results of Krojanski et al.,[23] who reports an $nLOD_m$ of 0.39 nMol·√s for 10.6 nL, our $nLOD_m$ was scaled to the same volume of 10.6 nL (57 times smaller). Decreasing the

sample volume with a factor of 57 gives a sensitivity increase[13] of $57^{(1/3)}$ yielding an $nLOD_m$ of 5.8 nMol·√s. Again, the lower sensitivity of the chip is explained by the substrate induced losses and the non optimized filling factor.

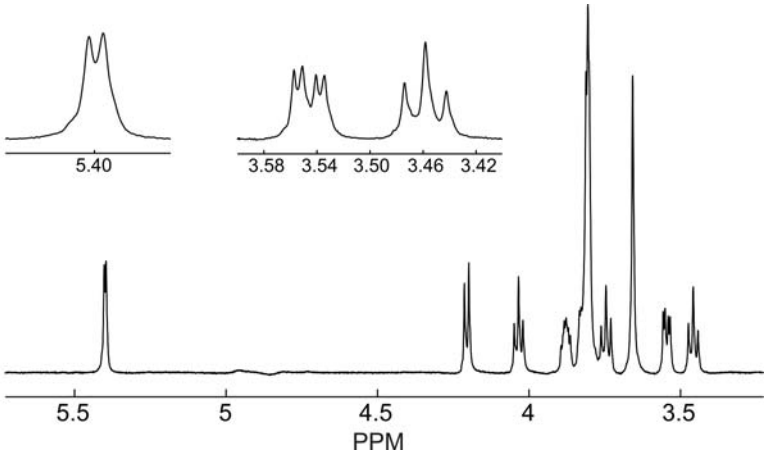

Figure 3.12. Single scan unapodized ^{1}H-spectrum of 600 nMol Sucrose in D_2O. Pulse delay: 3 sec; Water suppression by pre-saturation: 1.5 sec at a power of 1 µW (-16dB); 90° pulse: 3.7 µs at a power of 5 Watt (53 dB); acquisition time: 1 sec; spectral width: 1.5 kHz. Total time per scan: 5.5 sec. The SNR of the anomeric proton doublet was 189. The insets show details of the spectrum which indicate the superior resolution. Small J-couplings of 3.67 Hz are clearly resolved.

Shimming and resolution

From the linewidth broadening simulations discussed above, it was predicted that our design could exhibit a linewidth of ~0.5 Hz. In these simulations, the susceptibility distortions of the probe housing were not taken into account. These distortions, caused by the materials used for the probe were expected to be easily compensated with the standard shim set. However, the applicability of the standard shim set is rather limited for the tiny samples handled on chip, because the chip-induced distortions were concentrated in a very small volume, demanding extreme accurate settings for higher order shims. It was indeed observed that sharp lines (~2 Hz) were easily obtained by coarse settings of Z1, Z2, X and Y shims, as for example shown in Figure 3.11. Figure 3.13 shows the spectrum of pure ethanol after careful shimming with higher order shims. The J-multiplets are resolved to the baseline, and a linewidth of 0.73 Hz (1.2 ppb) is measured, in good agreement with the predictions. To our knowledge, this is the highest resolution, ever achieved on an integrated NMR chip.

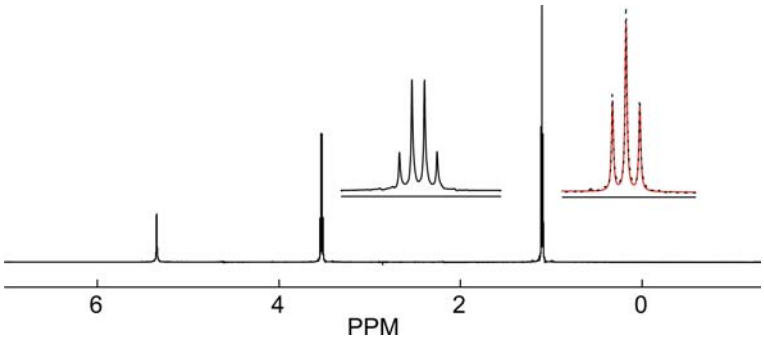

Figure 3.13. NMR spectrum of 600 nL pure ethanol (96% VLSI). The insets show magnifications of the CH_2 and CH_3 group. A Lorentzian fit of the methyl peak (red line) revealed a FWHM of 0.73 Hz. The dots represent the data points, whereas the line shows the fit. Linewidths at different heights: 50 %: 0.73 Hz, 0.55 %: 30.13 Hz, 0.11 %: 93.72 Hz. Measurement conditions: single scan; spectral width 5 kHz; 90° pulse width of 4.5 µs, transmitter frequency 600 MHz; transmitter power 5 W; No apodisation.

rf-strength

Although not of interest for proton NMR, the fact that microcoils can generate extremely high rf-fields has a big potential for spectra of other nuclei whose resonance lines are dispersed over a several megahertz bandwidth. Full excitation of such a spin system needs strong rf-fields. The rf-strength as computed with the nutation data discussed above was 36 kHz at a source power of 5 Watt. This is in very good agreement with a simple model based on Ampere's law to predict the field strength around the strip combined with the experimentally determined Q-factor, giving an rf-strength of 35 kHz. Since the stripline is built on a pure silicon substrate which is an excellent heat conductor, wider bandwidths (associated with higher powers) are readily accessible.[11]

2D spectroscopy

The 2D data acquisition ability of our detector (which relies on a good rf-homogeneity) was demonstrated with homo-nuclear proton Correlation Spectroscopy (^{1}H-^{1}H COSY). For this experiment, a 2M Glucose solution (1.2 µMol) in D_2O was prepared and loaded in the chip. Figure 3.14 shows the 1D and 2D plots as recorded with the stripline chip. All the expected resonance peaks and off-diagonal correlation peaks were clearly distinguishable with minimal phase cycling (4×).

This picture demonstrates that all parameters for high performance 2D NMR are at a proper level, and with that the chip is useful for the elucidation of complex molecules, from which the structure cannot be unravelled with 1D experiments.

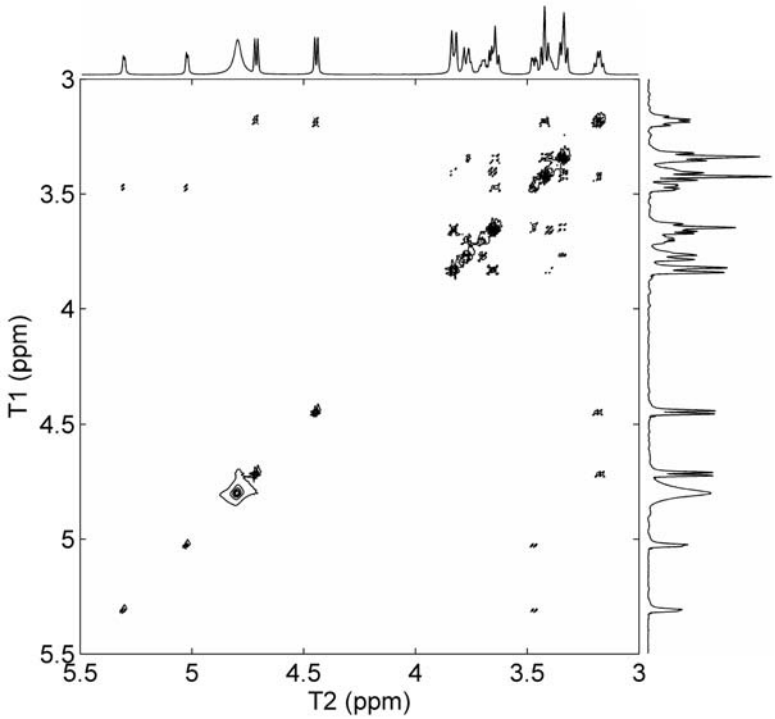

Figure 3.14. Two-dimensional ^{1}H-^{1}H COSY spectrum of a 1.2 µMol ^{13}C-labeled Glucose solution in D_2O, obtained with the stripline probe. 1024 T1 increments with minimal phase cycling of 4 scans were taken. Acquisition time per scan was 2 seconds, and the pulse delay 10 seconds. The total measurement time was 13.6 hr.

Discussion

It was found that the stripline geometry can be modelled in detail and an optimization towards required sensitivity, good B_1-homogeneity and ultimate resolution is possible. Moreover, the experimental results are in excellent agreement which means that optimization for other sample sizes or geometries can be straightforward. The implementation based on two substrates has turned out to be a useful platform for the evaluation of the stripline performance for NMR detection.

The stripline chip was based on a λ/2 resonator. The advantage of a λ/2 geometry is that it is a contactless resonator, preventing loss problems associated with contact resistance. Since the wavelength at 600 MHz is rather long (0.5 m in air and 0.33 m on a low-loss substrate like PTFE), we chose silicon as a substrate for its high ε_r (11.9). Apart from that, silicon yields the possibility to implement extra functionality like (CMOS) pre-amplifiers.

For low-loss substrates we have demonstrated that the predicted sensitivity for striplines very accurately converges with the experimental results, see Chapter 2.[11] Therefore, the comparison of the predicted LOD based on negligible losses in the silicon substrate and the achieved LOD in this work clarifies that the lowering in sensitivity must be attributed to substrate losses. Actually, this is already expected from the moderate Q-factor which could be obtained when implementing the substrate as a dielectric in a low-loss LC-resonator (see section substrate choice and modification). Thus, although the substrate is treated to minimize losses, it turns out that the passivation was not sufficient to obtain an LOD close to the predicted value assuming a low-loss substrate. These considerations explain the substantial difference in LODs between numbers reported in literature and the stripline described in this chapter.

Since sensitivity is essential for NMR, stripline probes designed on other substrates (*e.g.* fused silica implemented as a $\lambda/4$ structure) are worthwhile to be studied further. Apart from that, the filling factor (which was not optimized in the current chip) should be enhanced by fabrication of two channels at both sides of the central line. Such a design is discussed in Chapter 6.

Conclusions

We have modelled and built a stripline-based micro-NMR detector. The optimization of sensitivity, resolution and rf-homogeneity has been discussed. 2D and 3D rf-field simulation results were presented which were used for these optimization steps. Optimal dimensional ratios were found for w/d (1-1.5) and l/w (5-10).

From the experimental results it could be concluded that the simulation results were in good agreement with practice. By means of nutation experiments, an rf-homogeneity of 76% ($A_{810°}/A_{90°}$ ratio) was found for a completely filled channel whereas 78% was predicted. This number is comparable with commercial liquid-state NMR probes, and allowed for high-resolution 2D spectroscopy of ^{13}C-Glucose. Based on NMR lineshape predictions a linewidth of 0.5 Hz was expected, and a linewidth of 0.73 Hz was demonstrated in practice. An rf-strength of 36 kHz was reached for 5 Watt input power. The LOD of $2.8 \cdot 10^{14}$ spins/$\sqrt{\text{Hz}}$ was moderate compared to numbers reported in literature, which can be attributed to losses in the silicon substrate.

References

[1] L.V. Blake, *Transmission Lines and Waveguides*, John Wiley & Sons, Inc., New York (1969).
[2] C. Schöllhorn, W. Zhao, M. Morschbach, E. Kasper, *IEEE Trans. Elec. Dev*. 50(3), 740 (2003).
[3] J. Krupka, J. Breeze, A. Centeno, N. Alford, T. Claussen, and L. Jensen, *IEEE Trans. Microwave Theor. Techn*. 54(11), 3995 (2006).
[4] R.-Y. Yang, C.-Y. Hung, Y.-K. Su, M.-H. Weng, H.-W. Wu, *Microw. Opt. Techn. Letters* 48(9), 1773 (2006).
[5] B. Rong, J.N. Burghartz, L.K. Nanver, B. Rejaei, M. van der Zwan, *IEEE Electr. Dev. Letters* 25(4), 176 (2004).
[6] M. Spirito, F.M. De Paola, L.K. Nanver, E. Valletta, B. Rong, B. Rejaei, L.C.N. de Vreede, J.N. Burghartz, *IEEE Trans. Microwave Theory and Techn.* 53(7), 2340 (2005).
[7] J.T.M. van Beek, M.H.W.M. van Delden, A. van Dijken, P. van Eerd, A.B.M. Jansman, A.L.A.M. Kemmeren, T.G.S.M. Rijks, P.G. Steeneken, J. den Toonder, M.J.E. Ulenaers, A. den Dekker, P. Lok, N. Pulsford, F. van Straten, L. van Teeffelen, J. de Coster, R. Puers, High-Q integrated RF passives and RF-MEMS on silicon, *Proceedings of the Mat. Res. Soc. Symp.* Vol. 783 (2004).
[8] S. Chang, S. Sivoththaman, Low loss inductors built on PECVD intrinsic amorphous silicon for RF integrated circuits, *Proceedings of the 18th Annual Canadian Conference on Electrical and Computer Engineering (CCECE05),* Saskatoon, Canada, May 1-4 (2005).
[9] J.H. Klootwijk, H. van Kranenburg, C. Cobianu, V. Petrescu, P.H. Woerlee, H. Wallinga, An intensive study of LPCVD silicon morphology and texture for non-volatile memory application, *Proceedings of the 25th European Solid State Device Research Conference, ESSDERC'95,* 383 (1995).
[10] http://femm.foster-miller.net/wiki/HomePage, David Meeker, dmeeker@ieee.org.
[11] P.J.M. van Bentum, J.W.G. Janssen, A.P.M. Kentgens, J. Bart, J.G.E. Gardeniers, *J. Magn. Reson.* 189, 104 (2007).
[12] www.cst.com, CST AG, Darmstadt, Germany.
[13] D.I. Hoult, R.E. Richards, *J. Magn. Reson.* 24, 71 (1976).
[14] F.D. Doty, G. Entzminger, Y.A. Yang, *Concepts Magn. Reson.* 10(3), 133 (1998).
[15] D.L. Olson, T.L. Peck, A.G. Webb, R.L. Magin, J.V. Sweedler, *Science* 270 (5244), 1967 (1995).
[16] F. Laermer, A.R. Schlip, Method of Anisotropically Etching Silicon, US Patent Nos. 4.855.017 and 4.784.720, 1991 and German Patent No. 4241045C1 (1990).
[17] The process was modified with respect to the process described by Klootwijk et al., Ref. 9.
[18] M.J. Madou, *Fundamentals of microfabrication*, CRC Press, Boca Raton (FL), USA (2002).
[19] F. Niklaus, G. Stemme, J.-Q. Lu, R.J. Gutmann, *J. Appl. Phys.* 99, 031101 (2006).
[20] J. Bart, R.M. Tiggelaar, M. Yang, S. Schlautmann, H. Zuilhof, J.G.E. Gardeniers, *Lab Chip* accepted, (2009).
[21] J.D. van Beek, *J. Magn. Reson.* 187, 19 (2007).
[22] M.E. Lacey, R. Subramanian, D.L. Olson, A.G. Webb, J.V. Sweedler, *Chem. Rev.* 99, 3133 (1999).
[23] H.G. Krojanski, J. Lambert, Y. Gerikalan, D. Suter, R. Hergenroder, *Anal. Chem.* 80, 8668 (2008).

– Chapter 4 –

Fast reaction-monitoring using in-flow NMR detection

Parts of this chapter have been published as:

J. Bart, A.J. Kolkman, A.J. Oosthoek-de Vries, K. Koch, P.J. Nieuwland, J.W.G. Janssen, P.J.M. van Bentum, K.A.M. Ampt, F.P.J.T. Rutjes, S.S. Wijmenga, J.G.E. Gardeniers, and A.P.M. Kentgens, *J. Am. Chem. Soc.* 131, 5014 (2009).

Introduction

Recent years have shown an increased interest in the use of microreactors (defined here as microfabricated reactors with channels in the range of tens to hundreds of micrometers) for the study of chemical reactions.[1] Advantages are that these microreactors offer improvements in heat exchange, mass transfer and extremely high surface-to-volume ratios in comparison to conventional batch reactors.[2,3,4,5,6] This warrants better control over selectivity and significant suppression of side product formation. Apart from that, potentially dangerous and/or fast reactions such as exothermic reactions or reactions with flammable, explosive, toxic or hazardous chemicals can be performed under relatively safe conditions because of the low volumes which are usually involved.[7]

Since, due to the laminar flow, chemistry behaves extremely reproducible at every point in the fluidic channel in continuous-flow microreactors, such reactors are very well suited for *in-situ* screening and optimization of reaction conditions and kinetics.[8] Due to the small volumes this can be efficiently carried out with minimal amounts of reactants. The obtained knowledge can greatly benefit a variety of pharmaceutical and industrial processes.

A number of different analytical techniques can be employed to investigate kinetic data.[9,10,11,12] In particular spectroscopic tools are useful because, besides quantitative results, they provide chemical information at the molecular level. For structure elucidation, NMR is certainly the preferred spectroscopic method, through the possibilities offered by techniques like COSY, NOESY and more advanced pulsed-NMR procedures.[13]

Several groups have investigated the applicability of micro-NMR for the *in-situ* study of reaction kinetics. Ciobanu et al. studied the formation of stable borate–sugar complexes by monitoring the kinetics of xylose–borate reactions.[14] They introduced two fluid flows (d-xylose and borate solutions) in a Y-shaped mixer. The mixed solutions passed through a capillary around which multiple, physically distinct NMR detector coils were wound, each having a detection volume of 31 nL. The distance between the mixer and each individual NMR coil, together with the flow rate used, determined the reaction-time. The reaction time-window was between 8 s and 66 s corresponding to flow rates ranging from 17.6 μL/min to 5 μL/min. The reason to use multiple microcoils was that the amount of sample required to obtain the data was decreased. On the other hand, this set-up introduces big challenges for the rf-circuitry.

Wensink et al. presented a microfluidic chip containing two inlet channels, a mixer and one outlet channel. A planar microcoil detecting a 56 nL volume was integrated.[15] They demonstrated the real-time monitoring of the imine formation from benzaldehyde and aniline. By changing the liquid flow rate, the reaction times in the chip could be set from 30 minutes down to circa 2 seconds. They showed that the kinetics in a microfluidic chip were a factor of 2 faster compared to a standard 5 mm tube in a regular NMR system, which was attributed to faster mixing on the chip.

A long microfluidic chip which fits in a standard 5 mm sample tube, called Micro Channeled Cell for Synthesis Monitoring (MICCS), was commercialized by Jeol Ltd, Japan. Measurements with this system make use of the standard saddle-coil in a 5 mm probe. The chip contained three inlets and one outlet with distinct Y-shaped mixers, such that 2-step reactions could be performed. The reaction volume was 4.4 µL and the observed volume 7.2 µL. Takahashi et al. measured intermediates which appear during the Grignard reaction of 3-hexene-2-one with CH_3MgBr in tetrahydrofuran (THF).[16] The disadvantage of Grignard reagents is that they readily react with protic solvents (such as water). This experiment showed that the problem associated with water traces normally present under standard laboratory conditions was circumvented by exploiting the closed in-flow property of microreactors.

This chapter describes the use of stripline-based NMR detectors for reaction monitoring. The acetylation of benzyl alcohol using acetyl chloride in the presence of *N*,*N*-diisopropylethylamine (DIPEA) was chosen as a model reaction. The reaction was performed in a separate microreactor which was coupled to the stripline chip.

Experimental section

Set-up and probe

The fluidic part of the set-up was built up according to Figure 4.1. Two gastight syringes (2 × Hamilton 1 mL or 2 × SGE 10 mL) were mounted on two independently controlled syringe pumps (NE-1000, New Era) and connected using FEP tubing (Upchurch Scientific, 1529L, 1/16" OD, 1/100" ID) using luer locks. The tubing was connected to the inlets of the microreactor using flat bottom headless nuts (Upchurch Scientific, M-660 + M-650).

The microreactor (dimensions: 45×15×2.2 mm), having two inlets, one quench inlet (not used) and one outlet, was fabricated in borosilicate glass (BF33, Schott technical glasses, Germany) by Micronit Microfluidics BV, Enschede, The Netherlands. The microreactor (which is shown in Figure 4.1a) contained two semicircular fluidic channels which were fabricated using hydrofluoric (HF) acid

etching and had lengths of 30 and 877 mm respectively (volumes of 142 nL and 4.2 µL respectively). For the work presented here, the 30 mm long channel was used. The microreactor was positioned in a custom-made chip holder[17] with threaded holes on the top side in which the fluidic connectors could be screwed, see Figure 4.1b. This holder was positioned on top of the NMR probe as shown in Figure 4.1b and c. A 200 mm long fused silica capillary (Polymicro, TSP 100375, 360 µm OD, 100 µm ID), connected via nuts and ferrules (Upchurch Scientific, F123H + N-123-03) was used to connect the microreactor to the NMR chip. The total reaction volume from the point where the chemicals were mixed in the microreactor till the detection area in the NMR chip was 4.5 µL.

The fluidic channel (height: 300 µm, width 400 µm, length: 40 mm) in the stripline based NMR chip was anisotropically etched in silicon. The stripline, feeding the rf-current to excite and detect the nuclear spins was defined in copper, having a constriction (the area where the high rf-field is generated) of 5 mm long and 1 mm wide. The detected volume under this constriction was 600 nL. The outlet of the NMR chip was connected (using the same type of capillaries and connectors as were used for the inlet) to a waste vessel.

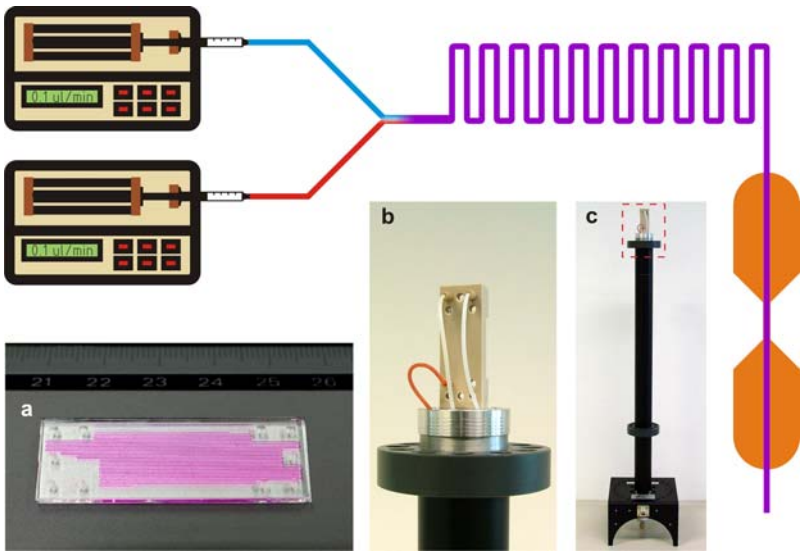

Figure 4.1. Schematics of the fluidic set-up. Two syringe pumps introduce two different substances, which start to react at the joint. The reaction continues until the outlet of the NMR chip.
a. The glass microreactor with purple ink indicating the channel.
b. Close-up view of the microreactor holder mounted on top of the probe
c. The stripline probe. The dashed line indicates the position of the microreactor holder.

Materials

All chemicals were of analytical grade and used as received. Acetyl chloride, benzyl alcohol, *N,N*-diisopropylethylamine (DIPEA) and deuterated chloroform were purchased from Sigma-Aldrich.

DIPEA and benzyl alcohol were dissolved together in deuterated chloroform, both in concentrations of 0.5 M. The concentration of the acetyl chloride was 1.2 M, also in deuterated chloroform.

NMR experiments

NMR spectra were continuously recorded during experiments at different flow rates. After having set a new flow rate, a stabilization time depending on the flow rate (varying from 5 minutes for the high flow rates to 45 minutes for the low flow rates) was taken into account, and a representative spectrum was recorded and saved.

The reference ^{1}H-NMR spectra were acquired on a Bruker AMX-400 in a 5 mm tube. The ^{1}H-NMR experiments in the stripline probe were carried out on a Chemagnetics CMX-Infinity 600 solid-state NMR spectrometer (600 MHz) using Spinsight software. All spectra were recorded at 300K and processed by using the MatNMR processing package.[18]

Flow Effects

Operating NMR under flow conditions has an effect on the observed effective spin-lattice relaxation time-constant T_1^{obs} and the observed spin-spin relaxation time constant T_2^{obs} (usually called T_2^*). This is expressed in the following equations:

$$\frac{1}{T_1^{obs}} = \frac{1}{T_1^{stat}} + \frac{1}{\tau} \qquad 4.1$$

$$\frac{1}{T_2^{*}} = \frac{1}{T_2^{stat}} + \frac{1}{\tau} \qquad 4.2$$

where τ is the residence time of a particular spin in the observed volume. Both time constants are shortened when operating in flow, because excited spins in the detection area are replaced by spins in thermal equilibrium. In terms of SNR, this is advantageous since pulse repetition can be increased for spins with long T_1 relaxation times, resulting in an improved SNR per unit time.[19,20] On the other hand, a shortened spin residence time will increase signal linewidth for any spin which can not be observed for a period long enough to record a full FID decaying with relaxation time constant T_2. In other words, when the observe volume of the NMR

probe is small with respect to the flow, the Free Induction Decay (FID) of the spins cannot be fully recorded. The resulting increase in linewidth due to flow is inversely proportional to the residence time: $LW=1/(\pi \cdot T_2^*)$.[21] Since the flow-dependent Equation 4.2 is an approximation, the flow-induced line broadening of the stripline was also studied by a numerical simulation in Matlab (Mathworks), in which the rf-pattern along the channel after a 90° pulse (obtained from CST 3D simulations, see Chapter 3, Figure 3.2b) was used. Basically, the fluidic channel was divided in small cross-sectional slices, which were excited according to the rf-pattern. At zero-flow conditions, the FID of every slice should have the shape of Figure 4.2a, scaled with respect to its position in the rf-pattern.

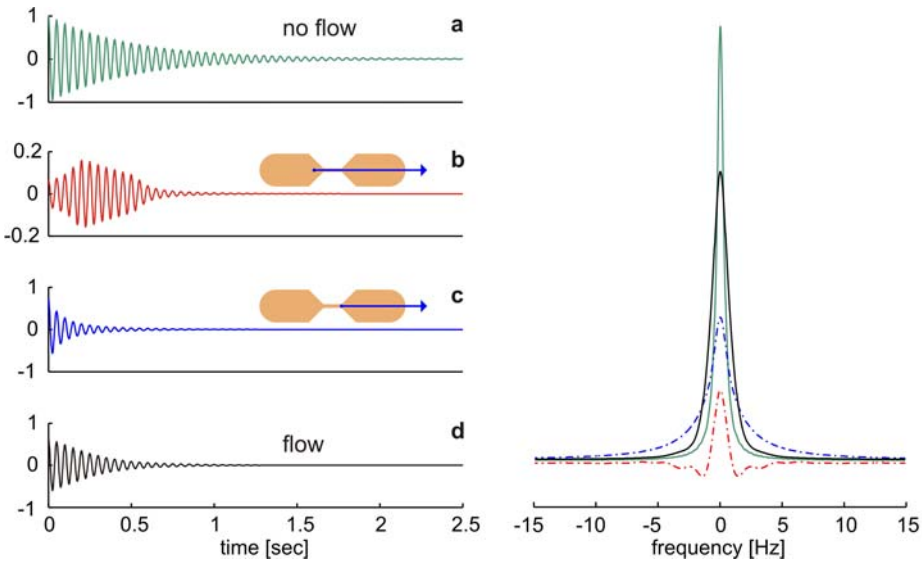

Figure 4.2. Flow effect on FID's belonging to individual precessing spins. T_2=0.5 sec. Flow rate is 100 µL/min except for Fig. 4.2a (no flow).
a) No flow. FID belonging to slice in center of constriction.
b) FID for a slice that is excited just before entering the constriction. The amplitude of the FID is enhanced during the first 0.25 seconds by entering via the tapering area into the most sensitive part of the stripline. The region from 0.25 to 0.6 seconds has precessed in the constricted area. After that, the FID decays more rapidly than T_2 because the sensitivity decreases simultaneously. Note that the initial amplitude is lower, because the spins are weakly excited.
c) FID for a slice that departs the constriction area shortly after excitation. The FID decays more rapidly than T_2. Note that the initial amplitude is nearly maximal since excitation took place in the constriction area.
d) Sum of the FID's of all segments along the channel.
picture on the right) Fourier transformed FID's, showing non-Lorentzian characteristics for FID's simulated in flow. The colours are adapted to the FID's in Figure 4.2a through d.

When the system is operated in flow, the rf-excitation (which is on such a short timescale that it can be assumed to be instant) will be according to the pattern of Figure 3.2b. However, the detection of the magnetizations along the channel (which takes place in the time range of seconds) will be position-dependent. In order to visualise the effect of flow on the FID belonging to one sample slice in the channel, each FID data point was calculated taking the travelled distance of the precessing spin into account. The Figures 4.2b and c show two simulated FID's belonging to sample slices travelling with a speed corresponding to a flow rate of 100 µL/min. These pictures indicate the effect of flow on the response of individual spins after a pulse. The final FID along the whole channel was obtained by summing the contributions of the individual slices (Fig. 4.2d). Figure 4.2 (right picture) displays the lineshapes after Fourier transformation of the four displayed FID's. Clearly, the lines belonging to the FID's depicted in Figure 4.2b and c have a non-Lorentzian shape, caused by a non-exponential decay of the FID. Therefore, the final FID (black) also shows a non-Lorentzian shape, and is increased in width.

The graph in Figure 4.3 shows the line broadening as a function of flow. The difference between the analytical and numerical solutions is because the analytical expression (Eq. 4.2) assumes a pure exponential decay of the detection-sensitivity along the flow direction. These results show that, although the NMR signal linewidth will increase as a function of flow, it can accurately be predicted.

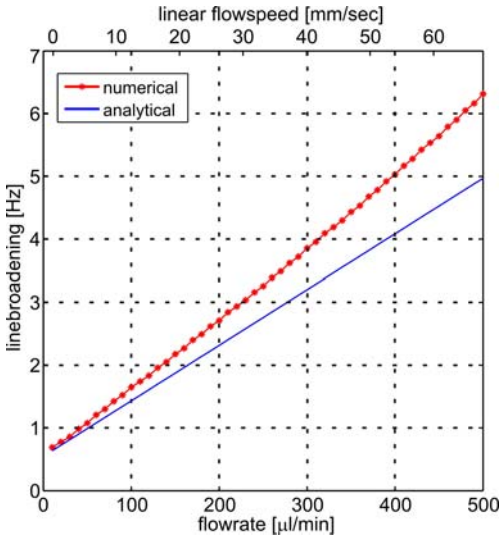

Figure 4.3. Line broadening as a function of the flow rate (bottom x-axis) or linear flow speed (top x-axis). For the numerical simulation a T_2^{stat} of 0.5 seconds was taken, which returns a linewidth of 0.7 Hz in static conditions. The blue line represents the analytical expression from Eq. 4.2.

Typical flow rates in microreactors are usually in the microliter range and seldom exceed 150 μL/min. From Figure 4.2 it can be concluded that such flow rates will never give rise to serious blurring of the NMR spectra. The intrinsic high resolution of the stripline chip still permits a spectral resolution of better than 2.2 Hz for flow rates up to 150 μL/min (corresponding to a linear flow speed of 20 mm/sec) can be predicted for every flow rate. Therefore observed line broadenings can be interpreted as meaningful information about the sample under study.

Results and discussion

Maintained resolution under flow conditions

Initially, we aimed for the carbamate formation from toluene diisocyanate (TDI) and pure ethanol as a model reaction. However, because of channel clogging caused by sedimentation of the product, this reaction could not be performed properly in the microreactor. Nevertheless, in the first stage of the reaction (when minimal product was formed) the reaction was running properly and representative spectra could be obtained. From these initial experiments, it was concluded that the resolution is indeed maintained at higher flow rates, as theoretically defended above. Figure 4.4 displays a spectrum recorded at a flow rate of 25 μL/min during the carbamate formation from toluene diisocyanate (TDI) (0.5 M in toluene) and pure ethanol. All J-couplings were clearly resolved, such that all typical reactant and product multiplets could be identified. This means that line broadening (exceeding the numbers given in Figure 4.3) observed during reaction monitoring should not be addressed to flow effects but to chemical phenomena.

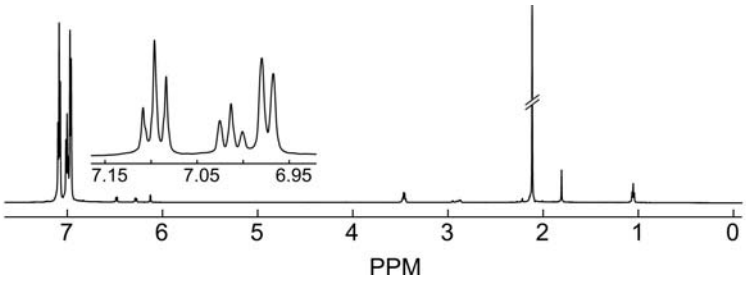

Figure 4.4. Spectrum recorded during carbamate formation at flow rates of 24.46 and 0.54 μL/min for TDI and ethanol, respectively. Only resonances of solvents and reactants are visible because of the short reaction time (9 sec) and the low TDI concentration. Inset: toluene aromatic peaks with all the J-couplings resolved, indicating the high-resolution performance. The stopped-flow linewidth was not shimmed down to the optimal resolution (0.7 Hz) but approximately to 2.8 Hz. The lines in this spectrum show also a linewidth of 2.8 Hz.

Acetylation of benzyl alcohol

Acetylation is a reaction that introduces an acetyl functional group into an organic compound. Such reactions play an important role in biological processes,[22] and are among the most frequently used reactions in organic synthesis,[23] where they are typically performed in the presence of a basic catalyst.[24] The most famous acetylation reaction is the synthesis of aspirin.[25]

Figure 4.5 shows the reaction scheme of the acetylation of benzyl alcohol using acetyl chloride. DIPEA was used as a basic catalyst.

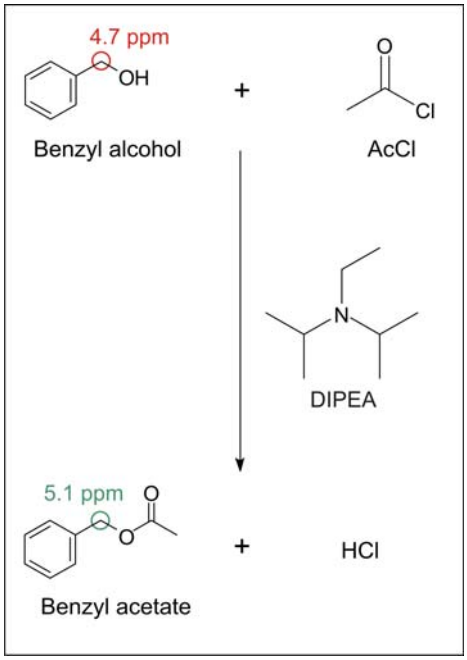

Figure 4.5. Schematic of the acetylation of benzyl alcohol using acetyl chloride in the presence of DIPEA. The conversion is calculated from the relative intensities of the α-protons (benzyl alchohol at 4.7 ppm and benzyl acetate at 5.1 ppm).

The main goal was to analyse the conversion as a function of time in the microfluidic set-up and find the optimal conversion parameters. The relative intensity of the α-protons belonging either to the benzyl alcohol or the benzyl acetate was used to calculate the conversion:

$$conversion = \frac{area_{benzylacetate}}{area_{benzylalcohol+benylacetate}} \qquad 4.3$$

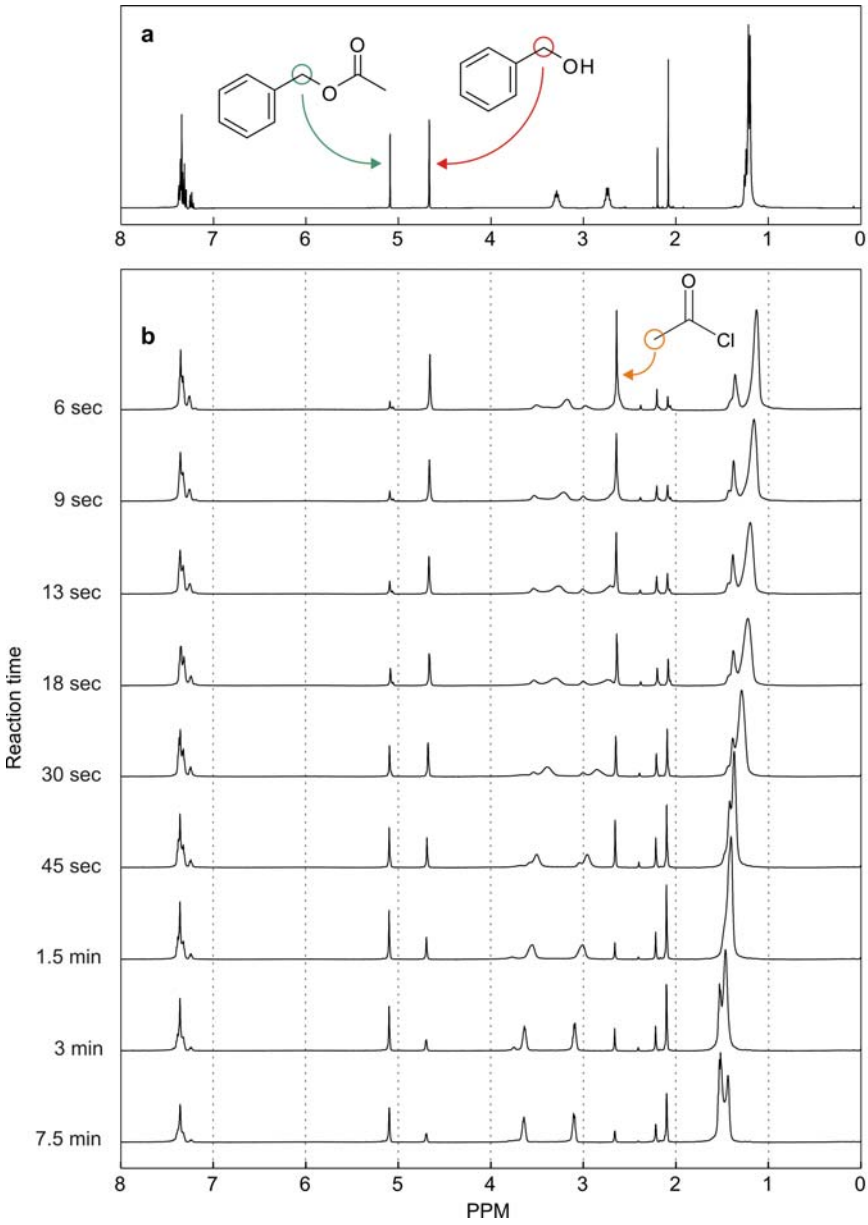

Figure 4.6. a) Reference spectrum of the acetylation of benzyl alcohol (excess) with acetyl chloride in the presence of DIPEA. The spectrum is recorded in a regular NMR system, 5 minutes after the initiation of the reaction. Stoichiometry: benzyl alcohol/DIPEA/acetyl chloride: 2:2:1.
b) Reaction monitoring of the acetylation of benzyl alcohol with acetyl chloride in the presence of DIPEA. The spectra are recorded in the stripline probe with different flowrates (from 0.6 to 45 µL/min) corresponding to different reaction times (from 7.5 min to 6 sec). The stoichiometry is kept constant at 1:1:1.2.

Figure 4.6a shows the spectrum of the acetylation reaction, as measured in a regular 400 MHz NMR after approximately 5 minutes reaction time. The α-proton of benzyl alcohol was found at 4.7 ppm. After conversion into the benzyl acetate product the α-proton peak was shifted to 5.1 ppm.

Figure 4.6b shows spectra recorded during the same reaction, but performed in the microreactor and measured in the stripline with constant stoichiometry and varying reaction times. Clearly, the conversion is taking place, since the intensity of the benzyl acetate α-proton increases and the acetyl chloride peak (2.69 ppm) as well as the resonance of the α-proton of benzyl alcohol are correspondingly diminishing.

Using Eq. 4.3, the conversion was calculated from the spectra in Figure 4.6b. The result for varying reaction time is shown in Figure 4.7. The maximum conversion was found to be 72%.

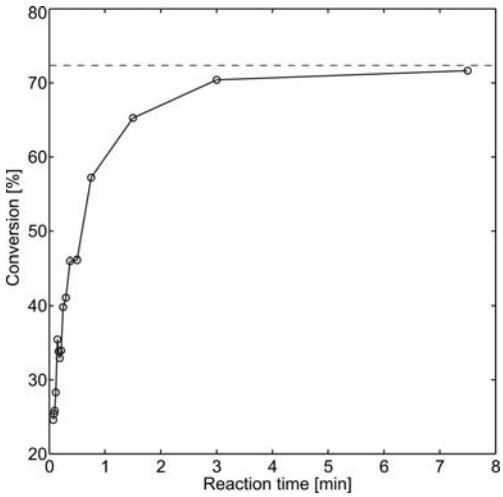

Figure 4.7. Reaction conversion as a function of time. The conversion is calculated according to Eq. 4.3. A maximum conversion of 72% is reached.

Intermediates and side-product formation

The fact that 100% conversion was not reached is explained by the formation of side- products. Besides the main product (benzyl acetate), at least two side-products were formed which could be identified as acetic acid and acetic anhydride, which are formed when water is present in the reaction mixture, as shown in Figure 4.8. The peak of the methyl group of acetic acid was found at 2.08 ppm and the acetic anhydride resonance was found at 2.23 ppm.

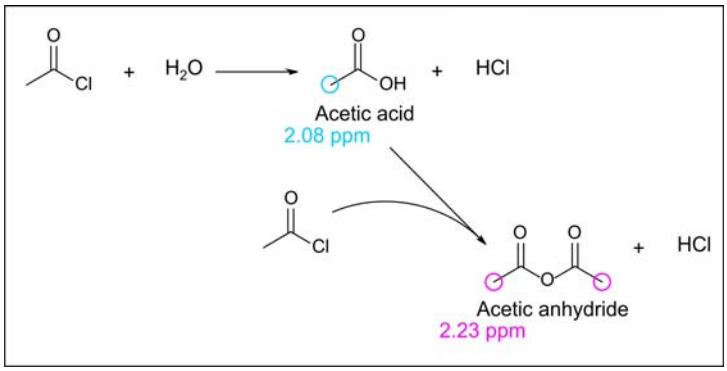

Figure 4.8. Side-reactions taking place during the acetylation of benzyl alcohol. Acetyl chloride reacts with water forming acetic acid, and acetic acid can react further into acetic anhydride.

A comparison of the reference spectrum with the dynamic data recorded in the stripline revealed two striking differences. First, broadening and shifting of the DIPEA peaks was observed in the dynamic data, most pronounced at the beginning of the reaction, and going back to a natural linewidth as the reaction progresses. This line broadening must be addressed to a chemical phenomenon since the flow analysis discussed above predicts a maximal line broadening of 1 Hz at these flow rates (up to 50 µL/min). This also agrees with other resonances which indeed exhibit narrow lines (*e.g.* at a chemical shift position around 5 ppm). The DIPEA line broadening is supposed to be caused by fast proton exchange of DIPEA occurring within the timescale at which the FID is recorded. Since the reference spectrum was recorded after a substantial reaction time, such fast kinetics were not taking place anymore. The chemical shifts for non-protonated DIPEA could be found in the first spectrum, which was recorded directly after initiation of the reaction: 1.13 ppm, 2.6 ppm and 3.18 ppm, respectively. The peaks for protonated DIPEA were deduced from the last spectrum (after a long reaction time) on 1.5 ppm, 3.1 ppm and 3.65 ppm, respectively.

The second difference was a clearly observable peak at 2.41 ppm in the kinetic data, which was almost unobservable in the regular spectrum. Preliminary results, based on a separate reaction between DIPEA and acetyl chloride (without benzyl alcohol), suggest that this resonance can be addressed to a short-lived intermediate DIPEA-acetate complex, which is formed by the reaction between DIPEA and ketene. Intentionally, DIPEA was added for scavenging protons from the acetyl chloride, thus forming ketene. The ketene, which is very instable, should react with benzyl alcohol, forming benzyl acetate. Practically, this is indeed the main reaction path, however, DIPEA can also react with ketene, forming a DIPEA-acetate complex. An in-

depth study of these observations is beyond the topic of this thesis. Nevertheless, this comparison shows that in-flow NMR can provide information beyond what can be obtained with standard NMR equipment.

Conclusions

In-flow NMR detectors offer the possibility to obtain kinetic data of chemical reactions on time scales inaccessible by regular NMR. In this chapter, a microfluidic set-up is demonstrated, consisting of a microreactor directly coupled to the stripline detector. Since operating NMR under flow conditions is not trivial, flow-effects on the linewidth are discussed, and a prediction of the line broadening as a function of the flow rate was presented. From this analysis it was concluded that only minor line broadening effects are expected at high flow rates.

The real-time monitoring of the acetylation of benzyl alcohol with acetyl chloride in the presence of DIPEA was demonstrated. These experiments allowed for visualisation of short-term line broadening caused by (de-)protonation of DIPEA which could not be observed in reference spectra obtained in a regular NMR system. Furthermore, the microreactor experiments showed a resonance at 2.41 ppm, which was almost unobservable in the experiments performed in a 5 mm NMR tube. This peak was supposed to be a short-lived DIPEA-acetate complex resonance. These results demonstrated the possibility to track intermediates using fast *in-situ* analysis.

Although in this study the variations of the flow rates as well as the successive recording of NMR spectra were set manually, the complete measurement procedure can easily be automated, yielding a tool which allows for very fast reaction screening and optimization.

References

[1] P. Watts, C. Wiles, *Chem. Commun.* 5, 443 (2007).
[2] G.N. Doku, W. Verboom, D.N. Reinhoudt, A. van den Berg, *Tetrahedron* 61(11), 2733 (2005).
[3] K. Geyer, J.D.C. Codee, P.H. Seeberger, *Chem. Eur. J.* 12(33), 8434 (2006).
[4] V. Hessel, H. Löwe, *Chem. Eng. Tech.* 28(3), 267 (2005).
[5] J. Yoshida, A. Nagaki, T. Iwasaki, S. Suga, *Chem. Eng. Tech.* 28(3), 259 (2005).

[6] J. Kobayashi, Y. Mori, K. Okamoto, R. Akiyama, M. Ueno, T. Kitamori, S. Kobayashi, *Science* 304, 1305 (2004).
[7] R.M. Tiggelaar, F. Benito-López, D.C. Hermes, H. Rathgen, R.J.M. Egberink, F.G. Mugele, D.N. Reinhoudt, A. van den Berg, W. Verboom, J.G.E. Gardeniers, *Chem. Eng. J.* 131, 163 (2007).
[8] K. Koch, R.J.F. van den Berg, P.J. Nieuwland, R. Wijtmans, H.E. Schoemaker, J.C.M. van Hest, F.P.J.T. Rutjes, *Biotechn. Bioeng.* 99, 4 (2008).
[9] X.S. Chai, Q. Luo, J.Y. Zhu, *J. Chromatogr. A* 946, 177 (2002).
[10] A. Liesener, U. Karst, *Anal. Bioanal. Chem.* 382, 1451 (2005).
[11] K.P. Nichols, S. Azoz, J.G.E. Gardeniers, *Anal. Chem.* 80, 8314 (2008).
[12] M. Kakuta, D.A. Jayawickrama, A.M. Wolters, A. Manz, J.V. Sweedler, *Anal. Chem.* 75, 956 (2003).
[13] R.R. Ernst, G. Bodenhausen, A. Wokaun, *Principles of nuclear magnetic resonance in one and two dimensions*, Clarendon Press, Oxford (1987).
[14] L. Ciobanu, D.A. Jayawickrama, X. Zhang, A.G. Webb, J.V. Sweedler, *Angew. Chem. Int. Ed. Engl.* 42, 4669 (2003).
[15] H. Wensink, F. Benito-Lopez, D.C. Hermes, W. Verboom, J.G.E. Gardeniers, D.N. Reinhoudt, A. Van Den Berg, *Lab Chip* 5, 280 (2005).
[16] Y. Takahashi, M. Nakakoshi, S. Sakurai, Y. Akiyawa, H. Suematsu, H. Utsumi, T. Kitamori, *Anal. Sci.* 23, 395 (2007).
[17] H.K. Trieu, J. Slotkowski, R. Klieber, J.C.M. van Hest, K. Koch, K., F.P.J.T. Rutjes, P.J. Nieuwland, P. Wiebe, Chip holder, fluidic system and chip holder system, Patent PCT/EP/2006/010299, 2006.
[18] J.D. van Beek, *J. Magn. Reson.* 187, 19 (2007).
[19] D.A. Laude, C.L. Wilkins, *Anal. Chem.* 56, 2471 (1984).
[20] H.C. Dorn, *Anal. Chem.* 56 (6), 747A (1984).
[21] M.H. Levitt, *Spin dynamics. Basics of Nuclear Magnetic Resonance*, John Wiley & Sons, Ltd, Chichester (2001).
[22] C.A. Hazzalin, L.C. Mahadevan, *PLoS Biology* 3, 12, 2111 (2005).
[23] T.W. Green, P.G. Wuts, *Protective Groups in Organic Synthesis*, 3rd ed., Wiley, New York (1999).
[24] S.-G. Lee, J.H. Park, *J. Mol. Cat. A: Chemical* 194, 1-2, 49 (2003).
[25] C. Gerhardt, *Annalen der Chemie und Pharmacie* 87, 149 (1853).

– Chapter 5 –

Micro-NMR spectroscopy on low concentration bodyfluids

Parts of this chapter have been published as:

J. Bart, A.J. Kolkman, A.J. Oosthoek-de Vries, K. Koch, P.J. Nieuwland, J.W.G. Janssen, P.J.M. van Bentum, K.A.M. Ampt, F.P.J.T. Rutjes, S.S. Wijmenga, J.G.E. Gardeniers, and A.P.M. Kentgens, *J. Am. Chem. Soc.* 131, 5014 (2009).

Introduction

Understanding the biochemical processes that occur in cells has captured the attention of scientists for over a century. A large part of this attention is focussed on metabolomics, which is the 'systematic study of the unique chemical fingerprints that specific cellular processes leave behind'.[1] In metabolomics the usually small molecules (metabolites) involved in biochemical processes are studied by a variety of techniques. NMR spectroscopy has emerged as a key tool for understanding metabolic processes in living systems.[2,3] The advantage of the NMR analysis compared to other analysis techniques (HPLC, GC, CE and MS) is that it provides specific structure information, needs minimal preparation and is a quantitative technique. Furthermore, NMR can selectively screen certain processes, *e.g.* by performing ^{31}P-NMR to study ATP/ADP ratios and energy balances.[4]

Because of its inherent low sensitivity, relatively large sample amounts (containing at least 10^{16} nuclear spins which translates tens of milligrams of sample) are necessary for proper spectroscopy in an acceptable time window. This severely limits the applicability of NMR for mass-limited low concentration samples, *e.g.* metabolites of small animals and plants, which are only collectable in microliter quantities.

Besides spectroscopic problems, micro- or nanoliter sample handling and preparation becomes difficult in a standard NMR set-up, which, in combination with possible hyphenation of analysis methods, is one of the most challenging aspects.[5] Such samples are ideally handled in microfluidic systems, as they are available nowadays at an integration level similar to microelectronic circuits.[6] Both the NMR detection sensitivity as well as the sample handling can be improved significantly by the use of integrated microcoils on microfluidic devices.

The microfabricated probe, described in Chapter 3 has demonstrated its usefulness for the acquisition of high-resolution NMR spectra. Therefore, we have tested the microfluidic stripline resonator to establish its suitability for metabolomics studies by measuring human cerebrospinal fluid (CSF). NMR analysis of CSF is a standardized technique, and the corresponding spectra provide unique information, which cannot be obtained by NMR spectroscopy on other body fluids, such as urine or blood.[7] The composition of CSF, which surrounds the spine and brain, reflects the cytological and biochemical basis of central nervous system diseases, inborn metabolic errors, and metabolism of different diseases.

In this chapter, we show that this new design is indeed suitable to resolve complicated spectra of low concentration samples. We describe the NMR

spectroscopy on human CSF in a fully integrated microfluidic NMR chip with a volume of 600 nL.

Experimental section

Sample preparation

CSF samples were provided by the Dutch 'Top Institute Pharma', project D4-102. The CSF samples were collected by lumbar puncture and immediately frozen to -80°C. Before analysis, 500 µL CSF was centrifuged at 650g for 5 minutes to remove cells. To 400 µL supernatant 44.3 µL D_2O and 5.7 µL 40.4 mM 3-(trimethylsilyl)-2,2-3,3-tetradeuteropropionic acid (TSP-d4) in D_2O was added for locking and chemical-shift referencing. The final concentration of TSP-d4 in the CSF was 0.513mM. After obtaining the reference spectrum, the sample was concentrated 9 times in D_2O. Subsequently, 5 µL was injected into the chip by syringe injection through a capillary from which 600 nL was detected.

NMR experiments

A silicon based stripline chip, as described in Chapter 3 was used for all the described measurements. A Q-factor of 35 was measured.

The 1D ^{1}H-NMR reference spectra were acquired on a Bruker AMX-500 NMR spectrometer (500 MHz). Equal processing parameters were applied for both data: 0.3 Hz line broadening and baseline correction. The 1D ^{1}H-NMR experiments on the stripline probe were carried out on a Chemagnetics CMX-Infinity 600 solid-state NMR spectrometer (600 MHz) operated by Spinsight software. All spectra were recorded at 300K and processed by using the MatNMR processing package.[8]

Since a lock-channel was not implemented in the stripline probe, spectra were recorded in blocks of 128 scans which afterwards were summed. For this summing, the different blocks were shifted with respect to one resonance line (TSP) to frequency-align all spectra, thus correcting for drift of the B_0-field.

Results and discussions

Spectra comparison

Figure 5.1 shows the CSF spectra as measured in a conventional 5 mm probe (reference) and in the stripline chip. The stripline chip contained 1.2% of the metabolites available in the reference sample. As can be noticed directly, the spectra are highly comparable. For both 1D-spectra, all the main metabolite resonances in

the aliphatic region could be identified successfully. The region containing the glucose resonances was left out of consideration, due to the naturally occurring overlap. Small changes in chemical shifts between the spectra were observed which is attributed to pH differences.[9] Furthermore, the stripline spectrum has slightly broader lines, which is caused by the absence of a lock-channel in the probe. Although spectrum-alignment was used to correct for line broadening induced by B_0-drift, the drift which had occurred within the recording of one block remains so that the intrinsic resolution which can be achieved in a single shot was not reached. This shows that, especially in the case of low concentration samples where long averaging is necessary, a lock-channel is crucial.

The lowest peak which could be identified was that of Alanine (1.45 ppm). The concentration of this metabolite in the stripline probe was 1.21 mM, which corresponds to 0.7 nmol in 600 nL.

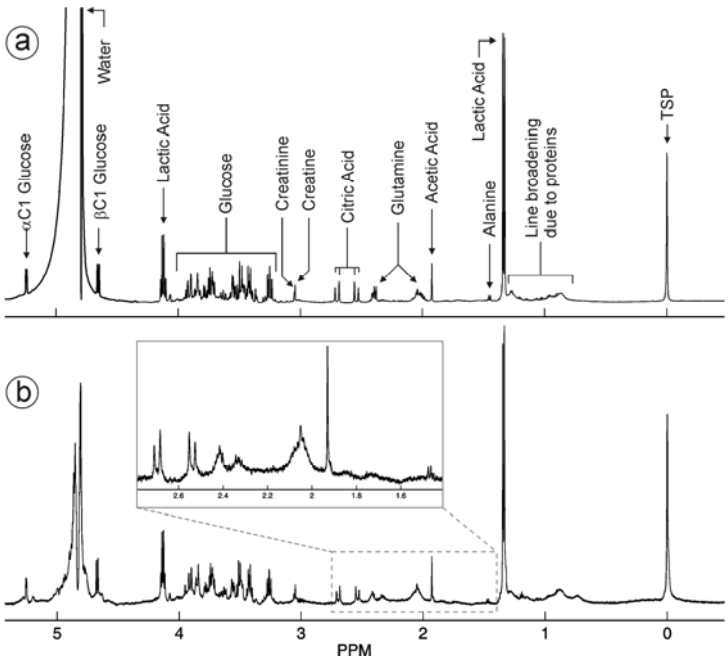

Figure 5.1. NMR spectra of human CSF as recorded in (a) a 5 mm probe and (b) the microchip, which contained 450 µL and 600 nL, respectively. Conditions 5 mm probe: 256 scans; spectral width 10 kHz; acquisition time 5 sec; delay time 12 sec; 90° PW of 6 µs; transmitter power 24W; pH 9.89; presaturation 12 seconds at 0.00015 % of 90° pulse power; zerofilling factor 2. Conditions microchip probe: 4608 scans (36x128 scans, unlocked); spectral width 8 kHz; acquisition time 2 sec; delay time 12 sec; 90° PW of 7 µs; transmitter power 5W; pH 9.41; presaturation 2 seconds at 0.13% of 90° pulse power; zerofilling factor 2.

Sensitivity

The sensitivity enhancement of the stripline probe compared to the 5 mm probe was computed using the experimental parameters and results summarized in Table 5.1. Since the detected sample volume is 500 times smaller, and the initial sample is 9 times concentrated, there are 55.5 times less spins present in the stripline probe. From this it can concluded that the sensitivity is enhanced by a factor of 4.9. Taking the different field strengths into account, (factor $(600/500)^{7/4}$), the final enhancement is 3.6. This means that for the same amount of metabolites, we can decrease the acquisition time in the stripline chip by a factor of $3.6^2 \approx 13$ compared to a 5 mm probe system. The achieved sensitivity enhancement is comparable to the improvement realized by cooling the detection coil and pre-amplifiers in so-called cryoprobes.

	5 mm tube	Stripline
Detected volume	450 µL	600 nL
Number of scans	256	4608
Field strength B_0	500 MHz	600 MHz
Concentration	1	9
SNR of Lactate (1.33ppm)	1175	200

Table 5.1. Experimental parameters and results for the comparison of CSF measurement as performed in a regular 5 mm tube and the stripline probe.

Compared to other microcoil-based NMR probes, this enhancement is quite moderate. Because of the relatively large rf-dissipation in the silicon substrate material (see discussion in Chapter 3), the current stripline probe operates below the theoretical limit. Moreover, our set-up was designed conservatively in terms of stripline dimensions in relation to the sample volume.

The use of low-loss substrates and optimization of the filling factor should make it possible to improve the sensitivity by a factor of 30. Such an optimized stripline is able to measure sub-nmol quantities in a few minutes, which makes it applicable for fast measurements of sample amounts in the picomole regime.

Outlook: mass-limited sample studies

Since the metabolite concentrations in human CSF are comparable to animal CSF, the presented measurements are relevant for animal studies as well. The obtainable CSF sample volumes for mice[10] and rats[11] are 7 and 40 µL *ante-mortem* and 15 and 260

µL *post-mortem*, respectively. Considering 7 µL mouse CSF as a reference, one can dissolve it in a standard 5 mm NMR tube containing about 500 µL D_2O. At this dilution factor, about two weeks of averaging is needed to obtain a similar SNR as for the human CSF presented above, or about one day in a cryoprobe. On the other hand, in the stripline probe the sample can be concentrated into circa 600 nL. In this case a typical measurement time of a few minutes in a fully optimized stripline design is anticipated.

Theoretically one could reduce the sample volume to a few nanoliter (and likewise the dimensions of the stripline) to achieve an even higher sensitivity. With the present lithographic methods this is technologically feasible, but in the end, the solubility of the metabolites will become the limiting factor.

NMR chip technology is attractive to analyze small sample quantities, not only because of the increased sensitivity and uncompromised resolution, but also because of the dedicated sample handling which is possible on these devices. Using the microfabrication toolbox available nowadays, it is no longer visionary to think about a completely integrated platform in one chip which can handle and detect raw samples without any preparative laboratory work. For example, cells and proteins can be separated from the sample by means of an integrated filter, whereas membranes can be used for 'on-chip' concentrating of the sample (see Chapter 7). Furthermore, plug-flow can be utilized to drive the small sample to the sensitive area of the probe. Apart from the study of body fluids, there are other applications; of considerable interest for liquid-state NMR is the hyphenation with other analysis and separation techniques such as liquid chromatography and capillary electrophoresis.[5] The results presented here demonstrate that the NMR resolution and sensitivity is adequate to achieve these goals.

Conclusions

With the stripline probe we have shown that it is possible to design a micro-NMR set-up which satisfies both the need for high sensitivity and high resolution. We have demonstrated a fully integrated NMR chip which can handle micromolar concentrations in nanoliter sample volumes. We have compared spectroscopic results obtained with a standard NMR set-up and with our stripline probe. The sensitivity is 3.6 times higher than compared to standard NMR set-up. With this probe we have carried out spectroscopy on human CSF which has proven the concept, and is very promising for NMR on mouse and rat CSF.

References

[1] C. Beecher, *The Human Metabolome in Metabolic Profiling: Its Role in Biomarker Discovery and Gene Function Analysis*, eds. G. Harrigan & R. Goodacre, Kluwer Academic Publishers (Boston), pp. 311-319 (2003).
[2] F.F. Brown, I.D. Campbell, P.W. Kuchel, D.L. Rabenstein, *FEBS Lett.* 82, 12 (1977).
[3] J.L. Griffin, *Philos. Trans. R. Soc. B* 361, 147 (2006).
[4] M.R. Viant, C.A. Pincetich, D.E. Hinton, R.S. Tjeerdema, *Aquat. Toxicol.* 76, 329 (2006).
[5] V. Exarchou, M. Krucker, T.A. van Beek, J. Vervoort, I.P. Gerothanassis, K. Albert, *Magn. Reson. Chem.* 43, 681 (2005).
[6] T. Thorsen, S.J. Maerkl, S.R. Quake, *Science* 298, 580 (20020.
[7] N.I. Wolf, A.A.P. Willemsen, U.F. Engelke, M.S. van der Knaap, P.J.W. Pouwels, I. Harting, J. Zschocke, E.A. Sistermans, D. Rating, R.A. Wevers, *Neurology* 62, 1503 (2004).
[8] J.D. van Beek, *J. Magn. Reson.* 187, 19 (2007).
[9] W. Lehnert, D. Hunkler, *Eur. J. Pediatr.* 145, 260 (1986).
[10] J.O. Fleming, J.Y.P. Ting, S.A. Stohlman, L.P. Weiner, *J. Neuroimm.* 4, 129 (1983).
[11] M.P. van den Berg, S.G. Romeijn, J.C. Verhoef, F.W.H.M. Merkus, *J. Neurosci. Methods*, 116, 99 (2002).

– Chapter 6 –

Towards optimized glass-based stripline detectors

Introduction

The silicon chip described and applied in the three previous chapters has been established for adequate high-resolution spectroscopy on nanoliter samples. As was mentioned in Chapter 3, the chip was not optimized in terms of sensitivity, however. Especially, an increase of the filling factor by fabricating channels at both sides of the central line is a straightforward way to enhance the sensitivity. Apart from the design, the sensitivity is negatively influenced by dielectric losses in the silicon substrate.

This chapter describes the design of a stripline based detector which has approximately the same observed volume as the silicon chip (600 nL) and is aimed to be optimized in terms of filling factor and losses. The chip design optimization and fabrication will be described, followed by an assessment of the NMR performance of the chip.

Design considerations

Optimized filling factor

In Chapter 3 the optimization in terms of stripline geometry was discussed and optimal dimensional ratios were extracted from the calculations. It was found that the optimal sensitivity is reached for an l/w ratio of 5 (length of the constriction divided by the width of the constriction) and a w/d ratio of 1 (width of the constriction divided by the distance of the ground planes). These ratios were calculated for a chip containing two channels (see Fig. 6.1) each having a width of 2/3 × the width of the constriction w and a height of 1/3 × the distance between the ground planes d (resulting in a total sample cross-section of $2/3w \times 2/3d$). The factor 2/3 was chosen for two reasons: first, the practical limit for etching in a substrate is roughly 2/3 of the total substrate thickness. Although deeper etching is in principle possible, it will give rise to an unacceptably low wafer yield. Second, making the channel wider than 2/3 × the width of the constriction means a drastic decrease in rf-homogeneity, as can be deduced from Figure 3.4a. As long as these ratios are maintained, the chip can be scaled to larger and smaller volumes, but will always give the optimal sensitivity for a chip consisting of two channels as shown in Figure 6.1.

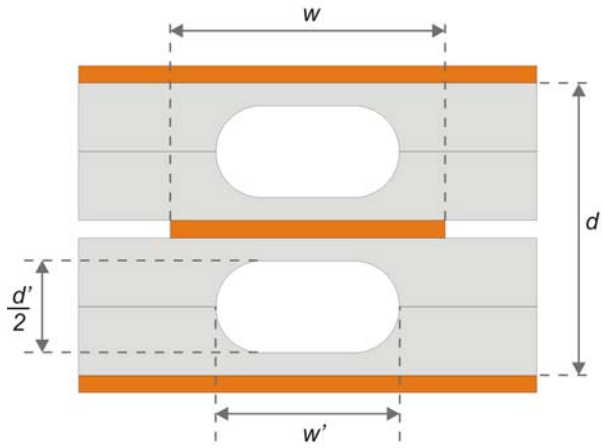

Figure 6.1. Cross-sectional view at the center of the constriction of a glass-based stripline chip design with two fluidic channels.

The observed volume of the chip depicted in Figure 6.1 is approximately given by:

$$V = w'd'l \tag{6.1}$$

where V is the volume, w' is the width of the channel and d' is the depth of a single channel. Using the optimal ratios for w/d and l/w the key parameter w, from which all other parameters can be derived, can be calculated using:

$$w = \sqrt[3]{0.9V} \tag{6.2}$$

As is shown in Figure 6.1, the channels are designed as buried channels. For this approach four glass substrates, each containing a half channel, have to be positioned on top of each other. For the aimed sample size of 600 nL, Eq. 6.2 gives w=650 µm. Since w/d=1, the total stack thickness is also 650 µm, and therefore one substrate should have a thickness of 165 µm. Since 150 µm thick glass substrates are commonly available, these were used, resulting in a total stack thickness of 600 µm, a stripline width of 600 µm and an observed volume of 428 nL.

For comparison of the sensitivity with the silicon chip, the LOD was calculated according to the description in Chapter 2. In this calculation, numerically determined values for B_1/i and the resistance R were used. The LOD of the optimized design in glass was $1.9 \cdot 10^{13}$ spins/√Hz, assuming a lossless substrate. In Chapter 3 the sensitivity of a chip design based on one channel was predicted, being $3.1 \cdot 10^{13}$ spins/√Hz, also assuming a lossless substrate. The sensitivity enhancement is therefore a factor of 1.68. This is in very good accordance with the general rule described in Chapter 2, that the sensitivity of an NMR detector scales inversely with

its dimension. In this case the dimension, represented by the stripline width *w*, scales from 1 mm to 0.6 mm and therefore a sensitivity enhancement of 1/0.6=1.67 is predicted.

Substrate

Silicon has turned out to be too lossy in electrical terms, to be a suitable substrate for high Q-factor stripline-based NMR detectors. Apart from that, the λ/2 stripline implementation limits the possibility to add extra electrical channels for other nuclei or locking. The use of a different substrate which has lower losses, together with a different rf-implementation could solve these problems.

The most obvious alternative for silicon is low-loss glass, *e.g.* crystalline SiO_2 (quartz) or amorphous SiO_2 (fused silica). Glass has a low dielectric permittivity ε_r compared to silicon, which allows for the implementation as an inductive element in an external LC-resonator (see Chapter 2, Fig. 2.8a). Furthermore, glass does not suffer from high temperature treatments, in contrast to silicon equipped with a surface passivation layer (amorphous silicon). This allows for other fabrication methods like fusion bonding which is not useable for silicon-based stripline chips. Finally, glass has become a standard substrate for the fabrication of fluidic channels, and several optimized and cleanroom compatible processes are available.

As calculated above, thin substrates are required to achieve a high filling factor for the aimed volume. Fused silica substrates are available in these thicknesses; however it is technically very challenging to fabricate them because of their fragility. Furthermore, the surface smoothness is generally worse than thicker substrates, because the fragility limits the suppliers in terms of polishing possibilities. For proper fusion bonding a high surface smoothness (< 2 nm) is required. Surface smoothness is the main reason why borosilicate glasses are used as substrates in microfabrication. The additives in borosilicate glasses make the processability much easier, so that suppliers deliver very smooth substrates.

In view of the processability, we have chosen a borosilicate glass substrate as an intermediate step to evaluate the processing of the four-stack design. In the future, the same process should be performed on a low-loss glass.

The structuring of glass can be performed in two ways. First, by means of a dry physical/chemical process called reactive ion etching (RIE) which produces anisotropic structures.[1] Second, by means of wet chemical etching (most commonly in hydrofluoric acid, HF) which results in isotropic structures.[1] Since anisotropic etching in glass is extremely slow at the present state of technological development, this process is only suitable for a typical depth up to 10 μm. The channel depth

which was needed for the chip described in this chapter was far more than 10 µm, and therefore HF-etching was utilized.

Fluidic connections

Side-inlets were used for the microfluidic connection.[2] Side-inlets are fabricated by making use of the isotropic shape of wet-etched channels in glass. By patterning a semicircular channel in two substrates which have to be bonded on top of each other, the resulting closed channel is circular (see detail Figure 6.2), and when the proper diameter is chosen, fused silica capillaries can be glued in from the side (called side-inlets) resulting in a very reliable connection. Compared to commonly used out-of-plane connections, based on PEEK interfaces with NanoPort™ assembly tools,[3,4,5] this in-plane connection typically has lower dead volumes. Limitation of dead volume is required for mass-limited samples (see Chapter 5), but also advantageous for reaction monitoring (see Chapter 4) since the reaction volume is reduced, resulting in an enlargement of the time window for kinetics monitoring. Another advantage of side-inlets is that it saves one process step, since out-of-plane holes for fluidic access are not necessary: the fluidic access is from the side, which is opened during dicing of the final chip.

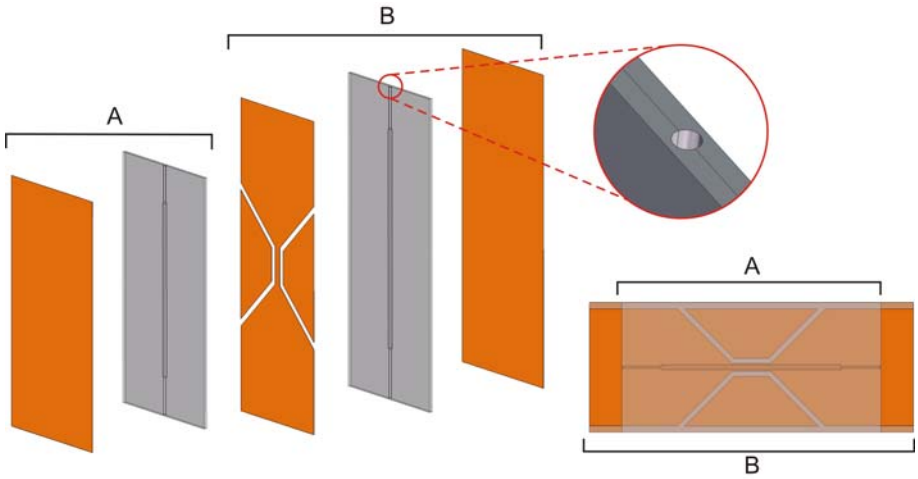

Figure 6.2. An exploded view of the glass chip. The chip consists of two separate parts, A and B, which are laid on top of each other. Part A has the same width as part B, but is shorter, such that the central line can be accessed for the rf-connection. For clarity, the ground plane on part A is not shown in the right picture. The detail shows the side-inlet design based on the isotropic etching of two semicircles in two substrates which subsequently are bonded together.

rf-connections

In contrast to a λ/2 resonator, the implementation depicted in Figure 2.8a, requires metallic connections from the central line to the external capacitors to establish an LC-resonator circuit. Therefore, the bottom part of the chip (B) containing the central line, was designed longer than the top part (A) giving access to the central line, see Figure 6.2. According to Figure 2.8a, one side is directly connected to ground whereas the other side is connected to the lumped element circuit.

Experimental

Chip Fabrication

A detailed description of the chip fabrication process is included in Appendix B. In this section, the main process steps are addressed and elucidated in Figure 6.3. Borosilicate glass wafers (D263T thin glass, thickness 150 µm, diameter 100 mm, Schott Technical Glasses AG, Germany) were used as a substrate.

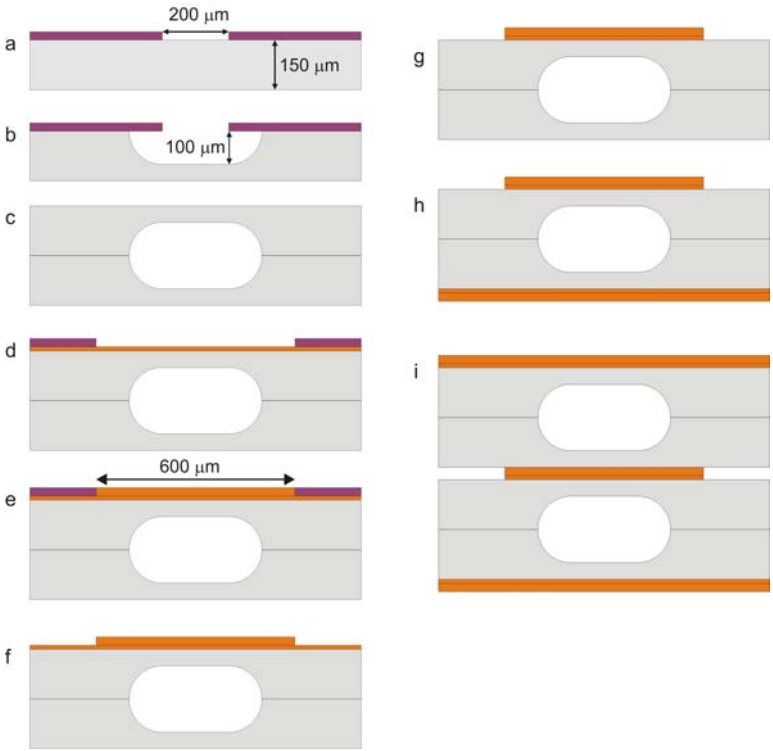

Figure 6.3. Process scheme for the fabrication of stripline based NMR chips in glass. See text for explanation.

For defining the fluidic channel geometry, the front side of the glass substrate was sputter-coated with a gold-chromium layer (200 nm Au, 15 nm Cr). This metal thin-film was patterned using photoresist (Olin 907-17, standard UV-lithography), Au-etchant and Cr-etchant. The patterned Au/Cr thin-film acted as a mask layer (Fig. 6.3a) for the realization of microchannels (depth 100 µm, width 400 µm) using isotropic etching in 10 % hydrofluoric acid (Fig. 6.3b). The backside of the substrate was completely covered with a resist-gold-chromium layer.

The channel mask was designed symmetrically, such that two wafers patterned with this mask could be bonded with the etched sides facing each other. A prebond was established in a mask-aligner operating in bond-alignment mode, after which the bond was annealed at 570 °C for 1 hour (Fig. 6.3c).

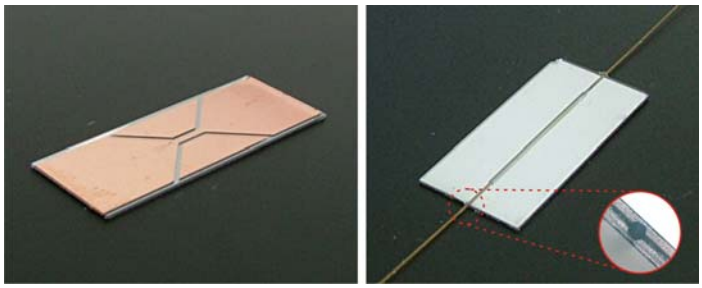

Figure 6.4. The two parts of the glass-based stripline chip. The left picture shows a glass stack containing a microfluidic channel and the stripline structure on top. The right picture shows part B, which also has a microfluidic channel, but is shorter, and does not contain the stripline structure. Both chips have ground planes at the backside. The left picture shows the side inlets, making use of the circular channel ends (inset).

The bonded stack was sputter-coated from the front side with a copper-chromium layer (200 nm Cu, 15 nm Cr) to achieve a seed-layer necessary for electroplating. Thick-film photolithography of 25 µm (AZ9260, Clariant, Wiesbaden, Germany) was utilized on this seed-layer to pattern the central stripline structure (Fig. 6.3d). A home-built electroplating set-up, based on Slotocoup HL10 bath chemistry (Schlötter GmbH, Geislingen, Germany) and a DµP(R)10-1-3 powersupply (Dynatronix Inc., USA) operating in DC-mode, was used for the plating procedure. With a current density of 1 A/dm^2 a copper layer with a thickness of 10 µm (>3 times the skin depth of copper at 600 MHz) was received in 18 minutes (Fig. 6.3e). After the resist was removed (Fig. 6.3f), the remaining seed layer was removed by ion beam etching (IBE) to isolate the separate structures electrically (Fig. 6.3g). Subsequently, the ground planes were fabricated on the backside of the stack using the same process (Fig. 6.3h). The chips were diced utilizing a standard wafer saw

after which the stack consisting of part A and B (Fig. 6.2) could be built up (Fig. 6.3i). Figure 6.4 shows a photograph of two fabricated chip parts, together with a detail of the fluidic inlet.

Probe fabrication

The stripline was implemented as an inductive element in an LC-resonator circuit. For the probehead, a similar design as discussed in Chapter 3 was used. An aluminum cylinder (9 mm ID, 11 mm OD, length 60 cm) was divided in two halves. Trenches of 0.3 mm deep were milled in both halves in which the 0.6 mm thick stack could be placed, resulting in a non-radiative cylindrical structure. The return line connection was established by the direct contact between the copper shielding planes and the aluminum.

NMR experiments

The NMR experiments were carried out on a Chemagnetics CMX-Infinity 600 solid-state NMR spectrometer (600 MHz) operated by Spinsight software. Spectra were recorded at 300K.

Results

Electrical performance

The Q-factor of the probe was 36, a moderate number, indicating substantial losses in the chip. The losses were caused by the substrate, as was verified by implementing an unpatterned glass substrate as a dielectric in the LC-resonator described before (Chapter 3). The Q-factor of the LC-resonator with a 300 μm thick glass stack as a dielectric was 50. Taking into account the rf-soldering on the chip which attributes slightly to the total losses, this means that the substrate losses were dominant. Preliminary results for a more advanced probehead in which the rf-soldering is improved, show a Q-factor of 50, which is clear evidence that the losses are completely dominated by the substrate.

For comparison, two 150 μm thick fused silica test substrates (Valley design, USA) were implemented as a dielectric in the LC-resonator. For this substrate, a Q-factor of 130 was obtained. Such a Q-factor indicates minor substrate induced losses. A Q-factor of 130 is typical for liquid NMR probes, and it must be mentioned that too high Q-factors are not desirable because this will limit the excitation bandwidth.

Sensitivity and resolution

To evaluate the chip in terms of sensitivity and resolution, a mixture of water and ethanol (50%/50%, v/v) was measured, see Figure 6.5. Both channels were filled so that the detected volume was 428 nL. The Limit of Detection (LOD) as calculated from the Free Induction Decay (FID) was $2{,}5 \cdot 10^{14}$ spins/√Hz. As discussed above an LOD of $1.9 \cdot 10^{13}$ spins/√Hz was predicted for a lossless substrate, which means a deviation by a factor of 13.

The resolution of the methyl peak in Figure 6.5 was 2 Hz. Although this resolution is sufficient for most NMR experiments, it must be mentioned that it can be increased by means of susceptibility matching. In Chapter 3 it was shown that by filling the gap which defines the constriction with a material having a susceptibility matching copper, the resolution could be improved.

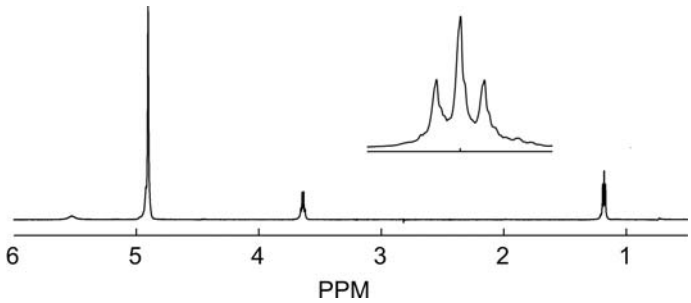

Figure 6.5. Single scan ^{1}H-spectrum of an ethanol-water mixture (50%/50%, v/v). The linewidth of the central methyl peak is 2 Hz.

Discussion

It has been shown that a stripline-based chip with an optimized filling factor could be fabricated in thin glass substrates (150 μm). The spectral resolution of the probe (2 Hz) was slightly lower than achieved with the silicon probe (0.7 Hz). However, this was expected since, in contrast to the silicon chip, no susceptibility matching was performed.

It was found that the sensitivity deviated by a factor of 13 from the sensitivity predicted on the basis of a lossless substrate. The losses are attributed to ionic additives in borosilicate glass, which are abundant in D263T glass (see Table 1). Apparently, the substrate choice for this optimized design was rather unfortunate in terms of sensitivity, although it is very well suitable for the fabrication of fluidic devices. Nevertheless, the geometrical design together with the fabrication

description are completely valid, and it is expected that the use of a proper substrate will provide the result which was aiming for.

For a proper selection, various glass substrates have to be evaluated with respect to their dielectric losses and processability. In Table 6.1, the composition of the most common glasses is shown together with the electrical properties (for 1 MHz) and the processability. The numbers are based on datasheets from the supplier and compared with literature.[6,7]

	Fused silica	Pyrex 7740	BF33	D263T	AF45
SiO_2	100	80	81	64	55
B_2O_3		13	13	8	14
Al_2O_3		3	2	4	
Na_2O		4	4	6	
TiO_2				4	
ZnO				6	
KaO			1	7	
CaO					30
tan δ	$1 \cdot 10^{-4}$	$5 \cdot 10^{-4}$	$37 \cdot 10^{-4}$	$61 \cdot 10^{-4}$	$9 \cdot 10^{-4}$
ε	3.8	4.1	4.6	6.7	6.2
rf	++	--	--	--	+
process	-	++	+	++	--

Table 6.1. Compositions and electrical properies of different common glass types. The 'rf' column indicates how suitable the substrate is for rf-applications, and the 'process' column indicates the processability by means of common microfabrication techniques. The values for *tan δ* and ε are specified for a frequency of 1 MHz.

It must be mentioned that data regarding substrate losses are often not available or they are limited to the MHz range. Therefore, the choice can not be based only on the data in Table 6.1, but the glass types have to be evaluated at the aimed frequency. As an example, the datasheet of Pyrex 7740 specifies a *tan δ* of $5 \cdot 10^{-4}$ at 1 MHz which is one of the lowest values of Table 6.1. However, Polyakov et al.[7] have shown that at higher frequencies (up to 10 GHz) the losses increase even above the losses of AF45 glass which has a higher *tan δ* at 1 MHz. Actually, AF45 is a well-established substrate for rf-MEMS (Micro Electro Mechanical Systems),[8,9,10] but suffers from a bad processability, especially for deep-channel structures.[7] Since it is expected that borosilicate glasses will always detoriate the NMR sensitivity because of the

included salts, a pure SiO_2 substrate is favourite. Therefore, the evaluation of processability of thin fused silica substrates is in progress.

Conclusions

The fabrication of a stripline-based chip with an optimized filling factor in glass substrates was demonstrated. The device showed a spectral resolution of 2 Hz and an LOD of $2{,}5 \cdot 10^{14}$ spins/√Hz. The sensitivity was a factor of 13 lower than the predicted sensitivity, which was attributed to substrate losses. Appearantly, a proper substrate choice is really crucial for stripline-based NMR chips. The selection of a proper substrate which has low losses and sufficient processablility is in progress. Although the sensitivity was rather disappointing, the developed fabrication process is still valid, also for low-loss glasses.

References

[1] M.J. Madou, *Fundamentals of microfabrication*, CRC Press, Boca Raton (FL), USA (2002).
[2] R.M. Tiggelaar, F. Benito-Lopez, D.C. Hermes, H. Rathgen, R.J.M. Egberink, F.G. Mugele, D.N. Reinhoudt, A. van den Berg, W. Verboom, J.G.E. Gardeniers, *Chem. Eng. J.* 131, 163 (2007).
[3] V. Nittis, R. Fortt, C.H. Legge, A.J. de Mello, *Lab Chip* 1, 2, 148 (2001).
[4] Upchurch Scientific Inc., Oak Harbor, WA, USA (www.upchurch.com).
[5] M. Brivio, R.E. Oosterbroek, W. Verboom, A. van den Berg, D.N. Reinhoudt, *Lab Chip* 5, 10,1111 (2005).
[6] Schott Technical glasses, Mainz, Germany (www.Schott.com).
[7] A. Polyakov, P.M. Mendes, S.M. Sinaga, M. Bartek, B. Rejaei, J.H. Correia, J.N. Burghartz, Processability and Electrical Characteristics of Glass Substrates for rf Wafer-Level Chip-Scale Packages, *Proceedings of the 53rd Elec. Comp. and Techn. Conference*, 875, May 27-30 (2003).
[8] L.J. Fernández, E. Berenschot, R.J. Wiegerink, J. Flokstra, H.V. Jansen, M. Elwenspoek, *J. Micromech. Microeng.* 16, 862 (2006).
[9] H.A.C. Tilmans, W. de Raedt, E. Beyne, *J. Micromech. Microeng.* 13, 139 (2003).
[10] X. Rottenberg, R.P. Mertens, B. Nauwelaers, W. de Raedt, H.A.C. Tilmans, *J. Micromech. Microeng.* 15, 97 (2005).

– Chapter 7 –

Porous hollow fibers for in-line concentration of mass-limited biological samples

Introduction

The main bottleneck of NMR spectroscopy is the relatively low sensitivity of the NMR detection method. As a result, relatively high amounts of (concentrated) samples are required, while for the analysis of samples with low concentrations, the measurement times can become unacceptably long. Microcoils offer the possibility to decrease measurement time, since the same amount of spins can be measured in a more sensitive coil. Because this also implies that the solvent volume has to be reduced, a method to increase the concentration of certain compounds is required. For regular NMR on a 500 µL sample commercial concentration machines are available, which are based on the evaporation of water in an evacuated centrifuge, followed by dissolving the remaining matter in a lower amount of solvent. Similar methods may be used for microcoil systems, however, efficient delivery of nanoliter-volumes into such a microcoil, positioned inside a magnet, remains challenging. Sample handling losses and dilution during transfer are difficult to avoid in this smaller volume regime, so that only a small fraction of the original sample may eventually reach the microcoil. The situation is even more critical when the initial sample is already mass limited, as is the case for body fluids of small animals and plant extracts. Therefore it may be concluded that for this type of work, with nanoliter samples, standard laboratory equipment is of limited applicability.

Microfluidics offer the possibility to handle and treat tiny samples very efficiently with minimal losses. For example, microcoil NMR has been coupled to High Performance Liquid Chromatography (HPLC),[1,2,3,4,5] Capillary Electrophoresis (CE)[2,3,6,7] Capillary Electro Chromatography (CEC)[2,3,8] and Capillary Isotachophoresis (cITP).[9,10] The aim of this work was to simplify the identification of separated fractions by molecular structure identification using NMR. Although a problem with these methods is that they are operated in-flow which will lead to a limited residence time in the NMR coil and with that to limitations in signal averaging, the work demonstrates the efficient coupling of microfluidics to microcoil NMR.

This chapter describes a very simple, cheap and general purpose method for concentrating analytes in a microfluidic environment, based on evaporation through a porous hollow hydrophobic fiber. We aimed for a proof-of-principle set-up, with which 5 µL of 10 times concentrated sample could be obtained within 10 minutes. First, the principle will be explained; next the practical implementation will be demonstrated together with the experimental results.

Theory

Evaporation of the solvent is performed by means of a porous hydrophobic hollow fiber through which the aqueous solution is fed. If the selected fiber consists of a hydrophobic material, water will not penetrate the porous wall, but only a meniscus with a positive contact angle (*i.e.* $\theta > 90°$) will be formed in every pore, see Figure 7.1. By decreasing the partial pressure of water outside the fiber, water molecules at the surface of the positive meniscus in the pores of the membrane will rapidly evaporate and the water vapour will escape through the pore. Thus, the driving force for the separation is the difference in the partial pressures of the components on the two sides of the membrane and not the volatility difference of the components in the solution. Partial pressure differences can be applied by evacuation,[11] purging with an inert gas, application of an osmotic pressure[12] or a temperature gradient across the membrane.[12,13]

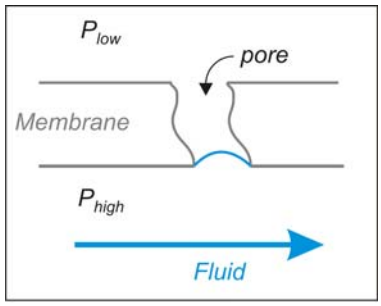

Figure 7.1. Schematic view of a hydrophobic membrane used for evaporation driven by a reduced partial pressure.

Hydrophobic porous hollow fibers are widely used in industry for a number of applications. Especially in food engineering, they are used for concentrating liquid food (*e.g.* fruit juice) in order to decrease transportation costs.[14]

For the work described in this chapter, the partial pressure is controlled by purging N_2 gas along the fiber. Since low concentration biological samples usually consist of close to 100% water, the water partial pressure will be effectively diminished, while that of the solutes will remain low. The latter is dictated by Raoult's law which states that the partial pressure of a solute is proportional to its mole fraction, which is very low for most of the solutes of interest in this work.[15] Furthermore, also according to Raoult's law, the partial pressure of the solvent, water, is hardly affected by the low amount of solute dissolved.[15] Finally, the vapour pressure of biomolecules is generally much lower compared to the vapour pressure of water at room-temperature. Therefore, effectively only water will evaporate.

In fact, the concentration mechanism is principally the same as is used for standard laboratory concentrators, based on evacuated centrifuges. The novelty of the concept based on a hollow fiber is the in-flow property, which makes it compatible to microfluidics. Operating this system in-flow, water will be separated selectively from the bulk, so that a higher concentrated solution will show up at the outlet of the system.

Model description and calculations

In Figure 7.2, a schematic representation of the hollow fiber evaporator (HFE) used for concentration of biological fluids is shown. The HFE has a length L and a radius R. The membrane wall thickness is assigned δ. A system of cylindrical coordinates is used to evaluate the HFE analytically.

The grey disk represents an infinitesimal small volume element that is used for composing mass balances over the HFE to calculate its dimensions. The volume element has an infinitesimal volume $dV = \pi R^2 dz$ and membrane contact area $dA = 2\pi R dz$.

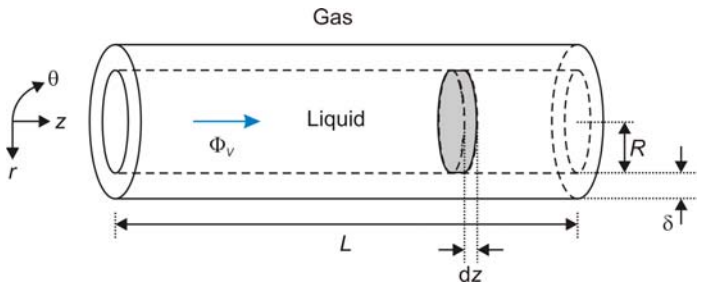

Figure 7.2. Schematic representation of a hollow fiber evaporator (HFE). Evaporation only happens at the inner wall of the fiber. The evaporation along the whole fiber is the integral of infinitesimal thin disks along the z-axis.

Mass balance

The mass balance of water (denoted with 'W') is derived based on the infinitesimal volume element of the HFE as shown in figure 7.2.

$$m_W\big|_z = m_W\big|_{z+dz} + m_{W,\text{evap}} \qquad 7.1$$

That is, the ingoing mass (at position z) of water equals the sum of the outgoing mass of water (at position $z + dz$) and the mass of water that has evaporated in the small volume dV. Using the density of the fluid, masses can be converted to volumes:

$$V\big|_z = V\big|_{z+dz} + V_{\text{evap}} \qquad 7.2$$

The volume of evaporated water through the infinitesimal surface dA during the retention time Δt of the fluid inside the HFE is given by:

$$V_{\text{evap}} = J_{\text{evap}}^{\text{vol}} \times \mathrm{d}A \times \Delta t \tag{7.3}$$

where $J_{\text{evap}}^{\text{vol}}$ is the volumetric flux of water vapour through the membrane (in $m^3/m^2 \cdot s$). $J_{\text{evap}}^{\text{vol}}$ is dependent on the permeability $\wp$ of the membrane material to water vapour ($m^2/Pa \cdot s$), the thickness of the membrane δ and the partial pressure difference between the fluid phase and the gas phase $p_W^{\text{F}} - p_W^{\text{G}}$.

$$J_{\text{evap}}^{\text{vol}} = \frac{\wp}{\delta}\left(p_W^{\text{F}} - p_W^{\text{G}}\right) = \frac{\wp}{\delta} p^{\circ} \tag{7.4}$$

The last part of the equation is valid under the assumption that the partial pressure for water vapor is equal to zero outside the membrane. In practice this is achieved either by imposing a constant vacuum on the gas side, or by continuously purging the gas side using an (inert) sweep gas. In this case, the partial pressure difference equals the saturated water vapor pressure $p°$, which can be calculated using the empirical Antoine equation:[16]

$$\log p^{\circ} = 5.40 - \frac{1839}{T - 31.7} \tag{7.5}$$

Substitution of Equations 7.4 and 7.3 in Equation 7.2 yields:

$$V\big|_z - V\big|_{z+\mathrm{d}z} = 2\pi R \mathrm{d}z \frac{\wp}{\delta} p^{\circ} \times \Delta t \tag{7.6}$$

Division of both sides by the retention time, Δt gives:

$$\Phi_V\big|_z - \Phi_V\big|_{z+\mathrm{d}z} = 2\pi R \mathrm{d}z \frac{\wp}{\delta} p^{\circ} \tag{7.7}$$

Division by dz and taking the limit d$z \rightarrow 0$ results in the following expression to describe the evaporation of water through the membrane in a HFE:

$$\frac{\mathrm{d}\Phi_V}{\mathrm{d}z} = -2\pi R \frac{\wp}{\delta} p^{\circ} \tag{7.8}$$

Solving of Eq. 7.8 is possible using the following boundary conditions:

$$\begin{aligned} &\mathrm{z} = 0 \quad \Leftrightarrow \quad \Phi_V = \Phi_{V,0} \\ &\mathrm{z} = \mathrm{L} \quad \Leftrightarrow \quad \Phi_V = \Phi_{V,L} = \Phi_{V,0}/\alpha \end{aligned} \tag{7.9}$$

where α is the concentration factor ($\alpha = \Phi_{V,0}/\Phi_{V,L} = c_L/c_0$). After integration the following expression is obtained:

$$\frac{\Phi_{V,0}}{\alpha} - \Phi_{V,0} = -2\pi R \frac{\wp}{\delta} p^{\circ}(L-0) \tag{7.10}$$

From Eq. 7.10, the desired concentration factor α can be expressed in terms of the dimensions and properties of the HFE:

$$\alpha = \frac{\Phi_{V,0}\delta}{\Phi_{V,0}\delta - 2\pi RL\wp p^{\circ}} \tag{7.11}$$

The permeability $\wp$ of the membrane material to water vapor is estimated from comparing the volumetric and mole flux of water vapour due to evaporation. The volumetric flux of water vapor through the membrane is given by Eq. 7.4; the mole flux of water vapor by:

$$J_{\text{evap}}^{\text{mol}} = \frac{D_W^{\text{eff}}}{\delta}\left(c_W^{\text{int}} - c_W^{\text{G}}\right) = \frac{D_W^{\text{eff}}}{\delta} c_W^{\text{int}} \tag{7.12}$$

where the superscript 'int' signifies the concentration of water at the gas/liquid interface. The last part of the equation is valid under the assumption that the evaporated gas is immediately swept after permeating the membrane wall. The water concentration at the interface is linked to the vapor pressure of water by using the ideal gas law:

$$p^{\circ} = R_g T \times c_W^{\text{int}} \tag{7.13}$$

where R_g is the gas constant (8.3145 J/mol·K) and T is the absolute temperature. The mole flux and volumetric flux are related as follows:

$$J_{\text{evap}}^{\text{vol}} = \frac{M_W}{\rho_W} \times J_{\text{evap}}^{\text{mol}} \tag{7.14}$$

where M_W is the molar weight of water, and ρ_W is the density of water. By substitution of Eqs. 7.4, 7.12, 7.13 and 7.14 it follows that:

$$\wp = \frac{M_W}{\rho_W} \times \frac{D_W^{\text{eff}}}{R_g T} \tag{7.15}$$

D_W^{eff} is the effective diffusion coefficient of water through the pores of the membrane, taking in account the porosity ε, and tortuosity τ, of the membrane:

$$D_W^{\text{eff}} = \frac{D_W \varepsilon}{\tau} \qquad 7.16$$

where D_W represents the diffusion coefficient of water vapour. The porosity describes the fraction of void space in the material, and the tortuosity is the actual (average) path length through the pores divided by the membrane thickness and thus corrects for any deviations of the pore shapes from a perfect cylinder.

Practical values

Equation 7.11 predicts the concentration factor α of an aqueous solution for a fiber (from which the dimensions L and R and the physical properties δ, ε and τ are known) as a function of the (inlet) liquid flow rate $\Phi_{V,0}$.

For a proof-of-principle, we used a commercially available polypropylene fiber (Accurel® PP Q3/2). From literature, the porosity of this fiber was found,[12] and the value of the tortuosity was estimated.[16] Table 7.1 shows all the relevant parameters in Eqs. 7.11 through 7.16, including the values for the commercial fiber which is used in this study.

Parameter	Symbol	Value	Unit [SI]
Flowrate at inlet	$\Phi_{V,0}$	Variable	m^3/s
Fiber length	L	Variable	m
Fiber radius	R	$300 \cdot 10^{-6}$	m
Wall thickness	δ	$200 \cdot 10^{-6}$	m
Porosity	ε	0.6	-
Tortuosity	τ	4	-
Molecular weight (water)	M_W	0.0180	kg/mol
Density (water)	ρ_W	1000	kg/m^3
Diffusion constant (water)	D_W	$2.60 \cdot 10^{-5}$	m^2/s
Vapor pressure (water)	$p°$	3120	Pa
Temperature	T	298	K
Gas constant	R_g	8.3145	J/mol·K

Table 7.1. Parameters in Eqs. 7.11 through 7.16 and their values for an aqueous sample based on a commercially available porous hollow fiber.

Equation 7.11 was explored for practical numbers, compatible with flowrates commonly used in microfluidic devices (0.1-200 µL/min) routing typical sample volumes in the order of microliters. Clearly, the speed at which the concentrate appears at the outlet of the fiber depends on the ratio of the fiber length and the flowrate. High flowrates combined with long fibers will provide the same concentration as short fibers operating under low flowrates, however, with a higher output rate. On the other hand, the hold-up volume (the internal volume) of the fiber is larger for longer fibers, which can be disadvantageous for mass-limited samples. Equation 7.11 predicts that, using a 10 cm fiber and a flow rate $\Phi_{V,0}$ of 5.5 µL/min yields the aimed concentration of 10 times (*i.e.* α = 10). The output flowrate of such a system is expected to be 0.55 µL/min, which leads to an acceptable time of 9 minutes for the collection of 5 µL sample.

Experimental setup

Figure 7.3 shows a schematic overview of the set-up that was used. A hydrophobic porous hollow fiber, made of polypropylene (Accurel® PP Q3/2, Membrana GmbH, Germany) with a nominal pore diameter of 0.2 µm, 60% porosity, an inner diameter of 600 µm, a membrane thickness of 200 µm and 10 cm length was used for the evaporation experiments. The hold-up volume was calculated to be 28.3 µL. Flexible fused silica capillary tubings (Polymicro Technologies, USA) with an inner diameter of 100 µm and an outer diameter of 360 µm, used as fluidic in- and outlets, were glued in the fiber by means of highly adhesive 2-component epoxy glue (UHU plus endfest 300, UHU GmbH, Germany), see Figure 7.4a.

From poly(methyl-methacrylate) (PMMA) a fiber-holder was fabricated, consisting of two parts (each 40×120×5 mm, l×w×h). In the bottom part, a flow-chamber (15×100×3 mm) with small in- and outlet trenches was milled by use of a CNC-lathe (Sherline Products inc., USA). The in- and outlet trenches, in which the fused silica capillaries could be fixed with a tiny droplet of glue, were milled with 0.5× the depth of the flow-chamber, such that the fiber in between the capillaries was freestanding, only kept in place by the glued capillaries. Nitrogen in- and outlet connectors were fabricated parallel to the axis of the fiber, warranting a rapid air refreshment in the flow chamber. The top part of the fiber-holder functioned as a lid, which was mounted with stainless-steel screws, (Fig. 7.4b). A nitrogen flow of approximately 50 cm^3/sec was set.

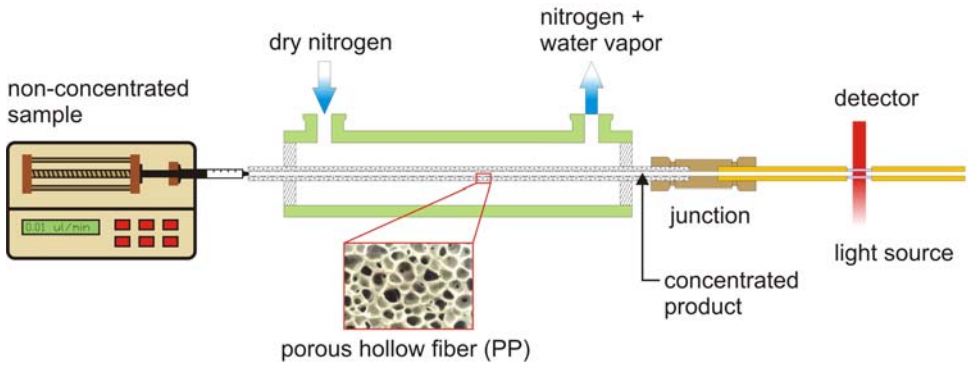

Figure 7.3. Schematic overview of the experimental set-up. A syringe pump delivers the diluted sample into the HFE, which is purged with nitrogen. The concentrated product at the outlet is fed into a spectrometric flow cell where the concentration is measured.

The inlet capillary was connected to a 500 µL syringe (Hamilton gastight) which was driven by a Harvard PHD 2000 syringe pump (Harvard Apparatus, United Kingdom).

For the measurements of the output concentration of the analyte after the HFE, a spectrometric set-up was used, equipped with a micro flow cell having an observed volume of 1 µL (Zeutec Opto-Electronic, GmbH, Germany), a miniature deuterium-tungsten-halogen light source (DT-Mini-2-GS, Ocean Optics, The Netherlands), and a high-resolution spectrometer (HR4000, Ocean optics, The Netherlands). The emission spectrum of the deuterium-tungsten-halogen light source was 200-410 nm (deuterium) and 360-2000 nm (tungsten-halogen). The flow cell was coupled to the light source and the spectrometer via solarization-resistant optical fibers (Ocean Optics, The Netherlands) with a core diameter of 600 µm.

The readout parameter of the spectrometer is the absorbance A, which is related to the concentration of the sample via the Beer-Lambert law:

$$A = E_m c l \qquad 7.17$$

where E_m is the molar extinction coefficient, c is the concentration and l is the optical path length of the light through the sample. Thus, for a fixed optical path length (being the sample diameter in the flow cell) the absorbance is linearly related to the concentration.

The outlet capillary of the HFE was connected to the inlet of the aforementioned flow cell, and the outlet of the flow cell was fed into a waste container via a capillary.

As a model fluid a solution of 22 µM phenolred (Sigma Aldrich) dissolved in distilled water was used. Phenolred exhibits a clear absorption at 432 nm, and therefore the tungsten-halogen light source was used.

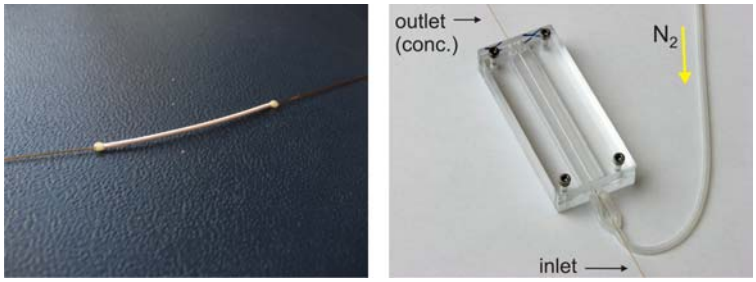

Figure 7.4. a) A polypropylene fiber, with capillaries glued using 2-component epoxy glue.
b) The PMMA based fiber holder with a fiber positioned in it. The tubing delivers the nitrogen flow.

Results

Before the concentration experiment was run, a calibration was performed by measuring the absorbance of 22 μM phenolred without using the HFE. The measured calibration absorbance was used to scale the results obtained during concentrating. The actual concentration experiment was run, starting from higher to lower flowrates. Figure 7.5 shows the increase in concentration as a function of the initial concentration.

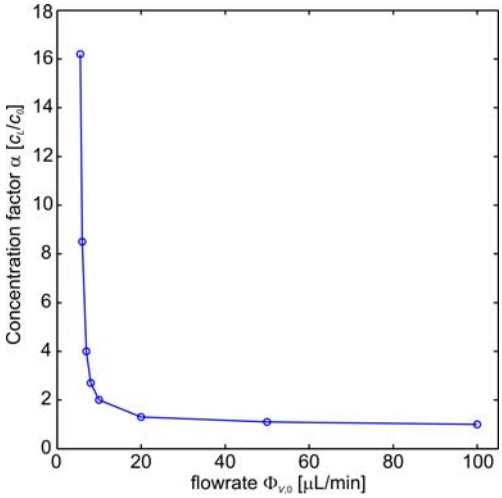

Figure 7.5. Concentration of phenolred in the HFE. For high flow rates, the evaporation is negligible and therefore, the relative outlet concentration remains unaltered (α=1). For decreasing flow rates, the evaporation increases resulting in higher outlet concentrations.

Clearly, at high flow rates the concentration factor is minimal, since the retention time Δt is very low (*e.g.* 17 seconds for 100 µL/min). The expected $1/x$ characteristic for the flowrate $\Phi_{V,0}$ (Δt is inversely proportional to $\Phi_{V,0}$) is visible. Therefore, at low flow rates a fast increase in concentration is observed. The highest concentration obtained in this experiment was 16.2 at a flowrate of 5.5 µL/min. This is higher than the predicted concentration of 10 with this flowrate, which is explained by a slightly higher membrane permeability (see below). Higher concentrations were measured, but not reproducibly. This was not because of malfunctioning of the HFE, but because of fluctuations in the N_2-line, caused by periodic charging of the N_2-net.

Although not the main scope of this research, it was found that the set-up is very well suitable for accurate determination of the membrane permeability $\wp$. Collecting all the constants except $\wp$ in Eq. 7.11 in one constant K yields:

$$\frac{1}{\alpha} = 1 - \wp \frac{K}{\Phi_{V,0}} \qquad 7.18$$

which is an equation in a form of y=Ax+B of which the slope A is determined by $\wp$. Plotting the same data from Figure 7.5, but with $K/\Phi_{V,0}$ on the x-axis and $1/\alpha$ on the y-axis results in a linear graph with slope $\wp$ as shown in Figure 7.6. Linear curve fitting gave a $\wp$ of $3.01 \cdot 10^{14}$, very close to the predicted $2.84 \cdot 10^{14}$, based on the values in Table 7.1. Apparently, evaporation under controlled conditions is a straightforward way to determine the permeability of a porous membrane.

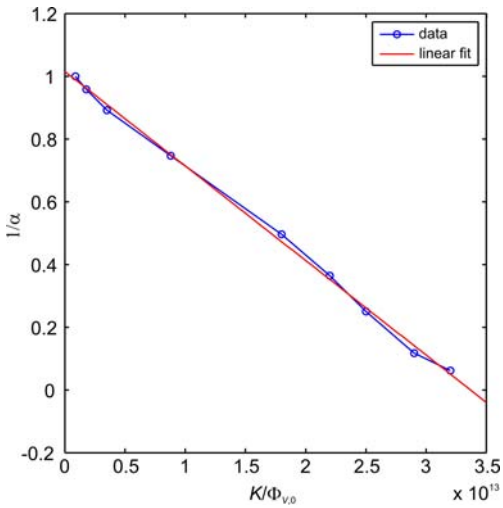

Figure 7.6. Permeability determination by fitting concentration data with linear function equivalent to Eq. 7.18.

Discussion

The HFE has shown to be an effective set-up for the concentration of aqueous samples. When optimized and calibrated, it requires minimal equipment, only a stable nitrogen stream. Since it is an in-flow system which can be directly coupled at the inlet to a syringe containing the raw sample and at the outlet to any detector, the system is fully compatible with microfluidics.

The predicted rate of evaporation of an HFE, based on the described model showed good agreement with the experimental results. Since the key parameter of a membrane, the permeability $\wp$ could be determined accurately, the presented model can be used for the optimization of a membrane based evaporation system for mass-limited samples.

The presented HFE can be optimized in several respects. First, the hold-up volume is rather high which limits the applicability for very small samples. Actually, a wide fiber is disadvantageous in general, not only because of the high hold-up volume, but also because of a poor efficiency. Since evaporation only takes place at the surface of the fiber, the surface-to-volume ratio should be maximized, which points to the direction of longer and narrower fibers. Ideal would be a realization in a microfluidic device, in which a wide and undeep channel is etched in a substrate which is closed by means of a hydrophobic membrane from the top. Such structures, although built for other purposes, are shown in literature.[17]

The HFE can become a very useful tool for micro-NMR. When implemented in a microfluidic device, exhibiting fast concentration and a low hold-up volume, it can be utilized for the concentration of samples which are mass-limited, without any preparative manual treatment. Even for a low concentration factor (*e.g.* 10 times) it should be realized that a signal gain of a factor of 10 will bring down experiment time by a factor of 100 which can easily bring the measurement times for various experiments so far unattainable down to a feasible level. It must be mentioned, that the concentration limit is in principle not set by the HFE but rather by the solubility of the molecules under study. Too high concentrations will lead to sedimentation resulting in NMR peak broadening, or loss of material by deposition somewhere in the fluidic path towards the NMR detection volume. For that matter, the HFE can be used as a fast tool for the determination of the maximal solubility.

Conclusions

Porous hollow hydrophobic fibers have shown their suitability for the concentration of aqueous solutions. Compared to other concentration methods described in

literature, the set-up is very simple and cheap. Comparison of the described model with the experimental results showed that the concentration rate is well predictable. A maximal concentration factor of 16.2 was achieved in a 10 cm long hollow fiber, with a flow rate of 5.5µL. The proof of principle shown here can be optimized for implementation in a fluidic chip. Being implemented, such a fluidic device is promising for NMR spectroscopy on low concentration biological samples.

References

[1] R. Subramanian, W.P. Kelley, P.D. Floyd, Z.J. Tan, A.G. Webb, J.V. Sweedler, *Anal. Chem.* 71, 5335 (1999).
[2] P. Gfrorer, J. Schewitz, K. Pusecker, E. Bayer, *Anal. Chem.* 71, 315A (1999).
[3] K. Pusecker, J. Schewitz, P. Gfrorer, L.-H. Tseng, K. Albert, E. Bayer, *Anal. Chem.* 70, 3280 (1998).
[4] N. Wu, A. Webb, T.L. Peck, J.V. Sweedler, *Anal. Chem.* 67, 3101 (1995).
[5] M.E. Lacey, Z.J. Tan, A.G. Webb, J.V. Sweedler, *J. Chromatogr. A* 922, 139 (2001).
[6] D.L. Olson, M.E. Lacey, A.G. Webb, J.V. Sweedler, *Anal. Chem.* 71, 3070 (1999).
[7] N. Wu, T.L. Peck, A.G. Webb, R.L. Magin, J.V. Sweedler, *J. Am. Chem. Soc.* 116, 7929 (1994).
[8] P. Gfrorer, L.-H. Tseng, E. Rapp, K. Albert, E. Bayer, *Anal. Chem.* 73, 3234 (2001).
[9] R.A. Kautz, M.E. Lacey, A.M. Wolters,F. Foret, A.G. Webb, B.L. Karger, J.V. Sweedler, *J. Am. Chem. Soc.* 123, 3159 (2001).
[10] A.M. Wolters, D.A. Jayawickrama, C.K. Larive, J.V. Sweedler, *Anal. Chem.* 74, 2306 (2002).
[11] K.B. Petrotos, N.H. Lazarides, *J. Membr. Sci.* 49, 201 (2001).
[12] V.D. Alves, I.M. Coelhoso, *J. Food Eng.* 74, 125 (2006).
[13] S. Álvarez, F.A. Riera, R. Álvarez, J. Coca, F.P. Cuperus, S.Th. Bouwer, G. Boswinkel, R.W. van Gemert, J.W. Veldsink, L. Giorno, L. Donato, S. Todisco, E. Drioli, J. Olsson, G. Trägårdh, S.N. Gaeta, L. Panyor, *J. Food Eng.* 46(2), 109 (2000).
[14] B. Jiao, A. Cassano, E. Drioli, *J. Food Eng*, 63(3), 303 (2004).
[15] P. Atkins, *Physical chemistry,* 7th ed. Oxford University Press, Oxford, United Kingdom (2006).
[16] M. Mulder, *Basic Principles of Membrane Technology 2nd ed.*, Kluwer Academic Press, Dordrecht, The Netherlands (1996).
[17] J. de Jong, B. Ankoné, R.G.H. Lammertink, M. Wessling, *Lab Chip* 5, 1240 (2005).

– Chapter 8 –

Room-temperature intermediate layer bonding for microfluidic devices

Parts of this chapter will be published as:

J. Bart, R.M. Tiggelaar, M. Yang, S. Schlautmann, H. Zuilhof, J.G.E. Gardeniers, *Lab Chip*, accepted (2009).

Introduction

Bonding of two substrates is an important process during the fabrication of microelectro-mechanical systems (MEMS) and microfluidic devices (Labs-on-a-Chip). Over the years many different techniques have been developed for silicon and/or glass wafer bonding, of which direct bonding, anodic bonding, and intermediate layer bonding are the most frequently used.

Direct bonding employs high annealing temperatures in order to obtain a strong hermetic bond via a chemical reaction between hydroxyl-groups present at the surfaces of wafers, and requires clean and ultra flat surfaces (low roughness).[1] Typically, one needs a temperature above 1000 °C for silicon-silicon fusion, and between 450-650 °C for glass-glass fusion (depending on the type of glass). Direct bonding can also be performed below fusion temperatures, as well as for bonding of silicon wafers with an oxide or nitride layer. However, low- and intermediate temperature direct bonds are not as robust as fusion bonds. Generally, for direct bonding a low surface roughness (nm-range) is necessary, which requires rigorous, diligent and laborious cleaning procedures.[1,2,3,4,5] Direct bonding can be significantly improved by activation of the surfaces prior to contacting, *e.g.* by wet chemistry,[4,5] UV/ozone exposure,[6] plasma treatments,[2,7,8,9,10] or combinations of these methods. Anodic bonding (or field-assisted bonding) is done at moderate temperatures (150-500 °C), and utilizes a large electric field (200-1500 V) to create a robust, leak-free silicon-glass bond.[11] Due to the large attractive forces generated by the electric field, anodic bonding has less stringent requirements for the surface quality of substrates and particle-contamination compared with fusion and direct bonding.

The intermediate-to-high annealing temperatures, the necessity of acidic cleaning of substrates or the use of high electric fields make that these bonding techniques are not compatible with integrated complementary metal oxide semiconductor (CMOS) processes. The techniques are also detrimental for wafers that contain temperature-sensitive components such as metal thin-films, organic compounds and waveguides. Intermediate layer bonding (or adhesive bonding) was developed to avoid these issues, and puts lower demands on the substrates in terms of surface roughness and cleanliness. Adhesive bonding is performed at low temperatures, is insensitive to surface topography, tolerates micron-sized particles to some extent, due to the planarization by the intermediate layer, and has the ability to join different types of wafers.[12] In order to create a hermetic seal between two substrates via an intermediate, a thermal or photo curable resin (thickness at least several microns) is dispensed on one substrate, contacted with another

substrate after pre-curing, and cured at temperatures below 300 °C. Although spin-on sodium silicate solution (spin-on-glass; SOG) yield good bonds at temperatures in the range 90-200 °C,[13,14,15] polymers are mostly used as intermediate layer, because most polymer-based materials can be patterned photolithographically, which allows localized adhesive bonding. Void-free, low-temperature adhesive silicon-silicon, glass-glass and silicon-glass bonds are realized with polydimethylsiloxane (PDMS) or its prepolymer at 60-65 °C,[16,17] Nafion (a perfluorinated ion exchange polymer) at 120 °C,[18] polyimide, SU-8 and cyclic perfluoropolymer (Cytop) at 150-160 °C,[19,20,21,22] and benzocyclobutene (BCB) at 180-270 °C,[23,24,25] whereas room-temperature glass-glass adhesive bonding is possible with UV curable epoxy resins.[26,27,28,29] The quality of the adhesive bond, *i.e.* the absence of voids/gaps/bubbles after curing, highly depends on the curing time and temperature, as well as on the load pressure on the wafer stack. This load influences possible filling of fluidic channels with the adhesive material, which obviously should be avoided. This can be accomplished by selective coating of one of the substrates using a 'stick-and-stamp' method,[27] which also ensures that none of the channel sidewalls is contaminated with adhesive glue.[16,17,29] Pull tests have shown that the tensile strength of polymer-based adhesive intermediate bonds is very high for unstructured wafers (up to 20.6 MPa).[19,21,25] However, leakage-free intermediate layer bonding of structured substrates without contaminating fluidic structures with adhesive resin is not trivial, and the long-term stability of these adhesive bonds is limited due to moisture uptake and chemical reactivity of used resins.

Recently, bonding of unstructured wafers via 'chemical gluing' was reported: this intermediate bonding method is based on the anchoring of chemical functionalities on surfaces via monolayers of several nanometers in thickness, rather than the use of micrometer-thick resin layers. Hydroxylated and aminosilylated glass wafers were strongly bonded (bond strength 1.78 MPa) via formation of C-C covalent bonds by a Diels-Alder cyclo-addition reaction at 200 °C.[30] In another publication, strong, robust, leak-tight amine-epoxy bonds were formed at room temperature between aminosilane-functionalized and epoxysilane-functionalized surfaces.[31] Although this chemical gluing method has not yet been reported for fluidic devices, it is anticipated that this method greatly reduces the risk of clogging of micrometer-sized fluidic structures.

A drawback of bonding with monolayers is that the surface topography of the specimens to be bonded is limited to nanometers. To overcome this limitation, we have studied the use of a chemically-inert fluorinated ethylene propylene (FEP) foil in combination with chemical modification of the surfaces of both the foil and the

substrates by EDC-NHS chemistry. As a result, covalent amide-bond formation occurs at room temperature, thereby making this method very attractive for a wide variety of microfluidic devices which include temperature sensitive materials. In this contribution we will discuss the principle and the performance of the technique by applying it for sealing of microfluidic devices, which were tested for their pressure stability.

Principle

Fluoropolymers are the most chemically inert polymers, and remain stable in nearly all chemical environments. Although this inertness is useful, chemical surface modification is necessary to increase its chemical reactivity in order to be able to bond it to other materials. Therefore, the surface of the fluoropolymer has to be defluorinated, and the empty atomic sites must be terminated with proper functional groups. Partial de-fluorination can be accomplished by a variety of methods, such as wet chemical, plasma, irradiation, corona discharge, flame or ozone treatments.[32,33] Depending on the type of wet etchant various ranges of de-fluorination and incorporation of functional groups, like oxygen-, sulfur-, and silicon-containing groups, can be obtained. Often sodium-based etchants, such as sodium in liquid ammonia and sodium naphthalene, are used to increase the adhesion between fluoropolymers and a metallization layer.[32,34,35] Commercial FEP foil that is 'cementable', *i.e.* FEP foil which is made reactive by means of a corona treatment, can also be used to form a strong intermediate bond between glass substrates using a pressure-assisted thermal bonding method (7 MPa, 2h at 90 °C).[36] Disadvantage of a corona treatment is that, although it makes FEP foil reactive, the surface of the foil is composed of unidentified species, which makes reproducible and controllable surface modifications difficult. Therefore, we have chosen a wet-chemical approach, from which the resulting surface chemistry is predictable. Although many different chemical approaches are possible, we chose the covalent amide-bond formation between amine-terminated silicon/glass surfaces and surface-carboxylated FEP foil utilizing EDC-NHS chemistry. NHS-EDC chemistry is well-established in organic and bioconjugate chemistry, and has not only been shown to work in solution but also on surfaces.[37] EDC (1-Ethyl-3-[3-dimethylaminopropyl]-carbodiimide hydrochloride) is a zero-length crosslinking agent used to couple carboxyl groups to primary amines, typically via the formation of amine-reactive NHS-esters.[38] EDC reacts with a carboxyl to form an amine-reactive *O*-acylisourea intermediate, see Figure 8.1. When this intermediate does not encounter an amine, it will hydrolyze and regenerate the

carboxyl group. In the presence of *N*-hydroxysuccinimide (NHS), EDC can be used to convert carboxylic acid groups to amine-reactive NHS esters. This is accomplished by mixing the EDC with an acid-containing molecule and adding NHS. The addition of a sulfonic-acid moiety on the NHS group increases the water solubility of both the activated ester and the leaving group, which facilitates cleaning of the substrates after activation.

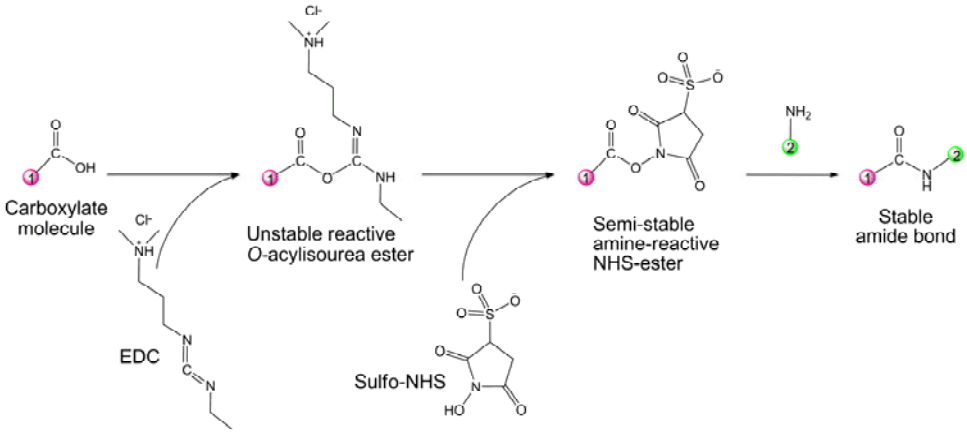

Figure 8.1. EDC-NHS chemistry: EDC reacts with a carboxylic-acid group on FEP foil (indicated by spheres with nr. 1), forming an amine-reactive *O*-acylisourea intermediate. This intermediate may react with an amine on silicon or glass (indicated by the spheres with nr. 2), yielding a conjugate of the two molecules joined by a stable amide bond. The addition of sulfo-NHS stabilizes the amine-reactive intermediate by converting it to an amine-reactive sulfo-NHS ester, thus increasing the efficiency of EDC-mediated coupling reactions.

Experimental section

Prior to use, all glassware was cleaned for at least 1 hour in ca. 2% v/v Helmanex solution in water, followed by rinsing with water and flushing with high-purity water (MilliQ, 18.2 MΩ·cm) and drying.

Preparation of silicon and glass samples

All bonding experiments described in this work were performed with silicon (Si) and glass samples onto which amine-terminated groups were coupled. Prior to amine immobilization on these surfaces, silicon and glass substrates were processed and cleaned as mentioned below.

Silicon substrates ({100}-oriented, p-type, resistivity 5-10 Ω·cm, 100 mm diameter, thickness 525 µm, single side polished, Okmetic, Finland) were diced (Disco DAD-321 dicing machine) into samples of 1 × 1 cm, which were ultrasonically

cleaned in DI water (10 min) and isopropanol (10 min; technical grade, BASF) and spin-dried.

Borosilicate glass substrates (Borofloat 33, 100 mm diameter, thickness 1.1 mm, Schott Technical Glasses, Germany) were ultrasonically cleaned by immersion in isopropanol (15 min; technical grade, BASF), subsequent immersion in fuming 100% nitric acid (15 min; Selectipur 100453, BASF), followed by quick dump rinsing in de-mineralized water and dry spinning. Subsequently, half of the amount of glass substrates was diced into samples of 2 cm × 1.5 cm, whereas the front side of the other glass substrates was sputter-coated with a gold-chromium layer (200 nm Au, 15 nm Cr). This metal thin-film was patterned using photoresist (Olin 907-12, standard UV-lithography), Au-etchant (105043, Merck) and Cr-etchant (111547.2500, Merck). The patterned Au/Cr thin-film acted as a mask layer for the realization of microchannels (depth 50 µm, width 350 µm, length 80 mm) using isotropic etching in 25% hydrofluoric acid (VLSI Selectipur, BASF). After quick dump rinsing in DI-water and spin-drying a photosensitive foil (BF410, Ordyl) was applied to the backside of the substrates. In this foil structures were defined using lithography, and powder blasting was used to create fluidic access holes to the microchannels (during powder blasting the front side of the wafers were covered with Riston protection foil). After removal of the foils, the substrates were ultrasonically rinsed in acetone (15 min; VLSI 100038, BASF), followed by removal of the photoresist layer and the Au/Cr layer, and dicing of the processed substrates into samples of 2 × 1.5 cm.

Amine immobilization on silicon and glass samples

A common and straightforward method to obtain amine-terminated silicon and glass surfaces is functionalization with an aminopropyl-triethoxysilane (APTES) monolayer, since APTES forms a self-assembled monolayer on silanol-terminated surfaces.[39,40,41] The silicon and glass samples in this work were functionalized with APTES. In order to have surfaces rich with hydroxyl groups (hydroxyl groups are necessary to anchor APTES molecules), directly prior to performing the formation of the amine-terminated layer on the silicon and glass, the samples were rinsed in 'Piranha' solution (15 min; 3:1 v/v mixture of 96% sulfuric acid (VLSI Selectipur, BASF) and 31% aqueous hydrogen peroxide (VLSI Selectipur, BASF)), followed by quick dump rinsing in DI-water, and drying with a nitrogen stream. Subsequently, the samples were positioned horizontally in a solution of 3% v/v 3-aminopropyl-triethoxysilane (APTES, 97%, ABCR GmbH, Germany) and ethanol (Pro Analysi, 100983.1000, Merck). After 2 hours the samples were cleaned ultrasonically in fresh

ethanol (5 min), followed by rinsing in ethanol and isopropanol and drying with nitrogen flow. The formation of a monolayer on the surface was verified with contact angle measurements, on a DataPhysics system in the sessile drop mode, for which fresh DI-water was used.

FEP foil treatment

Fluorinated ethylene propylene (FEP) foil was selected for intermediate layer bonding. FEP is a copolymer of hexafluoropropylene and tetrafluoroethylene, has superior chemical resistance, and is biocompatible. In this work 'general purpose' FEP foil was used (FEP type 100A, thickness 25 μm, DuPont, USA). Since a carboxylated surface was needed for EDC-NHS chemistry, fluorine had to be stripped from the carbon backbone. This was accomplished by means of FluoroEtch, a commercial etchant (Acton Technologies, USA).[42] During fluorine stripping Na atoms reduce the fluorine, forming Na cations and leaving a radical or a negative charge on the carbon atom. As soon as this free site is exposed to air it will be protonated or oxidized, resulting in a FEP foil of which the surface is rich in carboxyl groups. This fluorine stripping process takes place to a depth less than a nanometer, and the bulk of the polymer remains unaffected.[42]ripping process takes place to a depth less than a nanometer, and the bulk of the polymer remains unaffected.[42]

FEP foils were positioned in home-made circular Teflon clamp-holders arranged such that both sides of the foil will be treated when they are immersed in FluoroEtch etchant, which was done for 60 sec. The temperature of the etchant was 60 ± 2 °C, and since the etchant is very sensitive to oxidation it was used in a narrow glass battery beaker (opening width 2 cm, height and length 25 cm) while argon was bubbled through the solution. Subsequently, the foils were immersed in room-temperature isopropanol (15 min; technical grade, BASF) for 20 sec, in 70 °C DI-water (30 sec), stored for at least 15 min in room-temperature DI-water and dried with a nitrogen stream. After this fluorine-stripping process the foils had a brownish color, due to sodium naphthalene residues (Fig. 8.3). It was found that piranha solution effectively removes these residues; however, it also attacks the fluorine-free top layer. The combination of the temperature of the piranha solution and the etch time were crucial for obtaining FEP foils with surfaces rich in carbonaceous backbones for EDC-NHS chemistry: a temperature of 81 ± 3 °C and an etch time of 90 sec was found to be optimal (see Results and Discussion). After removal of the residues the foils were extensively flushed with DI-water, and dried with a nitrogen stream.

In high purity water 20 mM of N-hydroxy sulfosuccinimide sodium salt (sulfo-NHS; Sigma Aldrich) and 50 mM of 1-Ethyl-3-[3-dimethylaminopropyl]-carbodiimide hydrochloride (EDC; Sigma Aldrich) were dissolved. Reactive FEP foil slices (cut with a scalpel in slices of 1.5 cm × 1.5 cm and 2 cm × 2.5 cm) were horizontally immersed in this mixture. After 1 hour immobilization at room-temperature, the slices were turned upside down and left in the mixture for another hour. This sequence was performed in order to obtain sulfo-NHS modified FEP –foil with a homogeneous coverage on both sides of the foil. After immobilization the slices were rinsed with high purity water, ethanol to remove salts, and isopropanol to remove water, and dried with nitrogen flow.

After every of these process steps the FEP foil was characterized using contact angle measurements (fresh DI-water, sessile drop mode; DataPhysics system) and surface-sensitive X-ray photoelectron spectroscopy (XPS; Quantera system, Physical Electronics).

Bonding procedure

After the immobilization of an amine-terminated SAM on silicon and silicon dioxide samples and performing EDC-NHC chemistry on reactive FEP foil slices, stacks of silicon-FEP-silicon and glass-FEP-glass were prepared. On a support substrate (silicon wafer, 100 mm diameter), samples of silicon or glass were positioned with their amine-terminated side upwards. On these samples NHS-modified FEP slices were positioned (1.5 cm × 1.5 cm on silicon, and 2 cm × 2.5 cm on glass), after which the FEP slices were covered with silicon or glass samples in such a way that the amine-terminated side faced the NHS-modified FEP. After alignment of the samples the stacks were manually compressed, and another support substrate was positioned that covered all stacks. The cover substrate ensures a uniform force distribution on all stacks during application of a load on them, to enhance the coupling of amine groups with amine-reactive NHS esters. With a hydraulic plate system (Carver Inc., model 3851 CE) a load of 0.4 metric tons per square centimeter bond surface was applied for 15 hours at room temperature, or 4 hours at 75 °C. In this procedure, the load was installed after the system had heated up to the desired temperature.

Tests of FEP-based bonds

The strength of FEP-bonded silicon-silicon and glass-glass stacks was determined with tensile tests and leak tests. Onto the stacks of 1 cm × 1 cm brass pins were glued (Fig. 8.2a) using highly adhesive 2-component epoxy glue (UHU plus endfest

300, UHU GmbH, Germany), by means of which a pulling force could be applied on the stacks using a tensile test bench (Zwick/Roell Z020, Germany).

The maximum pressure that the fluidic stacks could withstand was determined with leak tests, performed under flow conditions. A stack was mounted in a home-made Teflon chip holder (Fig. 8.2b) and fluidic connections between the pump and chips were realized with Upchurch nanoport assembly parts and flexible fused silica capillary tubing (Polymicro Technologies, USA). For the inlet, a short capillary with a wide diameter was used (length 20 cm, O.D. 360 μm, I.D. 250 μm), whereas the outlet of the chip was connected to a capillary (length 70 cm, O.D. 360 μm, I.D. 100 μm). This long outlet-capillary ensured a constant pressure in the chip, since its hydraulic resistance was significantly larger than the hydraulic resistances of the short inlet tubing and the microfluidic channel in the chip. The flow of DI-water containing some drops of red ink (Trodat color 7011, used for visualization purposes) through the chips was increased until leakage was observed. Fluid flow was controlled by syringe pumps (Harvard PHD 2000 syringe pump and Hamilton syringes).

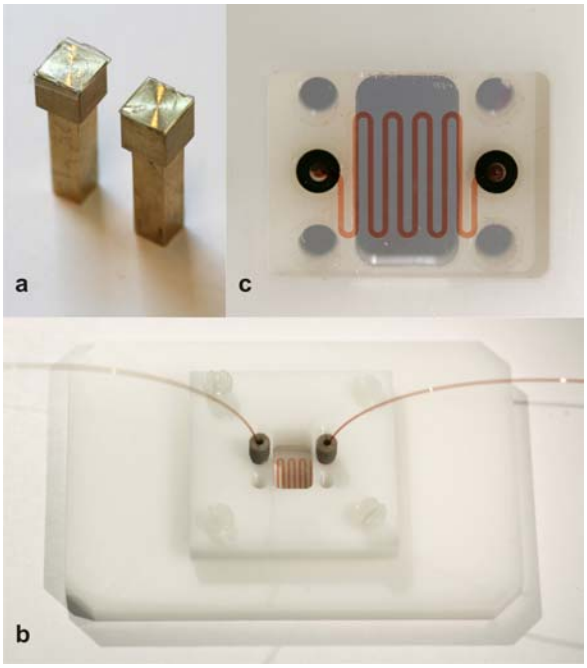

Figure 8.2. a) Photograph of a released glass-FEP-glass stack after tensile testing (glass and FEP on one pin, glass on the other pin). Brass pins were used for mounting the stacks in a tensile tester to determine the mechanical strength of the bond.
b) Home-made Teflon microfluidic chip holder with mounted glass chip.
c) Detail of the chip holder, showing the fluidic channel in the chip. DI water with a small amount of ink is visible in the fluidic channel.

Other stacks were exposed to endurance experiments in which DI-water containing red ink was continuously flushed through the microchannel at elevated pressures. Furthermore, in order to characterize the chemical inertness of the bonds, several stacks were flushed for 1 hour with ethanol, isopropanol, acetone, toluene, chloroform or a piranha solution prior to an endurance test performed with DI water.

Results and Discussion

APTES immobilization on silicon and glass samples

The silicon and glass samples were characterized before and after immobilization of APTES by means of contact angle measurements. Values on piranha-cleaned silicon and glass samples were 31° ± 1° and <3°, and after the amine immobilization process 62° ± 5° and 57° ± 4°, respectively. The contact angles measured on APTES-treated silicon and glass samples are in agreement with data reported in literature[43] and confirm the proper immobilization of an amine-terminated self-assembled monolayer (SAM) on the samples.

FEP foil activation

During the activation treatment, the FEP foils were characterized by means of XPS and contact angle measurements. This was necessary since every step of the activation process relied on proper previous steps.

The brownish colour of the foil observed after the fluorine stripping (Fig. 8.3a) indicated that a residual layer of sodium naphthalene was remaining on the surface. Therefore, it was proposed that after fluorine stripping the surface is as depicted in Figure 8.3b. This proposition was verified by XPS analysis and contact angle measurements (Table 8.1). It has been reported that the contact angle of a densely packed hydrophilic carboxylic acid-terminated surface is typically below 25° but can be lower depending on the surface smoothness and layer-density.[44,45] However, the contact angle of 37.1° measured after fluorine stripping indicated another surface composition, which can probably be addressed to partially oxidized naphthalene residues, since XPS data showed a hydro-carbonaceous surface after fluorine stripping (step 1). XPS data performed at several stages during residual layer removal (step 2) clearly showed a reduction of the residual layer, and a gradual return to the surface composition of the bare foil. Most likely, the residual layer was removed in ~30 seconds, after which the fluorine-free layer started to be attacked.

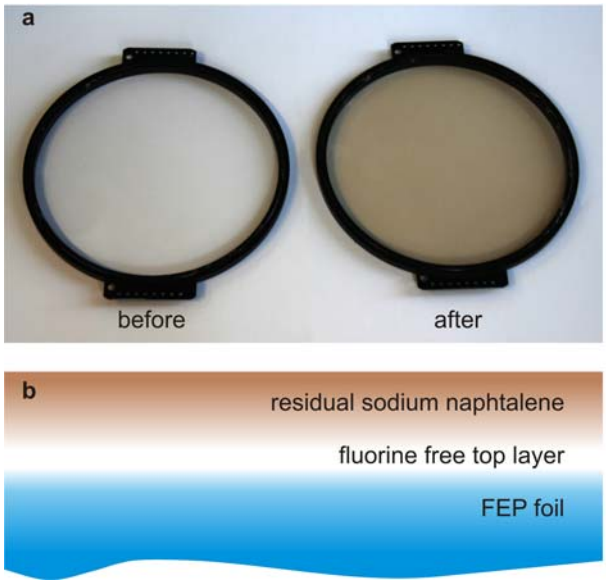

Figure 8.3. a) A comparison between photographs of new foil (left, as received) and a foil after fluorine stripping (right), indicating the appearance of a brownish layer of the residual naphthalene.
b) Proposed layer build-up after fluorine stripping utilizing sodium naphthalene. The etchant indeed removed fluorine from the carbon backbone, but etchant-residues remained on the surface after rinsing.

step	process	XPS				contact-angle (°)
		C1s	O1s	F1s	N1s	
0	Bare foil	32.1	-	67.9	-	108.0
1	Fluorine stripping	80.3	19.7	-	-	37.1
2	30 sec piranha	64.7	35.0	0.3	-	5.5
	60 sec piranha	61.8	36.2	2.0	-	3.8
	90 sec piranha	60.0	34.9	5.1	-	4.4
	120 sec piranha	58.3	33.6	8.1	-	5.1
	300 sec piranha	38.1	8.6	53.3	-	58.4
3	EDC-NHS immob.	64.7	22.4	5.6	7.3	27.7

Table 8.1. XPS and contact angle results obtained during activation treatment of the FEP foil. After fluorine stripping (step 1), a thick layer of organic residue remained on the surface, which could be removed by piranha cleaning (step 2). In the optimized process, step 2 was set to 90 seconds. After cleaning, a fluorine-free top-layer was achieved, which was carboxylated in H_2O. EDC-NHS chemistry was performed using this carboxylated surface (see text).

This was confirmed by complete disappearance of the brownish colour, and the increasing fluorine peak in the XPS data. When step 2 was performed for more than 300 seconds, the fluorine-free layer was completely removed and bare foil characteristics were measured at the surface, both with XPS and contact angle measurements. A minimum in contact angle was found for an etch time of 60 to 90 seconds. Therefore, it was concluded that an optimized activation treatment consists of piranha cleaning for another 60 seconds after the removal of the residual layer (i.e. the total time of step 2 was 90 seconds), in order to be sure that no contamination remained on the foil and that homogeneous fluorine stripped FEP-surface was created. The contact angle after 90 seconds piranha cleaning was below 10°, which indicated a carboxylic acid-rich surface.

Also after the EDC-NHS immobilization (step 3), XPS and contact angle measurements were performed. A significant change in the nitrogen content, as measured with XPS, indicated that immobilization indeed occurred.

Mechanical and fluidic performance of FEP-based bonds

To characterize the bond strength of silicon-FEP-silicon and glass-FEP-glass stacks, a commercial tensile tester was used. It has to be mentioned that all the bonded stacks passed dicing without problems, which already indicates a strong bond. Moreover, initial razor blade tests[46] failed since the interfaces were bonded too tight for placing a blade in between the substrates.

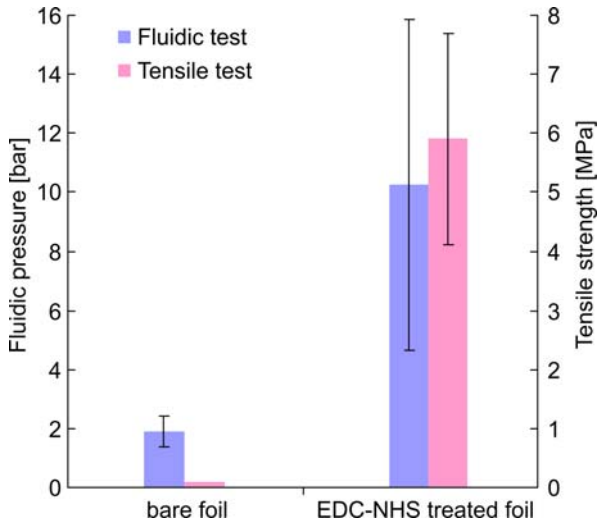

Figure 8.4. Comparison of the mechanical and fluidic bond strength for bonds with bare foil and EDC-NHS treated foils (averaged over 14 samples; bars show standard deviation of the data).

Figure 8.4 shows the tensile strength for silicon-silicon stacks bonded with either bare foil or EDC-NHS treated foil. Clearly, the mechanical strength is enhanced by the chemical treatment. Stacks bonded at slightly elevated temperatures (75 °C) showed comparable numbers. For glass-glass stacks similar values were found: 5.2 ± 0.6 MPa, which was expected on the basis of the comparable contact angle values for silicon and glass after APTES immobilization, indicating an highly similar surface termination.

To establish the maximal fluidic pressure that FEP-based bonds can withstand, water was pumped through the chip at increasing flow rates in the set-up of Figure 8.2b, until leakage was observed. Figure 8.4 shows results for chips bonded with either bare or EDC-NHS treated foil. A substantial increase in maximum fluidic pressure was observed for chips bonded with the chemically treated intermediate: an average pressure of ~10 bar and a maximum pressure of 23.2 bar were achieved. For chips stored for 2 months in ambient air at room temperature similar pressure values were obtained, which shows the stability of the bond. Such a pressure corresponds to a flow rate higher than 250 μL/min in a 70 cm long outlet capillary (I.D. 100 μm). A broad range of fluidic devices operate far below such pressures and flow rates, which makes this bonding method very promising for these devices.

Chemical compatibility of FEP-based bonds

Although this work essentially aimed for a room-temperature bonding mechanism for microfluidic chips routing water based (biological) solutions, the resistance of the FEP-based bond against several solvents was examined. Table 8.2 summarizes the findings for different chemicals that were all run through the chips at pressures of ca. 4 bar for 1 hour.

Compound	Time	Observation
Water	>1 hr	No effect
Ethanol	>1 hr	No effect
Isopropanol	>1 hr	No effect
Acetone	>1 hr	No effect
Toluene	>1 hr	No effect
Chloroform	>1 hr	No effect
Piranha	10 min	Leakage at 2.5 bar

Table 8.2. Resistance of the EDC-NHS bond to a variety of liquids. All observations are based on at least 3 experiments except for piranha (1 chip).

Clearly, the use of standard organic solvents did not introduce any leakage or bond failure. However, the bond was weakened by piranha solution. This is likely due to oxidation of the hydrocarbon chains by the extremely oxidizing piranha solution. From Table 8.2 it can be concluded that the method is suitable for bonding of microfluidic devices that have to handle aqueous and mild organic solvent solutions.

Conclusions

A room-temperature bonding technique for glass and silicon substrates, based on chemically activated Fluorinated Ethylene Propylene (FEP) films as an intermediate between chemically activated substrates, was developed and characterized. Surfaces of silicon and glass substrates were modified with APTES bearing amine ($-NH_2$) terminal groups, while FEP foil surfaces were treated to form carboxyl groups and subsequently activated by means of EDC-NHS chemistry. The activation of silicon and glass substrates as well as the FEP foil was studied by contact angle measurements and XPS. Bonding was successfully realized by simply pressing the two amine-terminated substrate surfaces together with NHS ester-terminated FEP foil in between. The bonding process was performed at room temperature. An average tensile strength of 5.9 MPa and 5.2 MPa was achieved for silicon-silicon and glass-glass bonds, respectively. The average fluidic pressure that could be operated was 10.2 bar. It was demonstrated that the chips handle mild organic solvents at elevated pressures without leakage problems. Only for an extremely oxidizing piranha solution leakage at higher pressures was observed.

The room-temperature intermediate layer bonding technique developed in this work has a high potential for bonding, packaging, and assembly of various (bio-) chemical microfluidic systems and MEMS devices. Although not shown in this work, the implementation of metal thin-film electrodes is feasible, and furthermore, since FEP is a proton-free material, this bond can be integrated in chips which require the absence of protons, like ^{1}H-NMR-chips.[47]

References

[1] M.J. Madou, *Fundamentals of microfabrication*, CRC Press, Boca Raton (FL), USA (2002).
[2] .W. Bower, M.S. Ismail, B.E. Roberts, *Appl. Phys. Lett.* 62, 3485 (1993).
[3] N. Chiem, L. Lockyear-Shultz, P. Andersson, C. Skinner, D.J. Harrison, *Sens. Actuators B* 63, 147 (2000).
[4] Q.-Y. Tong, Q. Gan, G. Fountain, P. Enquist, R. Scholz, U. Gösele, *Appl. Phys. Lett.* 85, 3731 (2004).
[5] Q.-Y. Tong, G. Fountain, P. Enquist, *Appl. Phys. Lett.* 89, 042110 (2006).
[6] Z. Lin, G. Liao, Z. Tang, T. Shi, *Microsyst. Technol.* 15, 317 (2009).
[7] H. Takagi, R, Maeda, T.R. Chung, T. Suga, *Sens. Actuators A* 70, 164 (1998).
[8] P. Amirfeiz, S. Bengtsson, M. Bergh, E. Zanghellini, L. Börjesson, *J. Electrochem. Soc.* 153, 2693 (2000).
[9] M.M.R. Howlader, S. Suehara, T. Suga, *Sens. Actuators A* 127, 31 (2006).
[10] M. Eichler, B. Michel, M. Thomas, M. Gabriel, C.-P. Klages, *Surf. Coat. Technol.* 203, 826 (2008).
[11] G. Wallis, D.I. Pomerantz, *J. Appl. Phys.* 40, 3946 (1969).
[12] F. Niklaus, G. Stemme, J.-Q. Lu, R.J. Gutmann, *J. Appl. Phys.* 99, 031101 (2006).
[13] R. Puers, A. Cozma, *J. Micromech. Microeng.,* 7, 114 (1997).
[14] H.Y. Wang, R.S. Foote, S.C. Jacobson, J.H. Schneibel, J.M. Ramsey, *Sens. Actuators B.* 45, 199 (1997).
[15] D. Goustourides, K. Minoglou, S. Kolliopoulou, S. Chatzandroulis, P. Morfouli, P. Normand, D. Tsoukalas, *Sens. Actuators A.* 110, 401 (2004).
[16] H. Wu, B. Huang, R.N. Zare, *Lab Chip* 5, 1393 (2005).
[17] B. Samel, M.K. Chowdhury, G. Stemme, *J. Micromech. Microeng.* 17, 1710 (2007).
[18] B. Ilic, P. Neuzil, T. Stanczyk, D. Czaplewski, G. Jordan Maclay, *Electrochem. Solid-State Lett.* 2, 86 (1999).
[19] F. Niklaus, P. Enoksson, E. Kalvesten, G. Stemme, *J. Micromech. Microeng.* 11, 100 (2001).
[20] P. Svasek, E. Svasek, B. Lendl, M. Vellekoop, *Sens. Actuators A* 115, 591 (2004).
[21] C.-T. Pan, H. Yang, S.-C. Chen, M.-C. Chou, H.-P. Chou, *J. Micromech. Microeng.* 12, 611 (2002).
[22] K.W. Oh, A. Han, S. Bhansali, C.H. Ahn, *J. Micromech. Microeng.* 12, 187 (2002).
[23] F. Niklaus, H. Andersson, P. Enoksson, G. Stemme, *Sens. Actuators A.* 92, 235 (2001).
[24] Y.-S. Choi, J.-S. Park, H.-D. Park, Y.-H. Song, J.-S. Jung, S.-G. Kang, *Sens. Actuators A* 108, 201 (2003).
[25] X. Zhou, S. Virasawmy, C. Quan, *Microsyst. Technol.* 15, 573 (2009).
[26] Z. Huang, J.C. Sanders, C. Dunsmor, H. Ahmadzadeh, J.P. Landers, *Electrophoresis* 22, 3924 (2001).
[27] S. Schlautmann, G.A.J. Besselink, R.G. Prabhu, R.B.M. Schasfoort, *J. Micromech. Microeng.* 13, S81 (2003).
[28] Y.-J. Pan, R.-J. Yang, *J. Micromech. Microeng.* 16, 2666 (2006).

[29] S. Carroll, M.M. Crain, J.F. Naber, R.S. Keynton, K.M. Walsh, R.P. Baldwin, *Lab Chip* 8, 1564 (2008).
[30] M. Zhang, J. Zhao, L. Gao, *Sens. Actuators A*, 141, 213 (2008).
[31] N.Y. Lee, B.H. Chung, *Langmuir* 25, 3861 (2009).
[32] E.T. Kang, U. Zhang, *Adv. Mater.* 12, 1481 (2000).
[33] W. Dasilva, A. Entenberg, B. Kahn, T. Debies, G.A. Takacs, *J. Adhesion Sci. Technol.* 18, 1465 (2004).
[34] R.R. Rye, A.J. Howard, A.J. Ricco, *Thin Solid Films* 262, 73 (1995).
[35] C.W. Lin, W.C. Hsu, B.J. Hwang, *J. Adhesion Sci. Technol.* 14, 1 (2000).
[36] W.H. Grover, M.G. von Muhlen, S.R. Manalis, *Lab Chip* 8, 913 (2008).
[37] M. Yang, R.L.M. Teeuwen, M. Giesbers, J. Baggerman, A. Arafat, F.A. de Wolf, J.C.M. van Hest, H. Zuilhof, *Langmuir* 24, 7931 (2008).
[38] Z. Grabarek, J. Gergely, *Anal. Biochem.* 185, 131 (1990).
[39] S. Liu, T. Zhu, R. Hu, Z. Liu, *Phys. Chem. Chem. Phys.* 4, 6059 (2002).
[40] N. Crampton, W.A. Bonass, J. Kirkham, N.H. Thomson, *Langmuir* 21, 7884 (2005).
[41] Y.-T. Li, H.-S. Liu, H.-P. Lin, S.-H. Chen, *Electrophoresis* 26, 4743 (2005).
[42] For more detailed information on FluoroEtch: http://www.actontech.com/fluor5.htm
[43] N. Balachander, C.N. Sukeni, *Langmuir* 6, 1621 (1990).
[44] T.R. Lee, R.I. Carey, H.A. Biebuyck, G.M. Whitesides, *Langmuir* 10, 741 (1994).
[45] A. Arafat, M. Giesbers, M. Rosso, E.J.R. Sudhölter, K. Schroën, R.G. White, L. Yang, M.R. Linford, H. Zuilhof, *Langmuir* 23, 6233 (2007).
[46] W.P. Maszara, G. Goetz, A. Caviglia, J.B. McKitterick, *J. Appl. Phys.* 64, (10), 4943 (1988).
[47] J. Bart, A.J. Kolkman, A.J. Oosthoek-de Vries, K. Koch, P.J. Nieuwland, J.W.G. Janssen, P.J.M. van Bentum, K.A.M. Ampt, F.P.J.T. Rutjes, S.S. Wijmenga, J.G. E. Gardeniers and A.P.M. Kentgens, *J. Am. Chem. Soc.* 131 (14) 5014 (2009).

Summary and future perspectives

Summary

The inherent low sensitivity of the NMR spectroscopy analysis technique has been the main drive for ongoing research onto sensitivity enhancement methods. One straightforward route, which is generally applicable, is the decrease of the detection coil while keeping the amount of sample the same. Initially, this research has only focused on micro solenoids closely wrapped around capillaries or micro planar coils patterned on fluidic devices. A short-coming of such systems is their limited spectral resolution, which in most cases does not comply with the state-of-the-art high-resolution NMR standard. In this thesis, the results of a study onto the feasibility of a novel stripline geometry for NMR analysis are discussed.

In **chapter 2**, the concept of stripline-based NMR detectors is introduced. Shortly, the stripline consists of a flat strip positioned in parallel with the static magnetic field. Through this strip an rf-current is fed, resulting in a magnetic rf-field encircling this strip. This field is perpendicular to the static field and can therefore be used for the excitation of spin transitions. Ground planes are applied at both sides of the central strip to homogenize the field. Long uniform structures in parallel with the applied field induce minimal susceptibility distortion, and therefore provide high-resolution spectra. This is in contrast to helices which, because of their perpendicular positioning with respect to the static field, introduce susceptibility broadening.

Apart from resolution advantages, the stripline offers an intrinsic higher sensitivity of a factor $\sqrt{2}$ compared to a solenoid. The sensitivity was verified using a simple prototype probe based on a closed capillary containing 12 nL of ethanol fixed in a PCB-board patterned stripline configuration. With this set-up an LOD of $1.5 \cdot 10^{13}$ spins/$\sqrt{\text{Hz}}$ (25 pmol/$\sqrt{\text{Hz}}$) was found, which is congruent with predictions.

A thorough optimization study in terms of sensitivity, resolution and rf-homogeneity is discussed in **chapter 3**. Optimal dimensional ratios for the length, width and thickness of the 3D stripline structure ($1 < w/d < 1.5$ and $5 < l/w < 10$) were derived using numerical models. Based on the optimized parameters, a simple integrated stripline-based microfluidic chip was realized in silicon substrates. With this chip containing 600 nL of sample, a sensitivity of $2.8 \cdot 10^{14}$ spins/$\sqrt{\text{Hz}}$ (0.47 nmol/$\sqrt{\text{Hz}}$) and a resolution of 0.7 Hz were obtained. This is the highest resolution ever shown on a microfluidic NMR system, and demonstrated the predicted low susceptibility broadening. The rf-homogeneity ($A_{810°}/A_{90°}$) was 76% and was proved

to be suitable for 2D-NMR analysis of glucose. To minimize dielectric losses in the silicon, high resistivity silicon was used, from which the surface was amorphizised to stop conductive surface channels. Nevertheless, the losses in this chip were substantial and lead to a deviation from the predicted sensitivity with a factor of 9. Therefore, it was concluded that, besides silicon, other substrates which have lower losses need to be considered for stripline-based NMR detectors.

As described in **chapter 4**, the in-flow property of the silicon NMR detector was exploited by the monitoring of a chemical reaction *in-situ*. In-flow NMR detectors offer the possibility to obtain kinetic data of chemical reactions on time scales inaccessible by regular NMR. For this purpose, the NMR probe was equipped with a microreactor positioned close to the NMR chip and directly linked via a capillary. The reaction volume was 4.5 µL. Since operating NMR under flow conditions affects the spectral resolution, flow-effects on the linewidth are discussed, and a prediction of the line broadening as a function of the flow rate was presented. From this analysis it was concluded that the linewidth remains below 2.2 Hz for flow rates up to 150 µL/min, which is a very high flow rate for microreactors. The real-time monitoring of the acetylation of benzyl alcohol with acetyl chloride in the presence of DIPEA was demonstrated. These experiments allowed for visualisation of short-term line broadening caused by (de-)protonation of DIPEA which could not be observed in reference spectra obtained in a regular NMR system. Furthermore, the microreactor experiments showed a resonance at 2.41 ppm, which was almost unobservable in the experiments performed in a 5 mm NMR tube. This peak was supposed to be a short-lived DIPEA-acetate complex resonance. These results demonstrated the possibility to track intermediates using fast *in-situ* analysis.

In **chapter 5**, the silicon chip is used for the analysis of a low concentration biofluid: human cerebrospinal fluid (CSF). The measurements in the stripline (600 nL, 9× concentrated) were compared with a reference measurement performed in a standard 5 mm tube (450 µL, non-concentrated). The mass-sensitivity was 3.6 times higher in the stripline probe. Moreover, all the resonance peaks identifiable in the reference spectrum, were also identifiable in the stripline spectrum, demonstrating again the high resolution.

The results obtained with the silicon chip suffered from moderate sensitivity caused by dielectric losses in the substrate and a low filling factor. Therefore, it was aimed for a chip based on a low-loss glass substrate in which the sample was

positioned more efficiently with respect to the central strip. **Chapter 6** discusses the fabrication of a stripline-based chip with an optimized filling factor in D263T borosilicate glass substrates. The device showed a spectral resolution of 2 Hz and an LOD of $2.5 \cdot 10^{14}$ spins/√Hz (0.42 nmol/√Hz). The sensitivity was a factor of 13 lower than the predicted sensitivity, which was again attributed to substrate losses. Apparently, a proper substrate choice is really crucial for stripline-based NMR chips. The selection of a proper substrate which has low losses and is compatible with cleanroom processing is still in progress. Although the sensitivity was rather disappointing, the developed fabrication process is still valid, also for low-loss glasses.

The sensitivity enhancement of microcoils relies on the concentration of the same amount of sample in a smaller coil and therefore it supposes the availability of a method to concentrate the sample. However, for sample volumes below 1 µL, sample concentration using standard laboratory equipment is of limited applicability. **Chapter 7** describes a very simple and cheap microfluidic concentration method, based on the evaporation of water through a hydrophobic porous membrane. A model was proposed with which the concentration rate can be predicted. This model was experimentally verified and found to be very accurate. With a prototype set-up using a 10 cm long hydrophobic porous hollow fiber (polypropylene), a 16 times concentration of phenolred was demonstrated. The concentration factor was detected using photometry. Until now, this technique is not coupled to NMR.

During the design of the silicon chip, a novel wafer bonding method was developed. In **chapter 8**, this method is described and demonstrated with (microfluidic) experiments. The method is based on chemically activated Fluorinated Ethylene Propylene (FEP) films as an intermediate between chemically activated substrates. Surfaces of silicon and glass substrates were modified with Aminoproyltri-ethoxysilane (APTES) bearing amine ($-NH_2$) terminal groups, while FEP foil surfaces were treated to form carboxyl groups and subsequently activated by means of EDC-NHS chemistry. The activation of silicon and glass substrates as well as the FEP foil was studied by contact angle measurements and X-ray photoelectron spectrometry (XPS). Bonding was successfully realized by simply pressing the two amine-terminated substrate surfaces together with NHS ester-terminated FEP foil in between. An appealing advantage of this technique is that it can be performed at room temperature, without the need for high electric potentials.

An average tensile strength of 5.9 MPa and 5.2 MPa was achieved for silicon-silicon and glass-glass bonds, respectively. The average fluidic pressure that could be operated was 10.2 bar. Control tests with stacks using non-treated foils could withstand a maximal pressure of 1.9 bar, which underlines the effectiveness of the activation. It was demonstrated that the chips could handle mild organic solvents at elevated pressures without leakage problems. Only for an extremely oxidizing piranha solution leakage at higher pressures was observed.

Future perspectives

Microfluidic integration of sample treatment

As stated several times in this thesis, handling of small samples is simplified using a microfluidic set-up. Using the microfabrication toolbox available nowadays, a completely integrated platform in one chip which can handle and detect raw samples without any preparative laboratory work is within reach. For example, cells and proteins can be separated from the sample by means of an integrated filter,[1,2] whereas membranes can be used for 'on-chip' concentrating of the sample (see Chapter 7). Furthermore, plug-flow[3] can be utilized to transport the small sample to the sensitive area of the probe. Since the concepts for many sample treatment procedures are already available in literature, the integration is mainly a matter of design implementation. Combining these functions in one device would result in a versatile platform for the analysis of mass-limited samples.

On-chip DNP

Dynamic Nuclear Polarization (DNP) is a double resonance technique that may help to overcome sensitivity problems in NMR measurements. The aim of DNP is to transfer the much larger electronic polarization of unpaired electrons to the abundant nuclei in the sample, using microwave irradiation. The most common procedure is that radicals are mixed with the sample which is subsequently frozen. Microwave irradiation is applied for several hours to pre-polarize the spin system, after which the sample is rapidly defrosted using a hot solvent and measured. With this method one can achieve impressive signal enhancements of 4 orders of magnitude.[4] Despite these impressive numbers, there are various issues that require further study and optimization. First, the low temperature polarization is a slow process (which often requires several hours) and the NMR experiment is necessarily limited to a single or a few scans within the T_1 time frame of the nuclei. Second, to achieve a proper resolution, the concentration of radicals must be decreased before

recording the FID. This dilution reduces the effective signal enhancement. Third, because of this dissolution, a sample can only be used once, as well as the (costly) radicals.

The latter two issues can be greatly improved when DNP is implemented in a dedicated microfluidic set-up consisting of a polarization area and a NMR detection area. In the polarization area, radicals (*e.g.* tetramethylpypiridine-1-oxyl (TEMPO))[5] can be immobilized in the fluidic channel. The (room temperature) sample is polarized in this area and subsequently transported to the detection area. Utilizing plug-flow and designing the detection area close to the polarization area, this transport can be performed in a very short time. Since the radicals are immobilized, they will not be transported to the detection area, which eliminates the problem associated with line-broadening caused by radicals present in the polarized sample. This also means that dissolution is not necessary so that the initial concentration can be maintained.

In a microfluidic set-up freezing of the sample is hardly implemented (although not impossible) which means that the advantage of the more favourable low temperature Boltzmann factors is not exploited. On the other hand, this means that polarization can be performed in a much shorter time (a few seconds). Moreover, in a microfluidic set-up one can consecutively shuttle the sample from the polarization area to the detection area and back which is not possible in the dissolution method since the sample is strongly diluted after one scan. A first step towards such a system was recently demonstrated by Annino et al.[6] A project, focussed on this microfluidic DNP implementation is recently started.

Table-top NMR

For high-resolution NMR, the B_0-field must be homogeneous (*i.e.* with a deviation in the order of parts per billion) over the whole sample volume. In the case of conventional 5 mm tubes the volume corresponds to a length of approximately 5 cm (z-axis) and a diameter of 5 mm. This sets very high demands to the design of the magnet, and as a result the used magnets are very large and expensive. For the microfluidic NMR devices presented in this thesis, the demands are much lower since the sample volume (especially the diameter) is much smaller. For example, in the case of the glass-based chip discussed in chapter 6, the B_0-field must be homogeneous over a volume with a length of 12 mm (length of the constriction and taperings) and a diameter of 0.5 mm. Clearly, a magnet optimized for such a volume can be substantially decreased in size without any compromise in the final resolution, especially when designed with a very narrow bore.

In organic chemistry, NMR is widely used as a fast and non-destructive method for the identification of synthesized compounds. Such compounds are usually less complex than for example body fluids, and therefore exhibit relatively simple spectra. Moreover, the concentration is generally high for these experiments. Since the necessary B_0-homogeneity for stripline probes is low compared to a conventional probe, and sensitivity is a minor issue because of the high concentrated compounds, a much smaller magnet producing a lower field and lower homogeneity can still be convenient for general purpose NMR in organic chemistry laboratory. Even the use of permanent magnets optimized for NMR applications[7] should be considered for these purposes. In combination with a low power amplifier, one can build a cheap NMR setup which is suitable for simple NMR experiments.

References

[1] H.M. Ji, V. Samper, Y. Chen, C.K. Heng, T.M. Lim, L. Yobas, *Biom. Microdev.* 10 (2), 251 (2007).
[2] T.A. Crowley, V. Pizziconi, *Lab Chip* 5 (9), 922 (2005).
[3] M. Prakash, N. Gershenfeld, *Science* 315(5813), 832 (2007).
[4] J.H. Ardenkjaer-Larsen, B. Fridlund, A. Gram, G. Hansson, L. Hansson, M.H. Lerche, R. Servin, M. Thaning, K. Golman, *Proc. Natl. Acad. Sci. USA* 100, 10158 (2003).
[5] E.R. McCarney, S. Han, *J. Magn. Reson.* 190(2), 307 (2008).
[6] G. Annino J.A. Villanueva-Garibay, P.J.M. van Bentum, A.A.K. Klaassen, A.P.M. Kentgens, *Applied Magn. Reson.* (special issue), accepted (2009).
[7] E. Danieli, J. Mauler, J. Perlo, B. Blümich, F. Casanova, *J. Magn. Reson.* 198, 80 (2009).

Appendix A. Detailed process-flow for silicon chip fabrication

Wafer selection and cleaning (all wafers)

Process	Process parameters
Wafer selection	• Supplier: Topsil • Diameter and finish: 100 mm, double side polished • Thickness: 0.525 mm • Resistivity: >10.000 ohm.cm (n-type)
Standard cleaning	**CMOS wet-bench** • 1% HF-dip till wafers are hydrofobe • Quick dump rinse • HNO_3 (100%) beaker 1: 5 min • HNO_3 (100%) beaker 2: 5 min • Quick Dump Rinse <0.1 µS • Fuming HNO_3 (69%, 95°C): 10 min • Quick dump rinse <0.1 µS • Spin drying

Channel etching (top wafer front side)

Process	Process parameters
Litho – resist spinning	**CR112B / Headway Spinner** • Primer: HMDS • 60 sec @ 4000 rpm • Resist: Olin 907-35 • 60 sec @ 4000 rpm • Prebake 90 sec @ 95 °C *On the front side*
Litho - Alignment & Exposure	**CR117B / EVG 20 Mask Aligner** **Mask: Channels (1)** • Lamp intensity= 12 mW/cm^2 • Exposure Time: 9 sec
Litho - Development	**CR112B / Wet-Bench 11** • Developer: OPD4262 • Time: 30 sec in beaker 1 • Time: 15-30 sec in beaker 2 • Quick dump rinse <0.1 µS • Spin drying • Postbake: 5 min @ 95 °C

Channel etching	**CR125c/Adixen SE** • Deep reactive ion etching (DRIE) • Bosch process (uniform) • Temp: -10 °C • Depth: 300 µm • Etch rate: ~ 20 µm/min (depends on loading) • Time: ~ 15 min *Check etch rate after 5 min etching with Dektak scan (see next step)*
Surface profile measurement	**CR118B / Veeco Dektak 8**
Resist removal	• Flush with acetone

Holes etching (top wafer bottom side)

Process	Process parameters
Protection	• Apply dicing foil on channel side to avoid scratches
Litho – resist spinning	**CR112B / Headway Spinner** • Primer: HMDS • 60 sec @ 4000 rpm • Resist: Olin 907-35 • 60 sec @ 4000 rpm • Prebake 90 sec @ 95 °C *On the backside*
Litho - Alignment & Exposure	**CR117B / EVG 20 Mask Aligner** **Mask: Holes (2)** • Lamp intensity= 12 mW/cm^2 • Bottom alignment (use crosshairs) • Exposure Time: 9 sec
Litho - Development	**CR112B / Wet-Bench 11** • Developer: OPD4262 • Time: 30 sec in beaker 1 • Time: 15-30 sec in beaker 2 • Quick dump rinse <0.1 µS • Spin drying • Postbake: 5 min @ 95 °C

Holes etching	**CR125c/Adixen SE** • Deep reactive ion etching (DRIE) • Bosch process (uniform) • Temp: -10 °C • Depth: through all (225 µm) • Etch rate: ~ 20 µm/min (depends on loading) • Time: ~ 12 min *Check etch rate after 5 min etching*
Resist stripping	**CR125A / Tepla 300 (Metal free)** • O_2 plasma 500 W • Time: 30 min
Residual Fluorocarbon cracking	**CR112B / Furnace B2 (Wet oxidation tube)** • 30 min in standby mode • Temp: 800 °C
Cleaning	Same process as described in other section: • Wafer selection and cleaning

Surface channel passivation (all wafers)

Process	Process parameters
Amorphous Si deposition	**CR125C / Tempress LPCVD (tube F2)** • Recipe: Amorfsi2 • SiH_4 flow: 25 sccm • Temp: 550 °C • Pressure: 750 mTorr (1 mbar) • Thickness: 500 nm • Deposition rate: 2.1 nm/min • Time: 3 hr 42 min
SiO_2 deposition	**CR102A / OXFORD Plasmalab 80$^+$ (PECVD)** • Recipe: Jacob_oxide • SiH_4 in N_2: 425 sccm, N_2O: 710 sccm • Temp: 300 °C • Pressure: 32 APC (1000 mTorr) • Power: 20 Watt HF • Thickness: 500 nm • Deposition rate: 62.5 nm/min • Time: 8 min

Electroplating Stripline (Bottom wafer front side)

Process	Parameters
Protection	• Apply dicing foil on backside to avoid scratches
Seed layer deposition	**CR106A / Sputterke** *Adhesion layer* • Select Ti Target • Ar flow: 80 sccm • Base pressure: 1.0e-6 mbar • Sputter pressure: 6.5e-3 mbar • Power: 200 W • Deposition rate = 8 nm/min • Thickness: 16 nm • Time: 2 min *Seed layer* • Switch Cu Target • Ar flow: 80 sccm • Base pressure: 1.0e-6 mbar • Sputter pressure: 6.5e-3 mbar • Power: 200 W • Deposition rate = 20 nm/min • Thickness: 200 nm • Time: 10 min
Litho – Resist Spinning	**CR112B / Headway Spinner** • Dehydration bake, 10 min @ 120 ºC • Cooldown • No primer • Resist: Clariant AZ9260 (positive) • 60 sec @ 2400 rpm (10 µm) • Bake 80 sec @ 110 °C • 60 sec @ 2100 rpm (14 µm) • Bake 160 sec @ 110 °C • Relax > 2 hour (better: overnight)
Litho - Alignment & Exposure	**CR117B / EVG 20 Mask Aligner** **Mask: Stripline (3)** • Lamp intensity= 12 mW/cm^2 Interval exposure:

	• Exposure time (1 cycle): 12.5 sec • Delay time: 5 sec • 10 cycles (Total exposure time: 125 sec)
Litho - Development	**CR112B / Wet-Bench 11** • Developer: OPD4262 • Time: 7 min in beaker 1 • Time: 15-30 sec in beaker 2 • Quick Dump Rinse <0.1 µS • Spin drying
Surface profile measurement	**CR118B / Veeco Dektak 8** • Note the measured thickness of the resist
Electroplating (Cu)	**Electroplate Bath ($CuSO_4$)** • Current density 1.0 A/dm^2 • Plate rate: 0.22 µm/min • Thickness: 10 µm • Time: 45 min • Electrolyte pump on maximal speed *Check plate rate after 20 min with a Dektak scan (see previous step)*
Remove dicing foil	• By hand
Strip resist with acetone	**CR116B / Wet-Bench 2** • Use metal beaker • Acetone VLSI • Ultrasonic bath • Time: 5 min • Quick dump rinse <0.1 µS • Spin drying
Seed layer removal	**CR106A /Ion Beam etcher** • Background pressure: 1e-7 mbar • Ar flow: 300 sccm • Etch pressure: ~ 1e-3 mbar • Beam current: 35 mA • Etching rate: ~3.5 nm/min • Time: ~ 60 min • Depth: through copper and titanium

Stack bonding

Process	Process parameters
Chemical substrate and FEP foil activation	See chapter 8
Stack alignment	**CR117B / EVG 20 Mask Aligner** • Program: anodic bond • Load bottom substrate • Be sure the striplines are facing *down* • Focus on the aligning marks and set crosshairs • Insert flags • Load top substrate • Be sure the channels are *up* • Align the crosshairs on the aligning marks located on the backside of the channel wafer • Clamp the stack gently (both together)
Pre-bonding	**CR117B / EVG 501 Anodic bonder** • Temp: 20 °C • Load: 8 kN • Time: 5 min
Bond finishing	**CR106A / Hydraulic press (Carver 3851 CE)** • Position stack between plates in center • Load: 0.4 metric tons per cm^2 • Temp: 20 °C • Time: 15 hr

Electroplating top shielding (holes side)

Process	Process parameters
Protection	• Apply dicing foil on backside to avoid scratches
Seed layer deposition	Same process as: - Electroplating Stripline (Bottom wafer front side)
Lithography AZ9260	Same process as: - Electroplating Stripline (Bottom wafer front side) **Mask: Top shielding (4)**
Surface profile measurement	Same process as: - Electroplating Stripline (Bottom wafer front side)
Electroplating (Cu)	Same process as:

	- Electroplating Stripline (Bottom wafer front side)
Remove dicing foil	• by hand
Strip resist with acetone	Same process as: - Electroplating Stripline (Bottom wafer front side)

Electroplating bottom shielding

Process	Process parameters
Protection	• Apply dicing foil on the plated top shielding, to avoid scratches
Seed layer deposition	Same process as: - Electroplating Stripline (Bottom wafer front side)
Lithography AZ9260	Same process as: - Electroplating Stripline (Bottom wafer front side) **Mask: Bottom shielding (5)**
Surface profile measurement	Same process as: - Electroplating Stripline (Bottom wafer front side)
Electroplating (Cu)	Same process as: - Electroplating Stripline (Bottom wafer front side)
Remove dicing foil	- by hand
Strip resist with acetone	Same process as: - Electroplating Stripline (Bottom wafer front side)
Seed layer removal	**CR106A /Ion Beam etcher** • Background pressure: 1e-7 mbar • Ar flow: 300 sccm • Etch pressure: ~ 1e-3 mbar • Beam current: 35 mA • Etching rate: ~3.5 nm/min • Time: ~ 60 min • Depth: through copper and titanium *Repeat this step for the other side of the stack*

Dicing

Process	Parameters
Protection	**CR128C / Laminator** • Laminate both sides • Bottom shielding side should be up during dicing, for this side contains the dicing help lines • Laminate this side with thin UV-sensitive foil • Use laminator to apply standard dicing foil on the top shielding side
Dicing	**CR128C / Disco DAD dicing saw** • Blade type NC1050 • Blade thickness: 50 µm • Working height: 2 mm • Speed: 3 mm/s • Stack thickness: ~ 1100 µm

Appendix B. Detailed process-flow for glass chip fabrication

Wafer selection and cleaning

Process	Process parameters
Wafer selection	• Supplier: Schott • D263T borosilicate glass • Diameter: 100 mm • Thickness: 0.150 mm • Double side polished
Standard cleaning	**CR116B / Wet-Bench** • HNO_3 (100%) beaker 1: 5min • HNO_3 (100%) beaker 2: 5min • Cascade Rinse <0.1 µS • Spin drying

Alignment marks etching (all wafers on one side)

Process	Parameters
Cr Sputtering	**CR106A / Sputterke** • Select Cr target • Ar flow: 80 sccm • Base pressure: 1.0e-6 mbar • Sputter pressure: 6.5e-3 mbar • Power: 200 W • Deposition rate = 10 nm/min. • Time: 1 min • Thickness: 10 nm *Remain vacuum for next step*
Au Sputtering	**CR106A / Sputterke** • Switch to Au target • Ar flow: 80 sccm • Sputter pressure: 6.5e-3 mbar • Power: 200 W • Deposition rate = 30-35 nm/min • Time: 4 min • Thickness: 120 – 140 nm
Litho – resist spinning	**CR112B / Headway Spinner** • Primer: HMDS

	• 60 sec @ 4000 rpm • Resist: Olin 907-17 • 60 sec @ 4000 rpm • Prebake 90 sec @ 95°C *On the non-metalized side*
Litho - Alignment & Exposure	**CR117B / EVG 20 Mask Aligner** **Mask: Channels (1)** • Lamp intensity= 12 mW/cm^2 • Exposure Time: 4.5 sec *Cover main structure with plastic plate. Only aligning marks should be visible*
Litho - Development	**CR112B / Wet-Bench 11** • Developer: OPD4262 • Time: 30 sec in beaker 1 • Time: 15-30 sec in beaker 2 • Cascade rinse <0.1 µS • Spin drying
Litho - Hardbake	**CR112B / Hotplate** • Temp: 120 °C • Time: ~10 min
Glass Etching in BHF	**CR116B / Wet-Bench** • Buffered HF (BHF) • NH_4F/HF (1:7) VLSI: Merck 101171.2500 • Etchrate: ~ 25 nm/min • Depth: 500 nm • Time: ~ 20 min • Cascade rinse <0.1 µS • Spin drying
Strip resist with acetone	**CR116B / Wet-Bench** • Use metal beaker • Acetone VLSI • Ultrasonic bath • Time: 5 min • Cascade rinse <0.1 µS • Spin drying

Channel etching

Process	Parameters
Cr Sputtering	Same process as described in other section: - Alignment marks etching *Only on the etched side*
Au Sputtering	Same process as described in other section: - Alignment marks etching *Only on the etched side*
Backside coverage	**CR112B / Headway Spinner** • Primer: HMDS • 60 sec @ 4000 rpm • Resist: Olin 907-35 • 60 sec @ 4000 rpm • Prebake 90 sec @ 95°C *To avoid pinholes in the alignment marks side during channel etching*
Litho – Resist Spinning	**CR112B / Headway Spinner** • Primer: HMDS • 60 sec @ 4000 rpm • Resist: Olin 907-17 • 60 sec @ 4000 rpm • Prebake 90 sec @ 95°C *On the non-protected metal side*
Litho - Alignment & Exposure	**CR117B / EVG 20 Mask Aligner** **Mask: Channels (1)** • Lamp intensity= 12 mW/cm^2 • Exposure Time: 4.5 sec • Bottom alignment • Frontside exposure *Cover aligning marks on mask before loading mask with non-transparent stickers. (this does not influence the aligning, since bottom alignment is used)*
Litho - Development	**CR112B / Wet-Bench 11** Developer: OPD4262 • After Exposure Bake (120°C): 60 sec Development:

	• Time: 30 sec in beaker 1 • Time: 15-30 sec in beaker 2 • Cascade Rinse <0.1 µS • Spin drying
Litho - Hardbake	**CR112B / Hotplate** • Temp: 120 °C • Time: 30 min
Ozone anneal of resist (to improve wetting)	**CR116B-1 / UV PRS-100** • Time: 300 sec *To improve wetting during etching of Chromium and Gold layers*
Surface profile measurement	**CR118B / Veeco Dektak 8** • Note the measured thickness of the resist
Au- Etching (Wet)	**CR116B / Wet-Bench 2** • KI (pa): MERCK 105043 • I_2: MERCK 144761 • KI:I_2:DI = (4:1:40) • Temp: 25 °C • Thickness: 120 – 140 nm • Time: 45 – 50 sec • Etchrate: 600 nm/min • Cascade Rinse <0.1 µS
Cr-Etching (Wet)	**CR116B / Wet-Bench 2** Chromium etch LSI Selectipur: MERCK 111547.2500 • Thickness: 10 nm • Time: 15 – 20 sec • Etchrate: 100 nm/min • Cascade Rinse <0.1 µS
Glass Etching in 10% HF	**CR116B / Wet-Bench** • HF (10% v/v) in DI • VLSI: MERCK 100373.2500 • Depth: 100 µm • Time: ~ 100-125 min • Etchrate: ~ 1 µm/min but strongly depends on loading and age of etchant • Cascade Rinse <0.1 µS

	• Spin drying *Check etched depth after 30 min with Dektak scan (see previous step)*
Strip resist	**CR116B / Wet-Bench** • HNO_3 (100%) • Selectipur: Merck 100453 • Glass beaker: HNO_3 (100%) • Time: 5 min • Cascade Rinse <0.1 µS
Au- Etching (Wet)	Same process described earlier in this section. • Remove al Au.
Cr-Etching (Wet)	Same process described earlier in this section. • Remove al Cr.
Cleaning Borofloat Glass	Same process as described in other section: - Wafer selection and cleaning
Surface profile measurement	**CR118B / Veeco Dektak 8**

Bonding

Process	Parameters
Pre-treatment	**CR116B / Wet-Bench** • HNO_3 (100%) • 15 min • Cascade Rinse <0.1 µS *Don't dry the wafers*
Cleaning Borofloat wafers by KOH - standard	**CR102B / KOH** • KOH: MERCK 105019.500 • KOH:DI = (1:3) • 25 wt% KOH: 500 g KOH pellets in 1500 ml DI water • Temp: 75 °C • Stirrer on • Time: 1 min
Sonification/Cleaning	**CR116B / Wet-Bench 2** • Ultrasonic bath • Glass beaker with water

	• Low energy setting (50%) • Time: 15 min • Cascade Rinse <0.1 µS • Spin drying *To remove particles which possibly remained after KOH etching*
Aligning	**CR117B / EVG 20 Mask Aligner** • Pre-align with flags in between • When aligned properly: remove flags • Release chuck from aligner
Pre-bonding	• Release stack from bond chuck • Finalize prebond by means of pressing gently with a 'soft' tweezer on the remaining airbubbles
Annealing	**Laboratory floor 10 (BIOS)** • Heraeus Furnace • Place waferstacks on Si-wafer (carrier) • 8 hr ramp-up to 600 °C • 1 hr stable @ 600 °C • 8 hr ramp-down to room temperature

Electroplating Stripline

Process	Parameters
Seed layer deposition	**CR106A / Sputterke** *Adhesion layer* • Select Ti Target • Ar flow: 80 sccm • Base pressure: 1.0e-6 mbar • Sputter pressure: 6.5e-3 mbar • Power: 200 W • Deposition rate = 8 nm/min • Thickness: 16 nm • Time: 2 min *Seed layer* • Switch Cu Target • Ar flow: 80 sccm

	• Sputter pressure: 6.5e-3 mbar • Power: 200 W • Deposition rate = 20 nm/min • Thickness: 200 nm • Time: 10 min
Litho – Resist Spinning	**CR112B / Headway Spinner** • Dehydration bake, 10 min @ 120 °C • Cooldown • No primer • Resist: Clariant AZ9260 (positive) • 60 sec @ 2400 rpm (10 µm) • Bake 80 sec @ 110 °C • 60 sec @ 2100 rpm (14 µm) • Bake 160 sec @ 110 °C • Relax > 2 hour (better: overnight)
Litho - Alignment & Exposure	**CR117B / EVG 20 Mask Aligner** **Mask: Stripline (2)** • Lamp intensity= 12 mW/cm^2 Interval exposure • Exposure time (1 cycle): 12.5 sec • Delay time: 5 sec • 10 cycles (Total exposure time: 125 sec)
Litho - Development	**CR112B / Wet-Bench 11** • Developer: OPD4262 • Time: 7 min in beaker 1 • Time: 15-30 sec in beaker 2 • Cascade Rinse <0.1 µS • Spin drying
Surface profile measurement	**CR118B / Veeco Dektak 8** • Note the measured thickness of the resist
Electroplating (Cu)	**Electroplate Bath ($CuSO_4$)** • current density 1.0 A/dm^2 • Plate rate: 0.22 µm/min • Thickness: 10 µm • Time: 45 min • Electrolyte pump on maximal speed

	Check plate rate after 20 min with a Dektak scan (see previous step)
Strip resist with acetone	Same process as: - Alignment marks etching

Electroplating shielding

Process	Process parameters
Protection	• Apply dicing foil on the plated striplines, to avoid scratches
Seed layer deposition	Same process as described in other section: - Electroplating Stripline
Lithography AZ9260	Same process as described in other section: - Electroplating Stripline **Mask: shielding (3)**
Surface profile measurement	Same process as: - Electroplating Stripline (Bottom wafer front side)
Electroplating (Cu)	Same process as described in other section: - Electroplating Stripline
Remove dicing foil	• By hand
Strip resist with acetone	Same process as: - Alignment marks etching
Seed layer removal	**CR106A /Ion Beam etcher** • Background pressure: 1e-7 mbar • Ar flow: 300 sccm • Etch pressure: ~ 1e-3 mbar • Beam current: 35 mA • Etching rate: ~3.5 nm/min • Time: ~ 60 min • Depth: through copper and titanium *Repeat this step for the other side of the stack*

Dicing

Process	Parameters
Protection	• Shielding side should be up during dicing, for this side contains the dicing help lines • Laminate only stripline side • Use laminator to apply standard dicing foil on the top shielding side
Dicing	**Disco Automated Dicing Saw** • Blade type TC300 • Blade thickness: 300µm • Working height: 2 mm • Speed: 4 mm/s • Stack thickness: ~ 300 µm

Nederlandse samenvatting

De inherent lage gevoeligheid van de NMR spectroscopie analyse techniek is de voornaamste drijfveer geweest voor voortdurend onderzoek naar methoden om de gevoeligheid te verhogen. Een eenvoudige en algemeen toepasbare route is het verkleinen van de detectiespoel waarbij de hoeveelheid sample gelijk blijft. In beginsel heeft dit onderzoek zich toegespitst op micro-solenoides die strak om een capillair gewikkeld waren, of planaire spoelen gepatterneerd op vlakke substraten waarin kleine vloeistofkanalen gedefinieerd zijn. Een nadeel van dergelijke systemen is dat de spectrale resolutie laag is, waardoor ze niet kunnen concurreren met de hedendaagse hoge-resolutie standaard. In dit proefschrift worden de resultaten behandeld van een studie naar de haalbaarheid en bruikbaarheid van een nieuwe stripline geometrie voor NMR analyse.

In **hoofdstuk 2** wordt het concept van NMR detectors gebaseerd op striplines geïntroduceerd. Een stripline bestaat uit een platte strip die parallel met het statische veld is gepositioneerd. Door deze strip wordt een radiofrequente (rf) stroom geleid wat resulteert in een magnetisch rf-veld rond de strip. Dit veld staat loodrecht op het statische veld en kan daarom gebruikt worden voor het exciteren van spin-transities. Aan beide zijden van de centrale strip zijn metalen grondvlakken aangebracht die het rf-veld homogeniseren. Een lange uniforme structuur parallel met het aangelegde veld induceert minimale susceptibiliteitsverstoring en verschaft daardoor hoge-resolutie spectra. Dit in tegenstelling tot helix-vormige structuren, die vanwege het feit dat ze loodrecht op het aangelegde veld worden gepositioneerd susceptibiliteitsversbreding induceren.

Afgezien van voordelen met betrekking tot resolutie levert de stripline ook een gevoeligheid die $\sqrt{2}$ keer zo hoog is als die van een solenoïde. De gevoeligheid werd geverifieerd met een eenvoudige prototype probe, waarin een stripline was gedefinieerd in een Printed Circuit Board (PCB) substraat. In deze stripline was een gesloten capillair geïmplementeerd, dat fungeerde als sample-houder. Dit capillair bevatte 12 nL ethanol. Met deze set-up werd een Limit of Detection (LOD) van $1.5 \cdot 10^{13}$ spins/$\sqrt{\text{Hz}}$ (25 pmol/$\sqrt{\text{Hz}}$) gemeten, een waarde die congrueert met de voorspellende berekeningen.

Een grondige optimalisatie in termen van gevoeligheid, resolutie en rf-homogeniteit is behandeld in **hoofdstuk 3**. Met behulp van numerieke modellen zijn

optimale dimensionale verhoudingen voor de lengte, breedte en dikte van de 3-dimensionale stripline structuur berekend ($1 < w/d < 1.5$ and $5 < l/w < 10$).

Een eenvoudige stripline chip met een geïntegreerd microfluïdisch kanaal werd gerealiseerd in silicium substraten. Daarbij werd gebruik gemaakt van de geoptimaliseerde parameters. Deze chip, die een sample volume van 600 nL had, leverde een gevoeligheid van $2.8 \cdot 10^{14}$ spins/√Hz (0.47 nmol/√Hz) en een resolutie van 0.7 Hz. Dit is de hoogste resolutie ooit getoond op een microfluïdisch NMR systeem en demonstreert de voorspelde minimale susceptibiliteitsverbreding. De rf-homogeniteit ($A_{810°}/A_{90°}$) was 76% en bleek hoog genoeg voor een 2D NMR-analyse van glucose. Om de diëlektrische verliezen van silicium te beperken, werd gebruik gemaakt van hoog-ohmig silicium. Teneinde elektrisch geleidende oppervlakte-kanalen te minimaliseren werd het oppervlak werd geamorfiseerd. Ondanks deze maatregel bleken de verliezen in deze chip substantieel, zodanig dat de actuele gevoeligheid met een factor 9 verschilde van de voorspelde waarde, uitgaande van een verliesvrij substraat. Daarom werd geconcludeerd dat afgezien van silicium ook andere substraten met lagere diëlektrische verliezen moeten worden onderzocht voor gebruik in stripline-gebaseerde NMR detectors.

In **hoofdstuk 4** wordt beschreven hoe de in-flow eigenschap (dat wil zeggen dat er tijdens metingen vloeistofdoorstroming kan plaatsvinden) nuttig gebruikt kan worden voor het *in-situ* volgen van chemische reacties. In-flow NMR detectors verschaffen de mogelijkheid om kinetische data van chemische reacties te verkrijgen op tijdschalen die ontoegankelijk zijn voor standaard NMR. Voor dit doel werd de probe uitgerust met een microreactor die dichtbij de NMR chip was geplaatst en verbonden via een capillair. Het reactie volume was 4.5 µL. Hoe vloeistofstroming van invloed is op de spectrale resolutie wordt in dit hoofdstuk behandeld. Een berekening van de lijnbreedte als functie van de stromingssnelheid werd gepresenteerd waaruit geconcludeerd kon worden dat de lijnbreedte niet hoger dan 2.2 Hz is voor stromingssnelheden tot 150 µL/min, een zeer hoge stroomsnelheid voor microreactoren. Als demonstratie werd de acetyleringsreactie van benzyl alcohol met acetylchloride met DIPEA als een katalysator *real-time* gevolgd. Dit experiment gaf de mogelijkheid tot het visualiseren van tijdelijke lijnverbreding veroorzaakt door (de-)protonatie van DIPEA. Dit kon niet vastgesteld worden in een standaard NMR systeem. De experimenten in de microreactor leverden een resonantie op bij 2.41 ppm die bijna niet gezien werd in het referentie spectrum. Deze piek werd verondersteld een kort-bestaand DIPEA-acetaat complex te zijn.

Deze resultaten toonden aan dat het mogelijk is om intermediairen te traceren met gebruikmaking van snelle *in-situ* analyse.

Hoofdstuk 5 beschrijft het gebruik van de silicium chip voor de analyse van een laaggeconcentreerde biologische vloeistof: menselijke hersenvloeistof (CSF). Metingen in de stripline chip (600 nL, 9× geconcentreerd) werden vergeleken met referentiemetingen in een standaard 5 mm NMR buis (450 µL, ongeconcentreerd). De massagevoeligheid was 3.6 keer hoger in de stripline probe. Alle pieken die in het referentiespectrum konden worden geïdentificeerd, bleken ook identificeerbaar in de stripline spectra, wat opnieuw de hoge-resolutie eigenschap bevestigde.

De silicium stripline chip vertoonde een matige gevoeligheid als gevolg van de diëlektrische verliezen en een lage vulfactor. Daarom werd als doel gesteld een chip te ontwerpen op een glas-substraat met minder verliezen, waarin tevens het sample efficiënter gepositioneerd werd ten opzichte van de centrale strip. **Hoofdstuk 6** beschrijft de fabricage van een stripline chip met een geoptimaliseerde vulfactor in D263T boorsilicaatglas substraten. Deze chip leverde een spectrale resolutie van 2 Hz en een LOD van $2.5 \cdot 10^{14}$ spins/√Hz (0.42 nmol/√Hz). De gevoeligheid was een factor 13 lager dan voorspeld wat opnieuw veroorzaakt werd door substraat verliezen. Kennelijk is een goede substraatkeuze dé cruciale factor voor stripline gebaseerde NMR chips. De selectie van een passend substraat met lage verliezen dat ook compatibel is met gestandaardiseerde cleanroom processen is nog niet voltooid. Hoewel de gevoeligheid onvoldoende was, blijft het ontwikkelde fabricage proces valide, ook voor substraten met lage verliezen.

De verbeterde gevoeligheid van microspoelen geldt alleen als het mogelijk is dezelfde hoeveelheid sample te concentreren in een kleinere spoel. Echter, het concentreren van sample volumes lager dan 1 µL met behulp van standaard laboratorium apparatuur is niet evident. **Hoofdstuk 7** beschrijft een zeer eenvoudige en goedkope microfluïdische concentratie methode, gebaseerd op de verdamping van water door een hydrofoob poreus membraan. Een model werd opgesteld waarmee de concentratiefactor kon worden voorspeld. Dit model werd experimenteel geverifieerd en zeer accuraat bevonden. Met een prototype set-up waarbij gebruik werd gemaakt van een 10 cm lange hydrofobe poreuze holle fiber (polypropyleen) werd een 16-voudige concentratie van fenolrood gedemonstreerd. De concentratiefactor werd fotometrisch gedetecteerd. De integratie met NMR is tot dusverre nog niet gerealiseerd.

Tijdens het ontwerpen van de silicium chip is een nieuwe wafer bonding methode ontwikkeld. In **hoofdstuk 8** wordt deze methode beschreven en gedemonstreerd aan de hand van (microfluïdische) experimenten. De methode is gebaseerd op chemisch geactiveerde Fluorinated Ethylene Propylene (FEP) films als een intermediaire laag tussen eveneens chemisch gemodificeerde substraten. De silicium en glas substraten werden geactiveerd met Aminopropyltri-ethoxysilane (APTES) met een amine ($-NH_2$) eindgroep, en de FEP folies werden zodanig behandeld dat carboxyl groepen gevormd werden teneinde EDC-NHS chemie te kunnen uitvoeren. De activering van de silicium en glas substraten alsmede de FEP folies werd bestudeerd met behulp van contacthoekmetingen en X-ray photoelectron spectroscopy (XPS). Een stabiele wafer bond werd eenvoudig gerealiseerd door twee amine-getermineerde substraten met daartussen een tweezijdig NHS-ester getermineerde FEP folie op elkaar te klemmen. Een interessante en aantrekkelijke eigenschap van deze techniek is dat deze uitvoerbaar is op kamertemperatuur en hoge elektrische potentialen onnodig zijn. Een gemiddelde treksterkte van 5.9 MPa en 5.2 MPa werden bereikt voor respectievelijk silicium-silicium en glas-glas bonds. De gemiddelde fluïdische druk die kon worden bereikt, was 10.2 bar. Controle experimenten met wafers die gebond waren zonder gebruikmaking van oppervlakte behandelingen toonden een maximale fluïdische druk van 1.9 bar waarmee de effectiviteit van de activatering werd bevestigd. De chips werkten probleemloos met mild-organische oplosmiddelen bij verhoogde druk; geen lekkage werd geobserveerd. Allen bij een extreem zure (oxiderende) piranha oplossing werd lekkage bij hogere druk waargenomen.

List of Publications and presentations

Publications

P.J.M. van Bentum, J.W.G. Janssen, A.P.M. Kentgens, J. Bart, J.G.E. Gardeniers, 'Stripline probes for NMR' *J. Magn. Reson.* 189, 104 (2007).

A.P.M. Kentgens, J. Bart, P.J.M. van Bentum, A. Brinkmann, E.R.H. van Eck, J.G.E. Gardeniers, J.W.G. Janssen, P. Knijn, S. Vasa, M.H.W. Verkuijlen, 'High-resolution liquid- and solid-state nuclear magnetic resonance of nanoliter sample volumes using microcoil detectors' *J. Chem. Phys.* 128, 1 (2008).

J. Bart and J.G.E. Gardeniers, 'On-line monitoring of reaction kinetics in microreactors using MS and micro NMR' *Micro Process Engineering: A Comprehensive Handbook*, Volume 3, V. Hessel, J.C. Schouten (eds.), Wiley-VCH, 135 (2009).

J. Bart, A.J. Kolkman, A.J. Oosthoek-de Vries, K. Koch, P.J. Nieuwland, J.W.G. Janssen, P.J.M. van Bentum, K.A.M. Ampt, F.P.J.T. Rutjes, S.S. Wijmenga, J.G.E. Gardeniers, A.P.M. Kentgens, 'A Microfluidic high-resolution NMR flow probe' *J. Am. Chem. Soc.* 131, 5014 (2009).

J. Bart, J.W.G. Janssen, P.J.M. van Bentum, A.P.M. Kentgens, J.G.E. Gardeniers, 'Optimization of stripline-based microfluidic chips for high-resolution NMR' *J. Magn. Reson.* accepted (2009).

J. Bart, R.M. Tiggelaar, M. Yang, S. Schlautmann, H. Zuilhof, J.G.E. Gardeniers, 'Room-temperature intermediate layer bonding for microfluidic devices' *Lab Chip*, accepted (2009).

Oral presentations

J. Bart, P.J.M. van Bentum, J.W.G. Janssen, J.G.E. Gardeniers, A.P.M. Kentgens, 'NMR on a chip' *IMM Colloqium*, Radboud University, Nijmegen, The Netherlands, 1 May 2006.

J. Bart, P.J.M. van Bentum, J.W.G. Janssen, A.P.M. Kentgens, J.G.E. Gardeniers, 'A μ-Fluidic NMR Chip' *Dutch NMR-Discussion Group*, Nijmegen, The Netherlands, 12 October 2007.

J. Bart, A.J. Oosthoek - de Vries, J.W.G. Janssen, P.J.M. van Bentum, A.P.M Kentgens, J.G.E. Gardeniers, 'In-flow NMR spectroscopy on sub-µL samples in a microfluidic Chip' *9th Netherlands' Catalysis and Chemistry Conference (NCCC)*, Noordwijkerhout, The Netherlands, 4 March 2008.

J. Bart, A.J. Oosthoek - de Vries, P. Nieuwland, J.W.G. Janssen, P.J.M. van Bentum, A.P.M Kentgens, J.G.E. Gardeniers, 'In-flow reaction monitoring by NMR on nanoliter samples in a microfluidic Chip' *International Microreaction Engineering Technology Conference (IMRET)*, New Orleans, USA, 6-10 April 2008.

J. Bart A.J. Oosthoek - de Vries, P. Nieuwland, K. Koch, J.W.G. Janssen, P.J.M. van Bentum, A.P.M Kentgens, J.G.E. Gardeniers, 'Stripline-based NMR flow probes' *Process Analytical Technology (PAT) Lecture*, Schering Plough, Oss, The Netherlands, 19 March 2009.

Poster presentations

J. Bart, J.W.G. Janssen, P.J.M. van Bentum, E.R.H. van Eck, J.G.E. Gardeniers, A.P.M. Kentgens, 'Magnetic resonance micro spectroscopy' *FOM-decemberdagen*, Veldhoven, The Netherlands, 13 December 2005.

J. Bart, J.W.G. Janssen, P.J.M. van Bentum, J.G.E. Gardeniers, A.P.M. Kentgens, 'Stripline NMR' *Euromar Conference*, York, United Kingdom, 16-21 July 2006.

J. Bart, J.W.G. Janssen, P.J.M. van Bentum, J.G.E. Gardeniers, A.P.M. Kentgens, 'Stripline NMR' *Dutch NMR-Discussion Group*, Oss, The Netherlands, 13 October 2006.

J. Bart, J.W.G. Janssen, P.J.M. van Bentum, A.P.M Kentgens, J.G.E. Gardeniers, 'A stripline-based microfluidic probe for NMR spectroscopy' *Conference on Micro Total Analysis Systems (µTAS)*, Paris, France, 6-10 October 2007.

J. Bart, A.J. Oosthoek - de Vries, J.W.G. Janssen, P.J.M. van Bentum, J.G.E. Gardeniers, A.P.M. Kentgens, 'NMR on nanoliter samples in a microfluidic chip' *Euromar Conference*, St. Petersburg, Russia, 6-11 July 2008.

J. Bart, A.J. Oosthoek - de Vries, J.W.G. Janssen, P.J.M. van Bentum, J.G.E. Gardeniers, A.P.M. Kentgens, 'NMR on nanoliter samples in a microfluidic chip' *Dutch NMR-Discussion Group*, Eindhoven, The Netherlands, 10 October 2008.

Dankwoord

In dit dankwoord wil ik iedereen bedanken die bijgedragen heeft aan de totstandkoming van dit proefschrift.

Om te beginnen mijn beide promotoren, professor Han Gardeniers en professor Arno Kentgens, voor het in mij gestelde vertrouwen en de kansen die ze me geboden hebben.

Beste Han, het heeft me altijd verbaasd hoe jij in staat was de vele en zeer diverse onderzoeken die binnen je groep liepen tot in detail bij te houden. Tot het einde van mijn promotieonderzoek hebben we intensief samengewerkt en heb je me voorzien van grondige en kritische input. Daarnaast heb ik de vrijheid die er was om zijwegen te bewandelen (zoals beschreven in hoofdstuk 7 en 8) bijzonder gewaardeerd. Het is me een groot genoegen geweest met je samen te werken.

Beste Arno, de samenwerking met jou was nét zo intensief, omdat mijn onderzoek zich duidelijk in twee vakgroepen afspeelde. Een element in jouw persoon dat me altijd erg aanstond was je liefde om iemand iets te leren. Met je enthousiasme en gedrevenheid voor wetenschappelijk onderzoek was je een goede begeleider bij wie ik altijd kon binnenlopen. Je consciëntieuze commentaren op onze artikelen hebben me diverse slapeloze nachten bezorgd (achter je computer slaap je niet zo makkelijk) maar de journal-editors zijn er waarschijnlijk blij mee geweest.

En dan mijn co-promotor, Jan van Bentum. Ik denk dat ik nooit eerder zo'n veelzijdige fysicus als jij ontmoet heb. Zeker in het begin van het onderzoek raakte ik af en toe wat licht in m'n hoofd als ik nietsvermoedend voor een paar vraagjes je kamer binnenstapte en er vervolgens een enorme dosis informatie over me heen gestort werd. Later leerde ik daar beter mee om te gaan, door vooraf bij mezelf vast te stellen wat ik écht wilde weten voor ik je kamer zou verlaten. Ik kijk met plezier terug op onze vrolijke meetings, en zie met spanning uit naar onze toekomstige samenwerking.

Mijn eerste NMR ervaringen heb ik opgedaan als student in de vakgroep Biosensoren (BIOS) bij Henk Wensink. Henk wist me in korte tijd de geheimen van deze techniek bij te brengen. De metingen werden verricht op een permanente magneet die zo temperatuurgevoelig was dat het veld versteld kon worden met de luxaflex. Henk, bedankt voor de leuke tijd en je enthousiastmakende begeleiding.

De meer doorwrochte kennismaking met magnetische resonantie onderging ik toen ik in de leer ging bij Ernst van Eck. Maar het bleef niet bij de leer: van jou heb ik echt leren NMR-en. Ook later kon ik telkens bij je langs komen als er wat databehandeling moest gebeuren. Bedankt!

Dit proefschrift was waarschijnlijk bij hoofdstuk 1 blijven steken als Hans Janssen er niet was geweest. Beste Hans, hartelijk bedankt voor de diverse glanzende probes die je vernuftig in elkaar sleutelde. Je was altijd heel vindingrijk, maar vooral ook secuur, een eigenschap die belangrijk bleek voor het behalen van hoge resolutie resultaten. Hartelijk bedankt voor onze fijne samenwerking!

In hetzelfde kamertje van Hans huisde ook Jan van Os, de rf-goeroe. Beste Jan, met jou er bij was het altijd een gezellige boel in het rf-lab, niet in het minst door je plastische taalgebruik als je iets ging uitleggen. Ik werd altijd getroost door je bemoedigende woorden dat je 'er op de brommer naar huis nog wel eens over na zou denken'.

Zodra er chips klaargestoomd waren in de Twentse cleanroom stond Anna Jo gereed om ze te gaan gebruiken. Beste Anna Jo, we hebben misschien niet zoveel samengewerkt als we oorspronkelijk voor ogen hadden. Toch hebben we leuke experimenten gedaan, en veel praktische ervaring opgedaan die je in de komende onderzoeksjaren kunt gebruiken. Veel succes met je promotie!

Dear Jorge, our stay in St. Petersburg was a nice experience for me. Our conversations about the more weighty things in life were serious and sometimes quite fierce, but friendly. Thanks! Ook de andere collega's in Nijmegen kunnen niet onbenoemd blijven: Marian, Paul, Margriet, Eugenio, Suresh, Chandrakala, Andreas, Adri, Sjaak, Gerrit, Jos, Sybren, Kirsten, Ramon, Frank, Hans Heus, Marko, Marc, Otmar, Agnieszka en Aafke. Allemaal bedankt voor de goede tijd.

Toen onze chip eenmaal begon te werken moesten er natuurlijk relevante vloeistoffen worden gemeten, dus eerst maar eens een slokje hersenvocht erin. Voor deze experimenten werkte ik samen met Ard Kolkman. Ard, onze samenwerking was kort maar hevig. Ik herinner me nog als de dag van gisteren dat we dachten onze eerste succesvolle meting te hebben verricht. 's Avonds liep ik in een overwinningsroes door het lab om maar gelijk een tweede meting in te zetten toen jij binnenkwam om met een grafstem te melden dat de door ons gesignaleerde piekjes helaas van glycerol bleken te zijn. Gelukkig is het allemaal toch goed gekomen.

Een andere relevante applicatie was het meten van reactiekinetiek waarvoor de mannen van Future Chemistry werden geraadpleegd. Beste Pieter en Kaspar, aan onze samenwerking heb ik zeer veel vreugde beleefd, mede door jullie enthousiaste reacties en ideeën. Het feit dat onze gloednieuwe NMR-detector openbaarde dat een supersimpele reactie ("deze reactie gaat gewoon batsh en klaar is kees") heel wat ingewikkelder bleek te verlopen dan we verwacht hadden mocht de pret niet drukken. En toen natuurlijk de boel publiceren. Wat een toestand! De feestelijke

toast die we hebben uitgebracht op onze langverwachte *JACS* publicatie zal ik niet gauw vergeten.

Mijn kamergenoten van 146 bedank ik voor het feit dat ze mijn aanwezigheid zo lang geduld hebben. Ik vond het plezierig met jullie op een kamer te zitten. Vincent, zoals je ziet, een proefschrift schrijven lukt ook op een Windows machine, dus je hebt me nóg niet om voor een Apple. Wojtek, you're nice and very modest guy, I appreciated your presence in our room. Thanks for the interesting discussions we had about politics, Poland and publications (of other people). En tenslotte Roald: Wat hebben we samen veel plezier gehad tijdens onze geurige waferbonding experimenten. Als wij de cleanroom binnenkwamen, maakten anderen dat ze wegkwamen en wij hadden het rijk alleen. En toen de chip eenmaal werkte was je niet meer te temmen: alle vloeistoffen in het lab moesten er doorheen geflusht worden, liefst onder zo hoog mogelijke druk. Ik heb je zeer gewaardeerd als vriendelijke collega, zeker ook vanwege je behulpzaamheid die op de UT legendarisch is.

Beste Stefan, hartelijk bedankt voor de chips die je voor me gefabriceerd hebt. Op het moment dat we superdunne wafers gingen gebruiken, wist ik Han om te praten om ze door jou te laten maken en het is nog gelukt ook. Trouw kwam je me elke dag melden wat de 'breakage score' was. Verder was je altijd ter plaatse als er problemen van grafische aard waren. Dat kwam me voornamelijk tijdens het schrijven bijzonder van pas. En niet te vergeten: met een 'punktlichkeit' die we van een Duitser kunnen verwachten stond je om 12.00 uur op ons raam te bonken om ons te herinneren aan de lunch.

The other MCS-members are acknowledged for creating the comfortable and cosy atmosphere which made working pleasant: Jacqueline, Piotr, Quentin, Anil, Dawid, David, Bilge, Wim, Selm, Elizaveta, Nikolay, Maciej, Regina, Sertan and Kevin. Many thanks for the great time I had with you.

Toen ik Rob Lammertink van de Membrane Technology Group vroeg of hij iemand wist waarmee ik zou kunnen samenwerken op het gebied van het concentreren van hele kleine sample volumes deed hij me wel een heel goede tip aan de hand: Ramon Groote. Beste Ramon, bedankt voor de korte maar uiterst productieve samenwerking. Er is een heus hoofdstuk 7 uit ons werk voortgevloeid, en dat in een tijdsbestek van minder dan drie maanden. Dat ze het bij de MT groep jammer vonden dat je weg ging is geen wonder. Veel succes met je verdere onderzoek.

For the wafer bonding chemistry (chapter 8) we collaborated with professor Han Zuilhof and Menglong Yang. I want to kindly acknowledge you both for the fruitful discussions which have led to beautiful results.

De eerste anderhalf jaar van mijn onderzoek (voordat MCS opgericht werd) zat ik in de vakgroep BIOS die aangevoerd werd door Professor Albert van den Berg. Beste Albert, bedankt voor de tijd die ik in je uiterst gezellige groep heb mogen doorbrengen. De eerlijkheid gebiedt me te zeggen dat Han's mededeling dat ik met hem meeging naar MCS me eerst lichtelijk ontstemde: ik had het prima naar m'n zin bij BIOS. Gelukkig is deze ontstemming van korte aard gebleken. Ik heb de gastvrijheid die na ons vertrek nog steeds in de koffiehoek geboden werd gewaardeerd. Enkele BIOS-namen mogen hier overigens zeker niet ontbreken: allereerst Johan Bomer, die me de cleanroom beginselen heeft bijgebracht. Verder denk ik aan de oud-kamergenoten Wouter Sparreboom en Paul ter Braak. Wouter, jij bent een plezierige collega met wie altijd iets zinnigs te bespreken was. Toen we allebei kindertjes kregen, hebben onze gesprekken vast wel eens tot opgetrokken wenkbrauwen van de andere aanwezigen geleid. Ik wens je met je gezin het beste toe. Paul, met je onafscheidelijke big-smile was je altijd het zonnetje in onze kamer. Helaas zijn je heroïsche pogingen me enthousiast te maken voor moderne muziek op niets uitgelopen, ik kan de smaak er niet van te pakken krijgen. Verder bedank ik ook andere (oud-) BIOS mensen: Hermine, Matthieu, Jan van Nieuwkasteele, Ana, Steven, Arjan, Egbert, Jan Eijkel, Daniël, Wouter Olthuis, Ad, Sebastiaan, Jurjen, Erik Krommenhoek, Erik Faber, Loes, Floor, Eddy, Edwin, Georgette, Severine en Iris. Het was een mooie tijd.

In dit dankwoord kan ik eindelijk mijn belofte aan Peter Linders inlossen. Beste Peter, bedankt voor het feit dat je altijd voor ons klaar stond als er iets aparts moest gebeuren in de cleanroom, maar vooral voor het herhaaldelijk beschikbaar stellen van je wetbench om onze voornoemde geurige experimenten in uit te voeren. Ik weet nog goed hoe Roald en ik voor de eerste keer gingen proberen zuurstofvrij Sodiumnaphthalene te schenken. Je bench onderging een complete metamorfose, en ik kon je alleen maar geruststellen met de melding dat je genoemd zou worden in de acknowledgements. Bij dezen.

Mijn ouders verdienen een belangrijke plaats. Papa en mama, ik wil jullie heel hartelijk bedanken voor de voortdurende stimulans gedurende mijn studie en de interesse in de vorderingen van het onderzoek. Zoals jullie weten waardeer ik de belangstelling bijzonder. Dat geldt overigens in gelijke mate voor mijn broers en zussen die, ofschoon werkzaam in totaal andere vakgebieden zich toch graag lieten

bijpraten over de nieuwtjes van het NMR-front. Ook mijn schoonmoeder, zwagers en schoonzussen wil ik bedanken voor hun betrokkenheid.

En dan: Gerdien! Dank voor je ondersteuning en je geduldig oor voor mijn vaak veel te technische verhalen. Hoezeer ik jou waardeer zal ik hier niet proberen te formuleren, je weet het. Het is heerlijk met jou getrouwd te zijn, en te genieten van onze Ruth en Jesse. Ruth en Jesse, als jullie iets groter zijn zal papa eens voorlezen uit dit boekje.

Ik wil niet besluiten met een dankwoord aan mensen. Dit proefschrift is geschreven in de overtuiging dat wij op elk ogenblik van God het leven, het verstand en de kracht nodig hebben om ons werk te kunnen verrichten. Daarom: die roemt, roeme in de Heere.

Jacob